feStructural Stability and Radiation Tolerance of Nanocrystalline Cu-Ta for Extreme Applications

by

Soundarya Srinivasan

A Dissertation Presented in Partial Fulfillment
of the Requirements for the Degree
Doctor of Philosophy

Approved June 2021 by the
Graduate Supervisory Committee:

Kiran N. Solanki, Chair
Pedro Peralta
Terry Alford
Kris A. Darling

ARIZONA STATE UNIVERSITY

August 2021

ABSTRACT

Nanocrystalline (NC) materials are of great interest to researchers due to their multitude of properties such as exceptional strength and radiation resistance owing to their high fraction of grain boundaries that act as defect sinks for radiation-induced defects, provided they are microstructurally stable. In this dissertation, radiation effects in microstructurally stable bulk NC copper (Cu)- tantalum (Ta) alloys engineered with uniformly dispersed Ta nano-precipitates are systematically probed. Towards this, both ex-situ and in-situ irradiations using heavy (self) ion, helium ion, and concurrent dual ion beams (He+Au) followed by isochronal annealing inside TEM were utilized to understand radiation tolerance and underlying mechanisms of microstructure evolution in stable NC alloys. With systematic self-ion irradiation, the high density of tantalum nanoclusters in Cu-10at.%Ta were observed to act as stable sinks in suppressing radiation hardening, in addition to stabilizing the grain boundaries; while the large incoherent precipitates experienced ballistic mixing and dissolution at high doses. Interestingly, the alloy exhibited a microstructure self-healing mechanism, where with a moderate thermal input, this dissolved tantalum eventually re-precipitated, thus replenishing the sink density. The high stability of these tantalum nanoclusters is attributed to the high positive enthalpy of mixing of tantalum in copper which also acted as a critical driving force against atomic mixing to facilitate re-precipitation of tantalum nanoclusters. Furthermore, these nanoclusters proved to be effective trapping sites for helium, thus sequestering helium into isolated small bubbles and aid in increasing the overall swelling threshold of the alloy. The alloy was then compositionally optimized to reduce the density of large incoherent precipitates without

compromising on the grain size and nanocluster density (Cu-3at.%Ta) which resulted in a consistent and more promising response to high dose self-ion irradiation. In-situ helium and dual beam irradiation coupled with isochronal annealing till 723 K, also revealed a comparable microstructural stability and enhanced ability of Cu-3Ta in controlling bubble growth and suppressing swelling compared to Cu-10Ta indicating a promising improvement in radiation tolerance in the optimized composition. Overall, this work helps advancing the current understanding of radiation tolerance in stable nanocrystalline alloys and aid developing design strategies for engineering radiation tolerant materials with stable interfaces.

DEDICATION

I dedicate this dissertation to my family – parents Hemalatha and Srinivasan, my sister Iswarya who have been a constant source of encouragement and have always been there for me, and my nephew Shrihari who shows great enthusiasm to understand what I do. Last but not least, to my fiancé, Arun who pushes me to be a better person and for his unwavering support.

ACKNOWLEDGEMENTS

This dissertation would have not been possible without the support of many people. First and foremost, I would like to express my gratitude to my Ph.D. supervisor, Dr. Kiran Solanki for providing me with immense opportunities and motivation to push my limits throughout my Ph.D. I am profoundly grateful to my committee members, Dr. Kris Darling, Dr. Pedro Peralta, and Dr. Terry Alford for their valuable inputs and discussions.

My sincere thanks to my labmates and members of the Multiphysics Lab - Prof. Mehul Bhatia, Prof. Ilaksh Adlakha, Dr. Mansa Rajagopalan, Dr. Scott Turnage, Dr. Benyamin Gholami, Dr. Pulkit Garg, Dr. Chaitanya Kale, Vikrant Beura, Saurabh Sharma, Sainyam Nagar, and Yashaswini Karanth for numerous valuable discussions throughout my research. I am grateful to Dr. Billy Hornbuckle at Army Research Laboratory (ARL) for Atom Probe (APT) characterization and for providing useful tips whenever needed.

Additionally, I extend my gratitude to Dr. Yongqiang Wang, Matthew Ryan Chancey, Dr. Khalid Hattar, and Dr. Eric Lang Joseph for the constructive inputs and help with ion irradiation and in-situ irradiation experiments carried out at the Center for Integrated Nanotechnologies (CINT), an Office of Science User Facility jointly operated by Los Alamos and Sandia National Laboratories. Finally, last but not the least, I acknowledge the use of facilities within the LeRoy Eyring Center for Solid State Science at Arizona State University and CAMECA instruments for APT experiments.

I am appreciative of the financial support provided by ARL and National Science Foundation (NSF) under contract no W911NF-15-2-0038 and 1663287, respectively.

TABLE OF CONTENTS

Page

LIST OF TABLES

Table Page

LIST OF FIGURES

Figure Page

Figure Page

Figure Page

Figure Page

Figure Page

Figure Page

CHAPTER 1

1 MOTIVATION

Increasing concerns about global warming and CO_2 emissions have raised the demand for renewable and sustainable energy sources. Nuclear power has the major renewable energy contribution worldwide. Continuously increasing number of reactors every year demands advanced materials with high strength and radiation tolerance. However, the development of cutting edge structural materials for next-generation reactors is considerably challenging due to the harsh reactor environment viz. high energy neutron exposure (displacement damage), temperature and corrosion environment which results in degradation of structural materials affecting the safety and lifetime of the reactors (Murty and Charit 2008; S.J. Zinkle and Was 2013). In addition to the radiation induced displacement cascades and point defects, helium produced by transmutation reactions is more detrimental causing volumetric swelling and high temperature helium embrittlement. Mitigating harmful radiation effects is not only of importance to the nuclear industry but also to microelectronic devices/detectors in space applications (Fleetwood, Winokur, and Dodd 2000; Stassinopoulos and Raymond 1988; Srour and McGarrity 1988), solid state electronic device modification using ion beams (Clark et al. 1987) and surface modification for wear and corrosion resistance using ion implantation.

Interfaces like grain boundaries and phase boundaries act as efficient sinks to annihilate radiation induced defects. Designing materials with a large fraction of natural defect sinks is the key to alleviate radiation effects. Nanocrystalline (NC) materials are one of the promising candidates due to their high volume fraction of grain boundaries which act as

unbiased sinks for radiation defects(Cheng et al. 2016). However, microstructural instabilities (e.g., grain growth) observed during high energy neutron radiation complicate the interpretation of grain size effects; hence, a mechanistic based understanding of radiation tolerance behavior in NC alloys is convoluted (Wurster and Pippan 2009). Also, temperature and radiation-induced grain growth degrade their efficiency as defects sink giving poor radiation damage resistance. This calls for materials that are not only immune to radiation induced degradation but also maintain/enhance their mechanical properties and microstructural stability during sustained radiation exposure.

With various computational and experimental efforts, grain boundary stabilization has been achieved through solute additions (C. C. Koch et al. 2008). Understanding the radiation response of such stabilized system is of utmost importance to aid better design strategies for developing radiation tolerant materials. Thus, this dissertation aims to systematically study the radiation response of a microstructurally stable bulk NC copper (Cu)- tantalum (Ta) alloy system where Ta atomic clusters or nanometer sized precipitates are strategically engineered in the alloys' microstructure that facilitates kinetic stability and superior mechanical properties (Frolov et al. 2012; Darling et al. 2016).

CHAPTER 2

2 BACKGROUND AND RESEARCH OBJECTIVES

2.1 Background

Materials when exposed to intense radiation such as in nuclear reactors are subjected to displacement damage as the high energy radiation knocks off an atom from its lattice site called a primary knock-on atom (PKA). This PKA further continues the displacement cascade until the energy of the displacing atom is less than the threshold displacement energy of the material at which point the atom settles at the interstitial position. Several theories have been proposed on the understanding of radiation damage cascades (), the impact produced by it, and ways of measuring the damage (Stiegler and Mansur 1979; Stoller 2012). Radiation induced displacement cascade generates a high density of vacancies and interstitials (Frenkel pairs) which eventually coalesce to form defect clusters like interstitial dislocation loops, voids, and stacking fault tetrahedra (SFT). As the concentration of these extended defects increases combined with helium generated as a result of transmutation reaction, radiation poses five major threats which can be summarized as hardening and embrittlement, phase instabilities from radiation induced precipitates, irradiation creep, volumetric swelling from void formation, and high temperature helium embrittlement (Steven J. Zinkle and Busby 2009), thus leading to a reduction in performance and lifetime (Gary S. Was 2017).

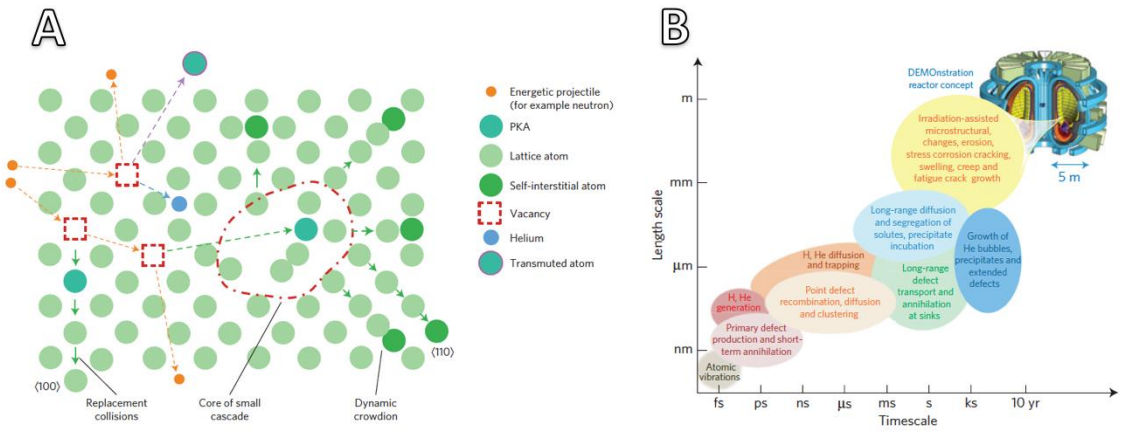

Figure 1: Schematic illustration of (A) Irradiation damage evolution at lattice scale (B) Time and length scales of multiscale damage processes responsible for microstructural changes and resulting property degradation during high-energy neutron irradiation of plasma-near in-vessel materials. The evolving microstructural changes (yellow and blue ellipses) substantially affect, in turn, defect nucleation and growth at the nanoscale. (From (Knaster, Moeslang, and Muroga 2016))

As mentioned earlier, interfaces like grain boundaries and phase boundaries act as efficient sinks to annihilate radiation induced defects. Thus, in order to mitigate radiation damage, various research efforts focus on designing and processing materials with large sink concentrations (see **Figure**). The current state of the art materials for reactor applications are reduced activation ferritic-martensitic (RAFM) and oxide dispersion strengthened (ODS) steels. ODS steels are of great interest due to their superiority in defect sink efficiency and high temperature properties attributed to the fine oxide dispersions (Sagaradze et al. 2001). However, they are still not completely immune to radiation hardening at considerably high doses (Alamo et al. 2007; 2000) and the stability of oxide phases (dissolution, growth and amorphization) are not well understood due to inconsistency with results observed in the literature (Wharry, Swenson, and Yano 2017). Various research on other advanced materials such as nano layered composites has shown that improving interface concentration (i.e. reducing the spacing of nano layers) creates

overlapping void denuded zones which is the key aspect in achieving void free structure (W. Han et al. 2013; Demkowicz, Hoagland, and Hirth 2008; Misra et al. 2007).

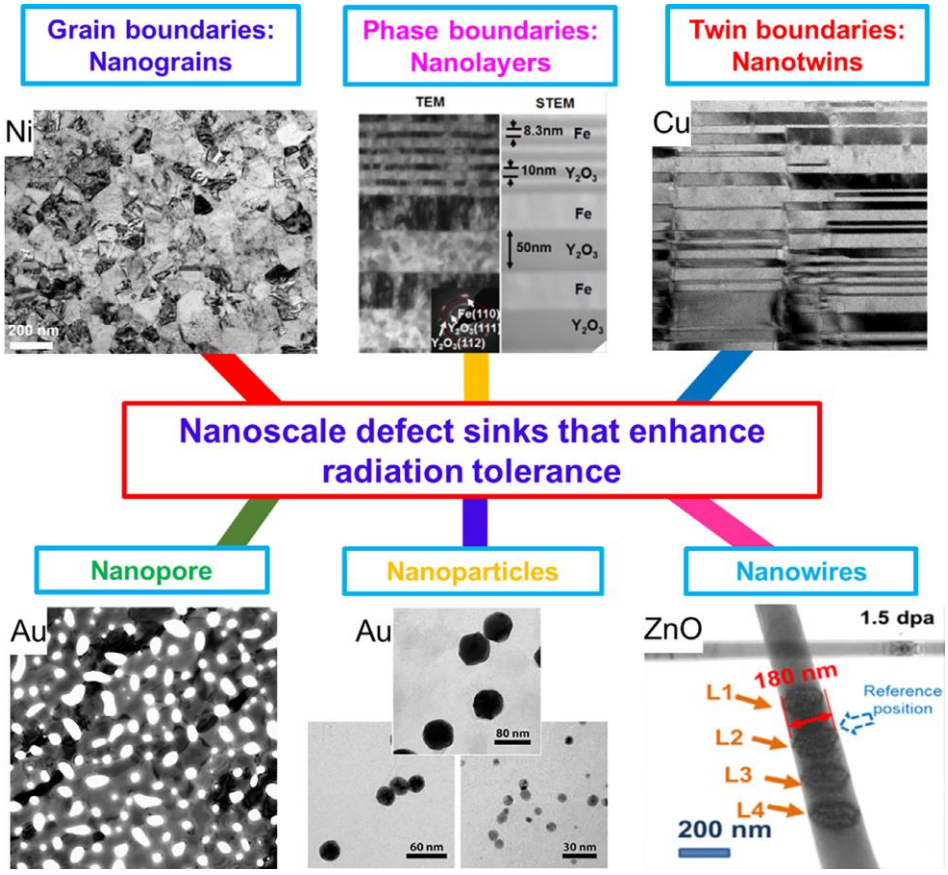

Figure 2: Key engineering strategies to alleviate radiation damage (From (Xinghang Zhang et al. 2018))

Likewise, nanocrystalline (NC) materials are one of the promising candidates due to the high volume fraction of grain boundaries which act as unbiased sinks for radiation defects (Cheng et al. 2016; Beyerlein et al. 2013). However, the inherent issue with microstructural instabilities (e.g., grain growth; see **Figure 3**) in intense radiation environment complicates the interpretation of grain size effects (Wurster and Pippan 2009; J. C. Liu, Li, and Mayer 1990; Atwater, Thompson, and Smith 1988); reduces the sink

concentration and efficiency, and degrades their potential. For instance, Mohamed et al., observed immense softening in nanocrystalline copper due to radiation induced grain growth, followed by radiation induced hardening (Mohamed et al. 2016).

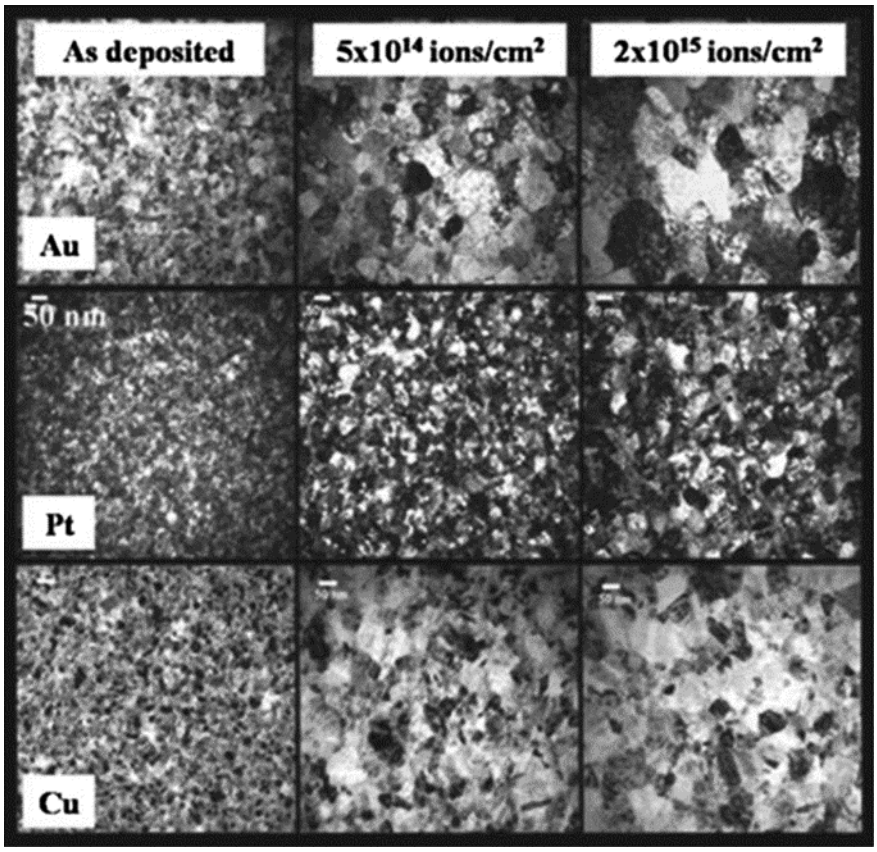

Figure 3: Microstructural instability in nanocrystalline materials with irradiation observed in the literature (from (Xinghang Zhang et al. 2018))

Stabilizing grains in nanostructured materials can provide stable sinks to achieve structures immune to radiation damage. Through years of research efforts in the solute selection and technological advances in material processing techniques, such stabilization can be achieved through appropriate solute additions which either segregate to grain boundaries (thermodynamic approach) or form nanoprecipitates pinning the grain boundaries (kinetic approach) (Carl C. Koch et al. 2013; C. C. Koch et al. 2008). Moreover,

appropriate solute addition to pure metals, irrespective of grain sizes can provide significant improvement to several engineering properties such as corrosion and wear resistance, mechanical strength, ductility, electrical and thermal properties, etc.

This work utilized non-equilibrium processing of pure metals with appropriate immiscible solute additions leading to kinetic pinning by second phase particles (Arshad et al. 2013; M. Wang et al. 2014). For instance, Darling et al. have observed extraordinary strength, stability and superior high temperature properties (Darling et al. 2016; Turnage et al. 2018) in NC alloy of immiscible copper tantalum system (Cu-Ta) produced by high energy ball milling followed by equal channel angular extrusion which is attributed to a high density of Ta rich nanoclusters. In addition to providing kinetic and thermodynamic stability resulting in a high fraction of stable grain boundaries (Darling et al. 2013; Frolov et al. 2012), high density of coherent/semi-coherent dispersoids in these immiscible systems can act as effective sinks for radiation induced defects. Thus, maintaining a specific length scale with these nanoclusters and addressing the grain instability can provide numerous stable sites for radiation defect neutralization which is the core hypothesis of this dissertation. To validate this and to uncover the radiation damage mechanisms involved in a stable nanocrystalline material, we use the NC Cu-Ta system as a model material and perform various types of ion irradiations (heavy ion, helium ion, dual beam) both ex-situ and in-situ at several conditions to emulate the reactor radiation environment and systematically evaluate the response.

2.2 Research Objectives

Understanding how a stable nanocrystalline microstructure responds to various aspects in the radiation environment is still in nascent stages and is critical to improving existing design strategies for developing radiation tolerant materials with stable interfaces. Therefore, this dissertation aims to address the critical need of systematically understanding the radiation tolerance from various avenues of a full dense powder processed nanocrystalline Cu-Ta alloy (that has been shown to exhibit high thermomechanical stability as well as exceptional high temperature performance) and aid compositional and design optimization for developing radiation tolerant materials. The objectives are

i. Evaluating radiation tolerance of nanocrystalline Cu-10Ta to high dose self-ion irradiation

NC Cu-10at.%Ta has been previously shown to have excellent thermomechanical stability (eg., creep, high strain rate loading, fatigue, etc.,) and high temperature properties [(Darling et al. 2016), (Turnage et al. 2018)]. In this chapter (Chapter 3), radiation hardening, lattice stability and microstructural (grain and phase) stability under systematic self-ion irradiation (to emulate displacement damage) are evaluated for NC Cu-10at.%Ta. Experiments including nanoindentation, grazing incidence X-ray diffraction, Transmission electron microscopy, Spectroscopy (EDS, EELS) and Atom Probe tomography were performed to understand the radiation tolerance of the NC Cu-Ta alloy and draw comparison with candidate materials from literature. In this section, two important conclusions were made: 1) NC Cu-10Ta shows exceptional microstructural stability and

resistance to radiation hardening compared to various candidate materials under similar conditions; 2) The tantalum nanoclusters and large sacrificial precipitates which are dissolved at high dose levels are reprecipitated with thermal input thus replenishing the sink density and self-healing the microstructure. This is attributed to the high positive enthalpy of mixing of Ta in Cu which forms the basis of a good design strategy.

ii. Understanding the role of Ta nanoclusters in neutralizing helium bubble damage in nanocrystalline Cu-10Ta

Besides displacement damage, neutron radiation introduces helium through transmutation reaction. Helium has more deleterious effects in the metals as they are nearly insoluble and stabilize the voids with pressurized bubble formation, thereby accelerating swelling and blistering [(Trinkaus and Singh 2003; Lucas 1984)]. In this chapter (Chapter 4), the microstructural response of NC Cu-10Ta to helium irradiation at room temperature and 450 C is analyzed using Transmission electron microscopy and atom probe tomography to understand the sink efficiency of the interfaces. The major conclusion made in this chapter is that the Ta nanoclusters act as preferential sites for helium segregation and bubble nucleation thus sequestering the helium bubbles resulting in reducing swelling.

iii. Analyzing the response and stability of different Ta precipitates to high dose self-ion irradiation and aid compositional optimization for better radiation tolerance

NC Cu-10at.%Ta alloy examined in (i) showed a significant radiation tolerance with enhanced immunity due to stable length scales or microstructural unit along with the presence of a sacrificial phase. Therefore, to address the role of sacrificial phases, in this

chapter (Chapter 5), the study is extended on compositionally optimized NC Cu-3 at.% Ta alloy, which has similar size and density of nanoclusters as NC Cu-10at.%Ta alloy but fewer incoherent large Ta particles. Recent work on NC Cu-3at. %Ta had shown similar mechanical performance and better long-term thermal stability as NC Cu-10at.%Ta alloy. Thus, microstructural and phase stability in nanocrystalline Cu-3at.%Ta alloy to high dose self-ion irradiation at room temperature and 300 C was analyzed to draw a comparison with Cu-10at.%Ta which showed promising enhancement

iv. In-situ irradiation and annealing response comparison in Cu-10Ta and Cu-3Ta to helium and dual ion irradiation (heavy ion + helium ion)

To further extend the comparison made in the previous chapter, this section (Chapter 6) focused on in-situ irradiation and subsequent isochronal annealing of Cu-10Ta and Cu-3Ta to get more insights on damage accumulation, defect and precipitate evolution and finally, reveal hitherto unexplored nano-scale irradiation tolerance mechanisms in the alloy through real-time observations. Dominant bubble coarsening mechanisms involved in these alloys at the given temperature range are discussed with insights from real-time bubble evolution during the annealing process. Comparison of bubble evolution between both the alloys revealed smaller bubbles size and density in Cu-3Ta indicating a better promise in the optimized composition.

In the end, a future research framework is presented in order to gain further understanding of the radiation response of stable NC alloys and the applicability of this design strategy to other candidate material systems. Thus, this dissertation systematically characterizes the radiation tolerance behavior in a stable NC alloy using NC Cu-10Ta as a model material system and eventually attempts to optimize the solute concentration to improve radiation response. The key takeaway from this study is that engineering immiscible systems (with high positive heat of mixing) in appropriate concentrations through mechanical alloying acts as an efficient design strategy in maintaining the microstructural length scale (stability) and in offering strong competition to the undesirable ballistic dissolution mechanism in irradiation often observed in many dispersion-strengthened (e.g., ODS) alloys.

CHAPTER 3

3 THEORY AND EXPERIMENTAL PROCEDURES

3.1 Material Processing

The nanocrystalline microstructure can be achieved through several processing techniques such as ion beam mixing, physical vapor deposition and ball milling. High energy mechanical alloying is a well-established and successful technique for processing nanocrystalline and non-equilibrium solid solutions with positive enthalpy of mixing (C.C. Koch 1997; Klassen, Herr, and Averback 1997; C.C. Koch 1993). Two different Cu-Ta alloys having different Ta concentrations, 3at. % Ta and 10at. % Ta, were synthesized using high-energy cryogenic mechanical alloying carried out in a SPEX 8000 M shaker mill. Hardened steel vial was loaded with appropriate amounts of Cu and Ta powders (~ 325 mesh and 99% purity) weighing 5g in total. 440C Stainless steel balls were utilized as the milling media with a ball to powder mass ratio of 10:1. The vials were sealed in an Ar atmosphere in a glove box (< 1 ppm oxygen and H_2O) and placed in a nylon sleeve modified for liquid N_2 inflow and outflow. The vial was equilibrated for 20 mins prior to milling to attain a temperature of -196 ºC. Cryogenic milling of Cu-Ta powders for 8h resulted in an un-agglomerated powder mass with a particulate size range of 20–100 μm. The process was repeated until enough powder was obtained for further processing.

3.2 Sample Preparation

3.2.1 Consolidation of Powder

Cu-Ta powders were consolidated using an equal channel angular extrusion (ECAE) process at 700 ºC. The as-milled powders were loaded into Ni cans and sealed in the glovebox. The Ni cans were heated to 700 ºC and equilibrated for 40 mins under Ar atmosphere. To minimize temperature losses, ECAE die assembly was preheated to 350 ºC before the Ni cans at 700 ºC were dropped into it. The Ni cans were then extruded following the route B_c (Segal 1995) at an extrusion rate of 25.5 mm s^{-1}. Four consecutive passes of extrusion at 90º were done to minimize texture effects. The extrusion resulted in a total strain of about ~ 450%. Electronic Discharge Machining (EDM) was used to cut samples from the extruded cans. All the powder processing was performed at Army Research Lab under the guidance of Dr. Kris Darling. The extruded samples of 3mm diameter were cut to ~1.5 mm height and mechanically polished to mirror finish on both the sides before irradiation experiments.

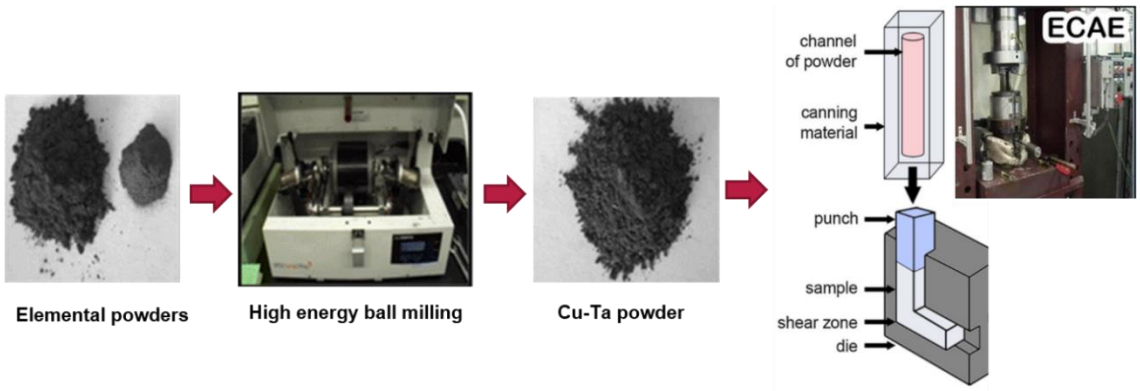

Figure 4: High energy ball mill and ECAE (Tschopp et al. 2014)

3.2.2 TEM sample preparation

Cross sectional samples for TEM experiments post ex-situ irradiation and for in-situ irradiation were carefully fabricated using FEI Nova 200 Dual beam FIB-SEM. A platinum protection layer was deposited on the surface before starting the sample fabrication. Lamella of dimensions ~ (15 x 4 x 1) μm^3 was lifted out and mounted on a molybdenum grid where it was eventually thinned to electron transparency using beam energies ranging from 30 kV, 1 nA to 5 kV, 20 pA. Final cleaning of the lamella was carried out at 2 keV for 1 minute on each side and plasma cleaned in Ar atmosphere for ~15-20 mins.

3.3 Experiment

3.3.1 Ion irradiation experiments

Neutron radiation damage can be emulated using charged particles such as electrons, protons and ions. Heavy ion is used as a surrogate to neutron radiation to achieve high damage levels [(Gary S. Was 2017)] and helium ion to emulate transmuted helium effects. For heavy ions, self-ion was utilized to avoid chemical interactions. Irradiations were performed on cylindrical specimens of Cu10at.%Ta (diameter 3 mm and length ~1.5 mm) in the Ion Beam Materials Laboratory (IBML) at Los Alamos National Laboratory. The current was monitored carefully throughout the irradiation and the average current was used to calculate the flux. The samples were mounted to the heating stage with silver paste for good thermal conduction and the stage temperature was monitored through a thermocouple attached to the stage to track any fluctuations. Additionally, helium and dual beam irradiations were carried out inside TEM for real-time observation of damage

evolution and synergistic effect of helium and displacement damage. The experiments were carried out in the In-situ Ion Irradiation TEM (I^3TEM) facility of Sandia National Laboratory that constitutes a Jeol 2100 TEM equipped with ion accelerators, laser heating and cooling and high temporal resolution imaging capabilities, enabling exploration of coupled extreme environments (Hattar, Bufford, and Buller 2014).

3.3.2 SRIM analysis

The energy of the primary knock-on atoms in high energy radiation is sufficiently high for the fission and fusion reactors to generate collision cascades. Various analytical models have been proposed to quantify the displacement cascade event of which Kinchin-Pease model gained wide popularity. Eventually, Norgett, Robinson and Torrens came up with a displacement model which is the current standard for nuclear industry (Nordlund et al. 2018). The Stopping and Range of Ions in Matter (SRIM) is a Monte Carlo simulation code widely used to compute ion deposition and damage profiles in materials exposed to energetic ions using binary collision approximation (Ziegler, Ziegler, and Biersack 2010; Ziegler and Biersack 1985). Damage profiles were calculated utilizing SRIM's quick Kinchin Pease model, which gives the best correlation with the internationally adopted NRT (Norgett, Robinson and Torrens) displacement model (Stoller et al. 2013). The simulations were performed with 99999 ions for all irradiations. Threshold displacement energies (E_d) for Cu and Ta were set to 30 eV and 90 eV respectively ("Standard Practice for Neutron Radiation Damage Simulation by Charged-Particle Irradiation" 96). Vacancy.txt and Range.txt files generated at the end of the simulation were utilized to calculate the dose/damage profile and profile of implanted ions respectively.

3.3.3 DPA and dose rate calculations

Since radiation damage from different sources (neutrons, protons, heavy and light ions) and energies are different in magnitude, it is incorrect to compare them using fluence. Hence, a common parameter of the damage is represented through the atomic displacements created due to the energetic recoils. Dose in dpa (Displacements per atom) was calculated according to the following equation:

$$dpa = \frac{Fluence * \#displacements * 10^8}{N} \quad (1)$$

where, fluence = ion fluence in #ions/cm^2

#displacements = sum of atomic and recoil displacements from vacancy.txt in #/ion. A˚

N = the atomic density of Cu in atoms/cc (8.57x10^{22} atoms/cc)

Dose accumulation and rate depend on the ion beam current. The dose rate is given by

$$\frac{dpa}{s} = \frac{Fluence * \#displacements * 10^8 * I}{Q * N} \quad (2)$$

where, Q = #ions x charge of the ion = Fluence x Area of exposure x charge, and I = Ion beam current in Ampere

3.4 Characterization

3.4.1 Hardness testing

Nanoindentation is a depth sensing indentation technique that analyses localized deformation in a flat specimen in contact with a rigid indenter, utilizing the theories of

Hertzian contact stresses to determine its elastic properties(Fischer-Cripps 2004). In this study, Nanoindentation experiments were carried out on TI980 Triboindenter equipped with diamond Berkovich indenter of radius 120 nm. The hertz equations (for spherical surfaces) are indirectly extended to sharp conical indenter geometry with a cone semi angle of α. Hardness, which is the saturated value of mean contact pressure with increasing load, is calculated as the ratio of indentation load to the contact area. The area of contact at full load is determined by the penetration depth and the known indenter geometry. The slope of the unloading curve provides the measure of modulus (Oliver and Pharr 1992). Hardness (H) calculated from nanoindentation corresponds linearly with the yield stress (Y) as

$$H = CY \qquad (3)$$

where C is the constraint factor which is predicted to be ~3 for metals with a large E/Y ratio.

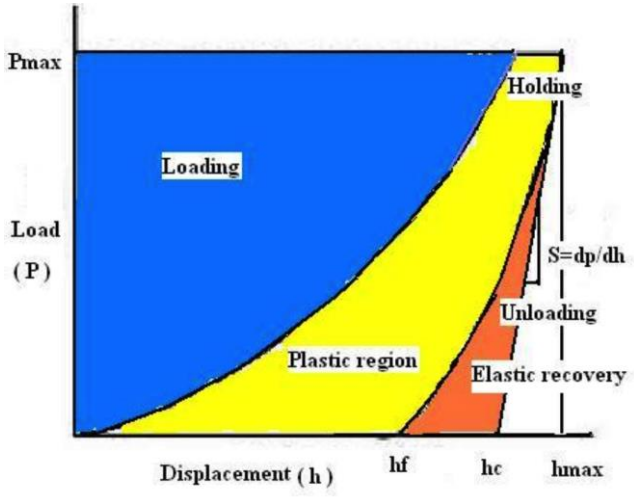

Figure 5: Typical load displacement curve illustrating different regimes of an indentation test *("Nano Indentation" n.d.)*

3.4.2 Grazing Incidence X-ray Diffraction experiments

PANalytical Xpert Pro with Cu kα radiation source (λ= 0.1542 nm) was utilized to get grazing incidence X-ray diffraction patterns. Mirrors and parallel plate collimators were utilized for incident beam and diffracted beam optics respectively. Peak shifts (2θ) were analyzed to detect any lattice contraction or expansion. Bragg's equation (Equation 4) was utilized to calculate lattice parameter (a) from the lattice spacing (d) obtained for prominent peaks (hkl planes) of Cu and Ta.

$$n\lambda = 2d \sin\theta\,, \ where\ d_{hkl} = \frac{a}{\sqrt{(h^2+k^2+l^2)}} \quad (4)$$

The incidence angle for the X-ray diffraction experiments to attain a penetration depth of <1 micron was determined from exponential X-ray attenuation characteristics (Equation 5). For an incident beam intensity of Io, penetrating through a material of density ρ, mass thickness x (x= ρt), thickness t, the final beam intensity is I based on the attenuation coefficient μ/ρ of the material. i.e., $I/Io = \exp[(-\mu/\rho)\,x]$ (5)

3.4.3 Microstructural characterization

Transmission electron microscopy (TEM) and scanning transmission electron microscopy (STEM) are widely used for microstructural characterization of nanostructured materials due to their greater resolution of nanostructured features. Imaging, diffraction patterns and elemental analysis were performed using aberration corrected electron microscopes (ACEM) namely Titan 8—300 (FEI) and ARM 200F (JEOL) at the LeRoy Eyring Center for Solid State Sciences. STEM images were acquired using an 8C probe

for high resolution with 8 cm camera length and a bright field aperture of 3mm. Multiple bright field (BF) and dark field images were captured in various magnifications to assess the microstructure and quantify statistics such as grain size, nanoclusters and cavities in the as-received and irradiated specimens. EELS and EDS were utilized to analyze any chemical changes in tantalum precipitates and radiation induced segregation at grain boundaries. EELS analysis was carried out in dual EELS mode with a dispersion of 1 eV/ channel and a 5 mm aperture. A step size of ~1 nm with a dwell time of 0.1 s was utilized for the scans. Selected area diffraction (SAD) patterns were utilized to investigate any amorphization of Ta particles.

Grain sizes were determined using BF and MAADF images which give the best contrast of grain boundaries. Grain size statistics were obtained from depth spanning ~100-600 nm from the irradiated to avoid the effects of peak damage region. More than 150 grains were sampled for each irradiation condition using ImageJ software to get the average grain size. Nanocluster size distribution was determined with the help of HAADF images at high magnification.

Voids and bubbles were identified using HAADF (High Annular Angular Dark Field) images which gave good contrast for the voids in the high Z matrix of Cu and Ta. Under and over focused TEM BF images were utilized to confirm small voids which were difficult to perceive. Swelling analysis was done by quantifying void/bubble size and density using Image J software and averaging over multiple regions for each condition. TEM lamella thickness was assumed to be ~60 nm. Swelling percentage for each condition was calculated based on the equation given below (Toloczko et al. 2014),

$$Swelling\ (\%) = 100\frac{Volume\ of\ voids}{Volume\ of\ lamella\ without\ voids} = 100\ \frac{\frac{\pi}{6}\sum_{i=1}^{N} {d_i}^3}{A.t-\frac{\pi}{6}\sum_{i=1}^{N} {d_i}^3} \quad (6)$$

where d is the void diameter, N is the total number of voids, A is the area of the lamella investigated and t is the thickness of the lamella.

Sink strengths of grain boundaries of grain size h and the nanoclusters of diameter d and number density N were calculated based on the equation given below,

$$S_b = \frac{15}{h^2} \quad (7)$$

$$\text{and} \quad S_{ppt} = 2\pi ND \quad (8)$$

3.4.4 Atom Probe Tomography

Atom probe tomography (APT) is an advanced material characterization technique that can generate 3D atom map data. This is achieved through field evaporation of ions from FIB fabricated sample (sharp tip) using high DC bias, whose position and mass are determined through the time-of-flight measurement and ion impact position in the detector respectively.

APT characterization was performed using a Cameca Local Electrode Atom Probe (LEAP) 5000 XS instrument. The specimens were lifted-out from the irradiated sample surface and welded to pre-fabricated silicon (Si) post using a Thermofisher Helios 660 dual-beam scanning electron microscope and focused ion beam (SEM/FIB) with a Ga source equipped with an Omniprobe micromanipulation system. Once welded to the Si post, specimens were sharpened to needle-shaped geometry of final tip diameter 100 nm

using annular ion beam milling with an acceleration voltage of 30kV and beam current of 0.18nA to 18pA. The last cleaning step was done with a 1kV ion beam to remove any damage introduced by using a higher energy ion beam. The field evaporation was performed at pulsed laser mode with a laser pulse energy of 50pj and a flexible laser repetition rate to maintain a minimum of 300 Da mass spectrum with a target evaporation rate of 0.5 %. The specimen was maintained at a base temperature of 30 K during the APT experiments. The APT datasets were reconstructed and evaluated using Cameca's Integrated Visualization and Analysis Software (IVAS) 3.6.12.

Composition of Ta nano-precipitates were determined using 1-D concentration profiles generated along various Ta 5 at. % interfaces by defining a cylindrical region of interest oriented along the analysis direction, perpendicular to the interface. Cluster identification for particles enriched with Ta was carried out using a maximum separation algorithm (Miller and Kenik 2004; Kolli and Seidman 2007). For further details of analysis techniques for Cu-Ta, please refer (Hornbuckle et al. 2015).

CHAPTER 4

4 RADIATION TOLERANCE AND MICROSTRUCTURAL CHANGES OF NANOCRYSTALLINE CU-10AT.%TA TO HIGH DOSE SELF-ION IRRADIATION

(The contents of this paper are published in (Srinivasan et al. 2020))

4.1 Introduction

Efficient operation and extended lifetime of future nuclear reactors depend on the performance of structural materials in an extreme radiation environment (S.J. Zinkle and Was 2013). High energy particle radiation causes displacement of atoms from their lattice sites leading to the formation of numerous point defects (vacancies and interstitials) whose subsequent diffusion and clustering to dislocation loops, voids and stacking fault tetrahedra (SFT) leads to volumetric swelling, hardening, phase segregation, disordering, etc., (Steven J. Zinkle and Busby 2009). Thus, the hunt continues for materials that are not only immune to radiation induced degradation but also maintain/enhance their mechanical properties during sustained radiation exposure.

Nanocrystalline and dispersion strengthened alloys are promising candidates due to high interface sink concentration (grain boundaries and phase boundaries) to alleviate radiation induced defects. However, microstructural and phase instability resulting from high energy displacement damage such as grain growth, ballistic mixing, Ostwald ripening, etc., affects the interface characteristics and density, limiting the potential of such materials (Wurster and Pippan 2009). Immiscible alloy systems have been observed to show great potential for developing thermally stable nanostructures through kinetic pinning

mechanisms (Koju et al. 2016). Furthermore, immiscible alloys driven far from equilibrium through mechanical alloying or irradiation, such as Cu-Ta, Cu-Nb, Cu-V, Cu-Mo, Ni-Ag, Ag-Fe, Ag-Cu etc., have been of great interest to researchers, since their response to severe plastic deformation/radiation is unique compared to their miscible counterparts (or those with low heat of mixing), due to the competition between ballistic mixing and thermodynamically driven kinetics such as decomposition and phase separation (Ma 2005; Wei and Averback 1997; Koju et al. 2018). Moreover, immiscible systems also result in numerous second phase particles/dispersoids which constitute a high density of interface sink in the material. Thus, the core strategy of this work is to maintain a stable length scale or microstructural unit along with the presence of a sacrificial phase in an immiscible alloy system for enhanced radiation tolerance.

Here, we use NC Cu-10 at. % Ta alloy (referred to herein as NC Cu-Ta alloy) with Ta nanoclusters of average diameter 3 nm and a spatial arrangement of proportional length scale, as a model material system. Recent works on this alloy have shown that introduction of stable nano dispersions led to extraordinary strength, thermomechanical stability and creep properties (Darling et al. 2016; Turnage et al. 2018), along with high thermal and electrical conductivity (Rajagopalan et al. 2019). Combining these unique mechanical, thermal and electrical properties with radiation tolerance will open avenues for applications such as high temperature heat exchangers and other reactor components. In this study, we primarily focused on investigating NC Cu-Ta alloy's self-ion irradiation response related to three of the most detrimental radiation effects, i.e., radiation induced hardening, void

swelling, and microstructural/phase instability to elucidate the radiation tolerance behavior of a stable nanocrystalline material.

4.2 Methodology

4.2.1 Processing and as-received microstructure

The material used in this study (Cu-10at.%Ta) was produced by high energy cryogenic ball milling followed by equal channel angular extrusion, as discussed in chapter 3 (Darling et al. 2016). As-received microstructural characterization (**Figure 6**) using transmission electron microscopy (TEM) revealed the presence of Cu grains with an average size of 50 ± 18 nm as well as Ta particles. Processing produced a wide range of Ta particle sizes, ranging from atomic nanoclusters (≤ 15 nm) of average diameter 3.18 ± 0.86 nm to much larger sacrificial precipitates (>15 nm) of average diameter 32 ± 8 nm (Rajagopalan et al. 2017). Previous works had indicated that this material has coherent, semi-coherent, and incoherent Ta precipitates (diameters of <3.9 nm, 3.9–15.6 nm and >15. nm, respectively) (Darling et al. 2016). Further, the Ta nanoclusters also have misfit lattice dislocations at the interface with an average misfit strain of about 5.8%, but can be as high as 11% (Rajagopalan et al. 2017; Darling et al. 2016; Bhatia et al. 2017).

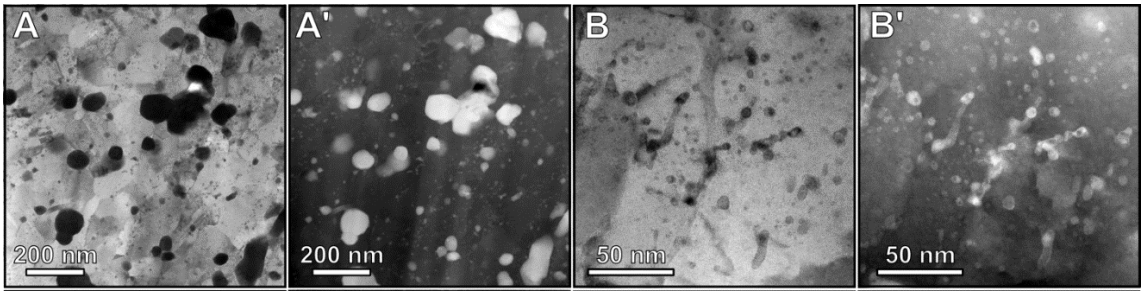

Figure 6: As-received microstructure. STEM images of unirradiated (A-B) NC Cu-10at. %Ta. (A') and (B') are the corresponding High Angle Annular Dark Field (HAADF) images to the Bright Field (BF) STEM images in (A) and (B) respectively. (Srinivasan et al. 2020)

4.2.2 Irradiation experiments and SRIM analysis

NC Cu-Ta cylindrical specimens with 3 mm diameter and ~1.2 mm tall, were mechanically polished to a mirror finish for irradiation experiment. A double charged copper beam ($^{63}Cu^{++}$) at 4 MeV was defocused to irradiate the specimen area on the stage. Defocused beam is considered better technique for simulating steady state damage than rastered beam since rastering suppresses the irradiation induced microstructure evolution like void nucleation and growth (Getto et al. 2015; Gigax et al. 2015). A flux of ~9 x 10^{12} ions cm^{-2} s^{-1} was used to achieve fluences of 2 x 10^{15} at room temperature (RT), 2 x 10^{16} at RT, 573 and 723 K, 2 x 10^{17} and 4 x 10^{17} ions cm^{-2} at RT and 573 K. SRIM damage profiles in displacements per atom (dpa, **Figure 7**), indicate damage level of 100 dpa near the surface (relatively flat) for the fluence 2 x 10^{17} ions cm^{-2}, with peak damage occurring at ~1.1 μm. Similarly, other fluences had a dpa of 1, 10 and 200 dpa at the surface respectively (Figure S1). Henceforth, nomenclature for the irradiated samples will correspond to the flat damage region on the surface, i.e., 1 dpa, 10 dpa, 100 dpa and 200 dpa. Approximate dose rates near the surface and peak damage were calculated to be 0.0045 and 0.015 dpa/s respectively. The depth range highlighted in green (away from the peak damage where the dose rate variation is relatively minimum) was utilized for analyzing the grain and void statistics.

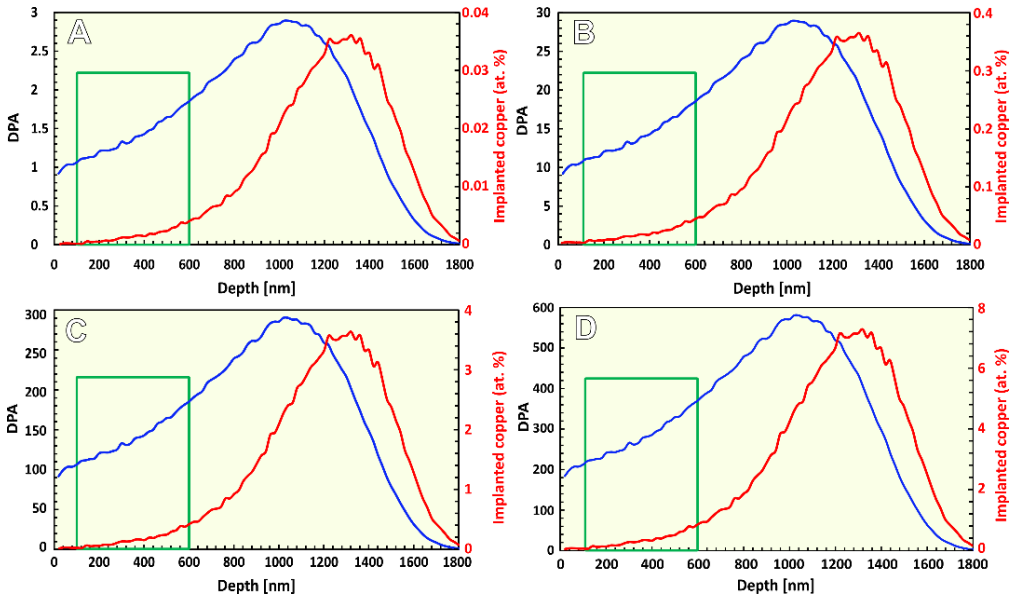

Figure 7: SRIM Damage profile. Dpa profile and implanted Cu in at. % for NC Cu-10at. %Ta irradiated with 4 MeV Cu^{++} ions to a fluence of (A) 2 x 10^{15}, (B) 2 x 10^{16}, (C) 2 x 10^{17} and (D) 4 x 10^{17} ions cm^{-2}. (Srinivasan et al. 2020)

4.2.3 Hardness Testing

Displacement controlled nanoindentation was carried out to obtain perspective on the radiation hardening behavior of the material at various doses. The surface was mechanically polished to mirror finish till 0.05 µm colloidal silica suspension before irradiation. Indentation depth was fixed at 200 nm to maintain a balance between the effect of plastic zone probing past the peak zone into the unirradiated region at higher depths and indentation size effects and surface effects at lower depth (Dolph et al. 2016; Duan et al. 2017)(Hosemann et al. 2012). A three segment quasi-static loading profile with load and unload period of 10.6 s and hold period of 7 s was utilized. A long dwell time is utilized to saturate creep effects on the contact area and stiffness. More than 25 indents were used for every condition to get good statistical information. Each indent was spaced 10 µm apart to avoid overlap of their radial plastic zones. Surface finish post irradiation was not affected

significantly due to sputtering till 100 dpa. Average hardness and standard deviation were calculated for every condition including the unirradiated sample and percentage increase in hardness was determined for each. Maximum Standard deviation for the indentation hardness was 7.5% indicating statistically precise measurements. However, at 200 dpa, the irradiated surface had high roughness due to the sputtering, and hence nanoindentation could not be carried out directly.

4.2.4 Grazing Incidence X-ray Diffraction experiments

To obtain X-ray signal within the damage depth, grazing incidence X-Ray diffraction scans were carried out at omega 2 degrees which gives an attenuation depth of nearly 750 nm in copper. A step size of 0.0125 degrees with a time per step of 0.2 s was utilized for the scans. Peak positions and intensity of Cu and Ta were analyzed to get some insight on lattice distortion and phase stability post irradiation. Error in lattice parameter measurements could arise from sample displacements and instrument misalignments such as peak positions and 2theta offsets (de Campos et al., n.d.). Calculations of standard deviation of peak positions between multiple measurements in as-received Cu-10Ta sample indicated an uncertainty of $< 0.05°$ in 2theta, which translates to an accuracy of >0.0035 nm in lattice parameter and >0.001% distortion in Cu and Ta peaks.

4.2.5 Microstructural characterization and TEM Sample Preparation

For transmission electron microscopy (TEM) characterizations carried out on ARM-200F, samples were prepared using a Focused Ion beam (FIB) FEI Nova 500 to get cross section liftouts of the irradiated region as described in chapter 3. EDS and EELS were

performed with a step size of 1 nm and a dwell time of 0.1 s. Grain size statistics were obtained from depths spanning 100-600 nm from the irradiated surface to minimize the effects of surface and interstitials in peak damage region. More than 150 grains were sampled for each irradiation condition using ImageJ software to get average grain size. Nanoclusters and voids statistics were determined with the help of HAADF (High Annular Angular Dark Field) images. Under and over focused TEM BF images were utilized to confirm small voids.

4.2.7 Atom Probe Tomography

APT was carried out in CAMECA Local Electrode Atom Probe (LEAP) 5000 XS instrument. The specimens irradiated to 100 dpa at RT and 573 K were lifted-out from the irradiated surface and welded to a pre-fabricated Si post using a Thermofisher Helios 660 dual-beam scanning electron microscope and focused ion beam (SEM/FIB) with a Ga source equipped with an EasyLift Nano-manipulator system. Specimens were then sharpened to a needle-shape geometry with a final tip diameter of 100 nm using annular ion beam milling at 30kV, followed by 1 kV cleaning. The field evaporation was performed at 30 K with a laser pulse energy of 50 pJ, auto pulse control limit of 300 Da and a target evaporation rate of 0.5 %. Clustering was evaluated through the cluster analysis functions in Integrated Visualization and Analysis Software (IVAS) utilizing the maximum separation algorithm as determined in (Hornbuckle et al. 2015).

4.3 Results and Discussion

4.3.1 Radiation Hardening

Radiation hardening is one of the major issues responsible for embrittlement of structural reactor components. Thus, to study radiation hardening behavior of NC Cu-Ta alloy, displacement-controlled nano-indentation experiments were performed on the irradiated surface (Experimental Section). Indentations were carried out at a depth of 200 nm, where the dpa profile is relatively flat. However, the measured hardness values correspond to a larger volume that spans a range of radiation doses higher than that for which they are reported, due to extension of the plastic zone generated from the indentation (Fischer-Cripps 2011). Post irradiation hardness data for NC Cu-Ta is plotted in supplementary **Figure 8**.

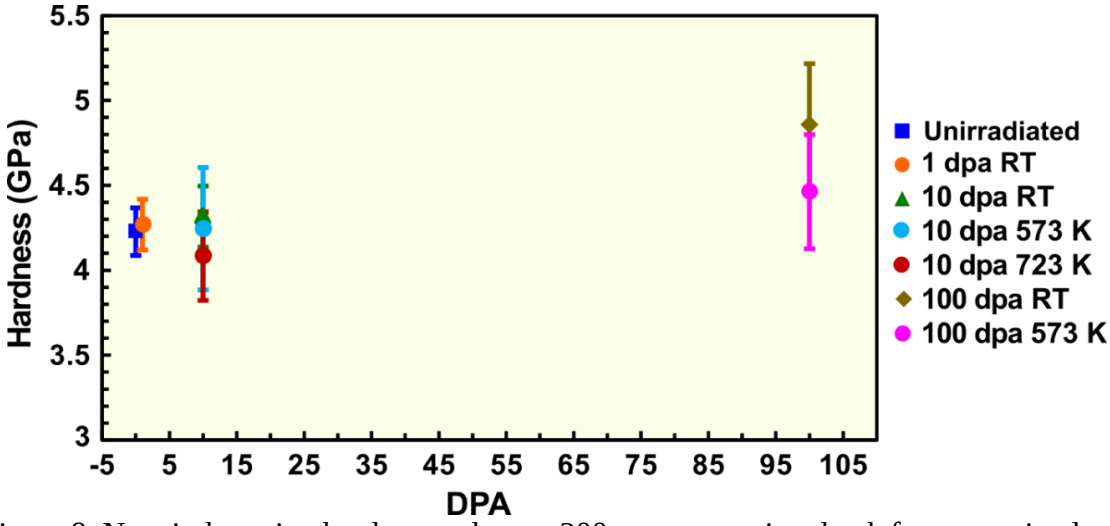

Figure 8: Nanoindentation hardness values at 200 nm penetration depth for as-received and irradiated Cu-10at.%Ta. (Srinivasan et al. 2020)

Figure 9 shows the change in hardness at 298 K and at 573 K for various irradiated alloys in comparison with NC Cu-Ta alloy. Note that for literature data, the values for

change in hardness have been obtained either through direct measurements such as nano-indentation/micro-indentation or indirect measurements such as tensile yield strength converted into hardness. In the case of radiation hardening at 298 K, (Figure 9A), the percentage change in hardness from as-received (0 dpa) to 1 and 10 dpa in NC Cu-Ta alloy is negligible. On the contrary, for similar dpa levels, the radiation hardening for coarse-grained pure Cu is about ~80% (24% at a very low dose of 0.034 dpa) (Mohamed et al. 2016) and that for nano-layered composites is about ~15% (Fu et al. 2013). Furthermore, at 100 dpa, NC Cu-Ta shows a hardening of mere ~15%, which is similar to the amount of radiation hardening observed in other materials at 1-2 dpa (Figure 3A). Hence, it can be inferred that NC Cu-Ta alloy has high-level of tolerance to radiation hardening at 298 K. Likewise, hardening comparison at 573 K, Figure 9B, shows some of the notable materials, the ferritic ODS steels and ferritic martensitic steels, experiencing a steep increase in hardness post-radiation at low to moderate damage levels. For instance, MA 957 shows a hardening of 7% at 6.5 dpa and 48% at 42 dpa (Alamo et al. 2007; Krumwiede et al. 2018). However, NC Cu-Ta alloy exhibits a paltry hardening of 0.4% and 5.5% at dose levels of 10 and 100 dpa, respectively at 573 K. Overall, it is evident that NC Cu-Ta alloy retains its hardness up to considerably high dose levels reached in generation IV reactors, indicating exceptional resistance to radiation hardening.

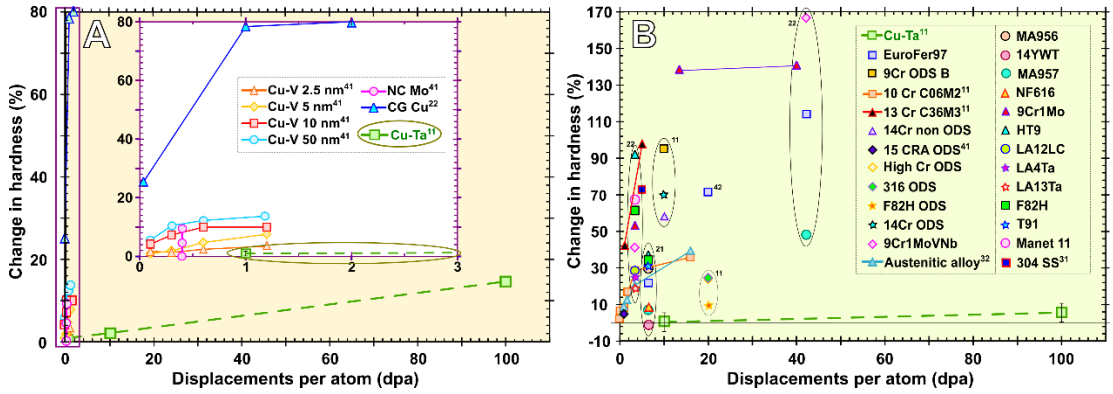

Figure 9: Percentage irradiation hardening for NC Cu-Ta and various materials from literature, at different doses irradiated at (A) 298 K and (B) 573 K *(Cheng et al. 2016; Mohamed et al. 2016; Alamo et al. 2007; 2000; Fu et al. 2013; Jiao and Was 2010; T. Zhang et al. 2014; Lupinacci et al. 2015; Fave et al. 2014; Krumwiede et al. 2018; Aydogan et al. 2018; Duan et al. 2017; C. Liu et al. 2011)*. Note that numbers in the super scripts (on legends and data points) represent irradiation ion type, and testing method carried out for calculating hardening respectively; where 1- Heavy/self-ion, 2- neutron, 3- proton and 4-helium ion, in the first letter of superscript and 1- Indentation and 2- Tension test, in the second letter of superscript. (Srinivasan et al. 2020)

4.3.2 Lattice stability

Radiation exposure is also known to cause lattice and phase instabilities leading to lattice distortion and disordering. Grazing incidence X-ray diffraction (GIXD) studies on NC Cu-Ta show a minimum lattice parameter change for all irradiation conditions (**Figure 10** and **Table 1**). Lattice contraction of ~0.7% (negligible considering experimental uncertainty) observed in Ta peaks at 200 dpa may be attributed to strain relaxation (processing induced). A similar structural contraction of ~1.42% was observed in NC ZrN upon increasing dose to 5 dpa after which the lattice contraction saturated (F. Lu et al. 2012). Additionally, high concentration of implanted Cu in the Ta precipitates at higher dose, could have also caused this contraction in Ta peak since the atomic radius of Cu is smaller than Ta. Further, XRD and TEM studies of helium ion irradiated Cu-V 2.5 nm

multilayers in literature had shown a peak lattice expansion of 1.2% at 5 dpa (Fu et al. 2013; X. Zhang et al. 2010). However, in NC Cu-Ta alloy, no significant distortion of copper lattice was observed up to a dose of 200 dpa. Further, a slight drop in Ta peak intensity relative to Cu, observed at higher doses (100 dpa and beyond) could be attributed to amorphization or dissolution of larger Ta particles. However, since no significant lattice expansion was observed in Cu peaks post irradiation (as expansion could indicate Ta entering Cu lattice as solid solution, as observed in as-milled Cu-Ta post mechanical alloying (Rojhirunsakool et al. 2015)), significant portion of dissolved Ta could be distributed as fine precipitates. An important takeaway from these results is that there is a minimal change in lattice parameter of Cu or Ta at very high doses, indicating the lattice stability of NC Cu-Ta system at very high dpa levels.

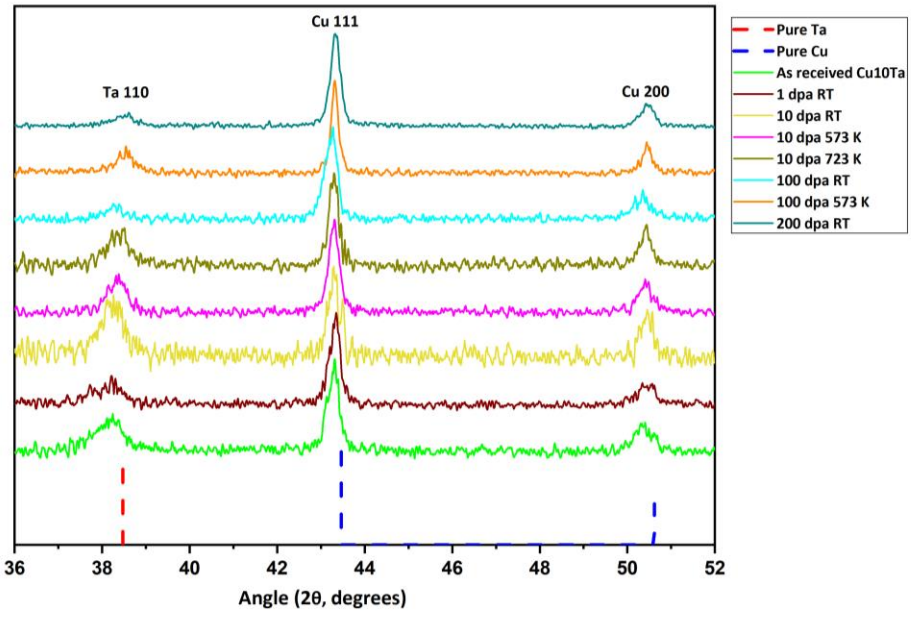

Figure 10: Grazing incidence X-ray Diffraction data for NC Cu-Ta irradiated at various conditions indicating negligible lattice distortion. The peak positions for pure Cu and Ta were taken from the ICDD database for comparison. (Srinivasan et al. 2020)

Table 1. Lattice parameter change measured from grazing incidence X-ray diffraction of Cu-10at.%Ta at high doses. Negative and positive sign indicates lattice contraction and lattice expansion respectively.

% Lattice distortion			
	Cu 111	**Ta 110**	**Cu 200**
100 dpa RT	0.096	-0.045	0.092
100 dpa 573 K	-0.028	-0.494	-0.179
200 dpa RT	-0.028	-0.652	-0.033

4.3.3 Microstructural stability and void swelling

To understand the extraordinary resistance to radiation hardening and lattice stability of NC Cu-Ta alloy, we drive our attention to post irradiation microstructural analysis at various damage conditions. **Figure 11** shows low and high magnification bright field STEM images of NC Cu-Ta alloy tested to a dose of 10 dpa at RT, 573 and 723 K, revealing several significant features. As observed in the **Figure 11**, microstructure of NC Cu-Ta alloy at 10 dpa showed a small increase in the average grain size from 50 nm in as-received microstructure to 90 nm at 10 dpa irrespective of the irradiation temperature even till 723 K.

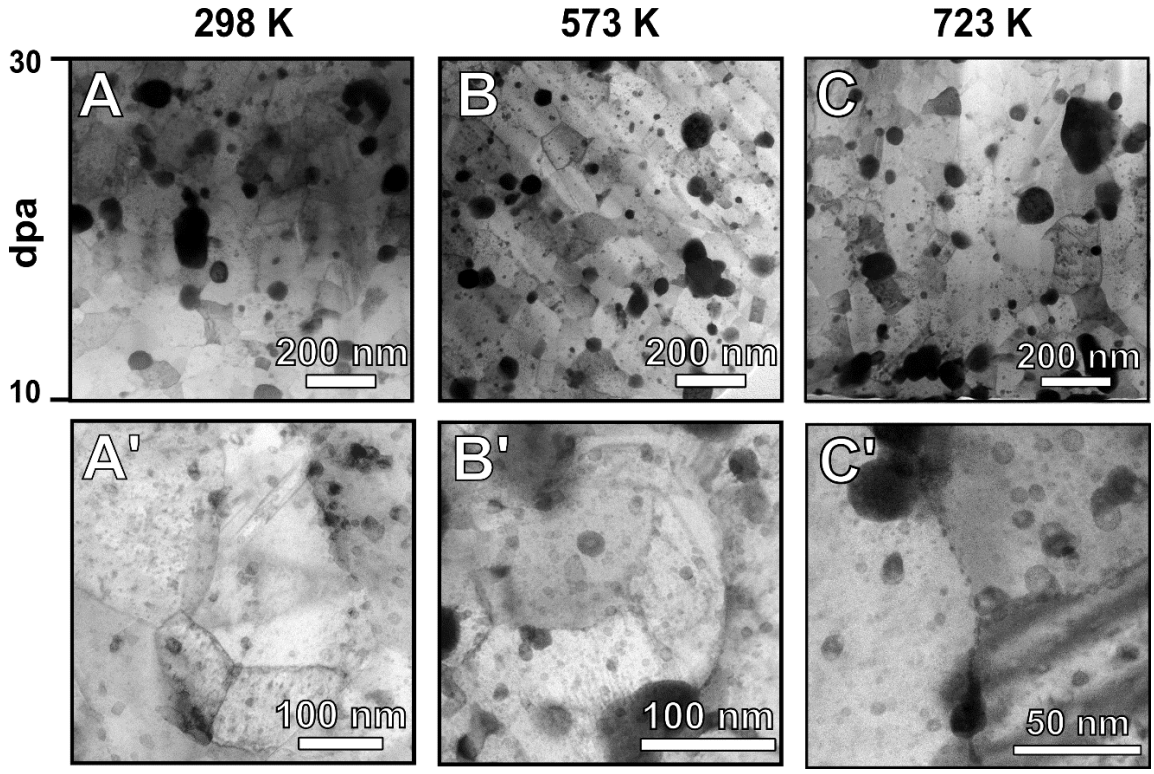

Figure 11: Cross section BF STEM images of NC Cu-Ta from the irradiated surface (bottom of each low mag image) to the peak damage region (refer figure 7), where the brighter grains are NC Cu and the darker grains/precipitates are Ta, of samples irradiated to 10 dpa at (A, A') Room temperature, (B, B') 573 K and (C, C') 723 K (Srinivasan et al. 2020)

Moreover, the grain size reached an average of 110 and 140 nm for 100 and 200 dpa respectively, with the irradiation temperature having a negligible effect as seen from **Figure 12**. The average grain size is thus maintained at nano regime even at such high dose, in comparison to the massive grain growth observed in NC Cu from ~48 to 800 nm at 1 dpa (Mohamed et al. 2016) and NC composite of Cu-0.5Al_2O_3 from 180 to 495 nm at 0.9 dpa (Xinghang Zhang et al. 2018). In other words, minimal grain growth and microstructural evolution in NC Cu-Ta signals that the stabilized grain boundaries (GBs) act as stable sinks and persist, thereby annihilating irradiation induced defects. In fact, earlier Precession Electron Diffraction (PED) studies on NC Cu-Ta alloy revealed a large

fraction of high angle GBs in the material (Rajagopalan et al. 2017), which are naturally more efficient defect sinks (Tschopp et al. 2012).

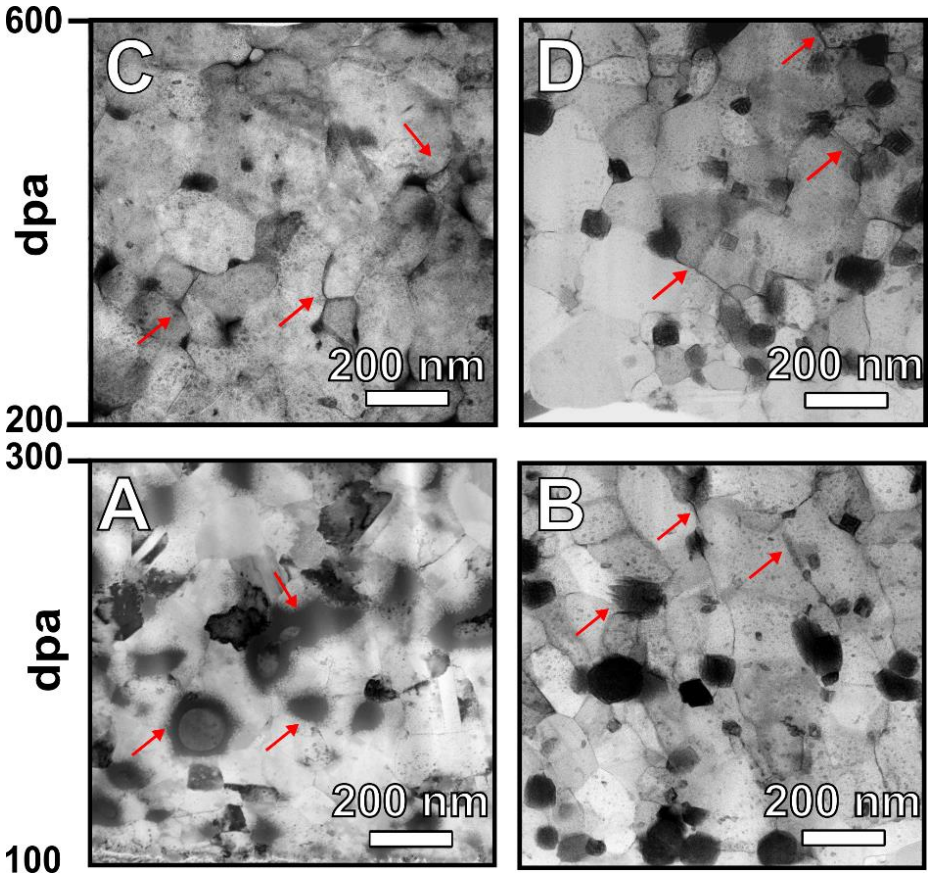

Figure 12: Cross section BF STEM images of NC Cu-Ta from the irradiated surface (bottom of each low mag image) to the peak damage region (refer figure 7), where the brighter grains are NC Cu and the darker grains/precipitates are Ta, of samples irradiated to (A-B)100 dpa at (A) Room temperature (B) 573 K and (C-D) 200 dpa at (C) Room temperature (D) 573 K (Srinivasan et al. 2020)

Further, BF TEM and STEM images showed no observed defects post irradiation. Zone axis imaging for the identification of radiation defects was challenging because of the nano-crystallinity of the alloy. HAADF images (which are purely phase contrast) were compared with their corresponding MAADF images (which gives diffraction contrast), to look for defects and differentiate them from Ta clusters.

4.3.4 Phase stability

Coherent/semicoherent interfaces of Ta nanoclusters in NC Cu-Ta alloy are key recombination sites for annihilation of vacancies and interstitials due to high as received misfit strain as discussed earlier. Moreover, the as received sink strength (using equation 2) for Ta nanoclusters (average diameter 3.18 nm and density $6.5x10^{23}/m^3$) is $1.3x10^{18}/m^2$, which is two orders of magnitude higher than that for GBs (average grain size 50 nm) with sink strength of $6x10^{16}/m^2$ in NC Cu-Ta. Further, the dense spacing between these nanoclusters of ~5 nm (Turnage et al. 2018; Kale et al. 2019) paves the way for overlapping defect denuded zones. Hence, it is paramount to investigate radiation effects on tantalum phase and interface stability including structure, size and density. Several mechanisms have been studied and reviewed on phase stability post-irradiation, which constitutes ballistic dissolution, Ostwald ripening, radiation enhanced diffusion and inverse Ostwald ripening (Wharry, Swenson, and Yano 2017; Allen et al. 2008; Russell, n.d.; Swenson and Wharry 2017). For instance, Chen et al. observed shrinkage and dissolution of the oxide particles in 12Cr ODS (Chen et al. 2015), while Lescoat et al. witnessed growth of oxides in ferritic ODS steels (Lescoat et al. 2011). In NC Cu-Ta alloy, as discussed earlier there are two types of Ta based phases: larger Ta sacrificial particles (>15 nm) and Ta nanoclusters (≤15 nm) both of whose stability with radiation are discussed in detail below.

To start with, the larger Ta sacrificial particles develop amorphous ring (**Figure 13 A**) due to ballistic mixing along the interface in room temperature irradiations where diffusion is sluggish, and at damage levels > ~20 dpa. This is confirmed using a selected area diffraction pattern on the region surrounding the tantalum particle irradiated to 100 dpa at

RT, which showed an obvious diffused ring at Ta (110) lattice spacing position (and a mild one at Ta 221) (**Figure 13** B). The halo size increases and becomes prominent with dose since ballistic mixing across the interface is proportional to the fluence. Excessive accumulation of defects and chemical disordering at the incoherent Ta interface due to the dense cascades has increased the free energy of the system enabling amorphization (Motta and Lemaignan 1992a). At 100 and 200 dpa and RT, the larger tantalum particles were also observed to undergo short-circuit diffusion along copper grain boundaries with minimum/no amorphization observed at 200 dpa and RT (**Figure 13** D-E). The observed disordering (mixing) could thus, be a precursor/transient state for dissolution of the tantalum particles. Computational studies have shown similar amorphization due to shear induced chemical mixing at the precipitate-matrix interfaces of Cu-Nb (4 at.%) and Cu-V (8 at.%), which increased linearly with particle radius (Ashkenazy et al. 2012). It was also reported that semi-coherent interfaces were more stable and resistant to amorphization. Moreover, Sauvage et.al reported that the amorphous interface they observed post wire drawing in Cu-Nb were associated with very fine precipitates due to mixing of Cu and Nb (Sauvage et al. 2001).

Furthermore, interestingly with some incubation time in the room temperature irradiations of 100 dpa and 200 dpa, voids were observed in some of the larger Ta interfaces (**Figure 13** C and F respectively). Nevertheless, the swelling observed was as low as ~0.2% compared to 0.5% observed in a ODS ferritic alloy MA 957 at 100 dpa under 823 K (Toloczko et al. 2004). At very high dose of 200 dpa at RT, few regions were observed to show continuous voids especially along copper GBs and larger Ta interfaces (Figure 13F)

but still with no significant swelling. However, for the irradiation conditions such as 100 and 200 dpa at 573 K and lower dose cases (See Figures 11 &14), no voids could be detected illustrating swelling resistance of NC Cu-Ta alloy at such high dose levels.

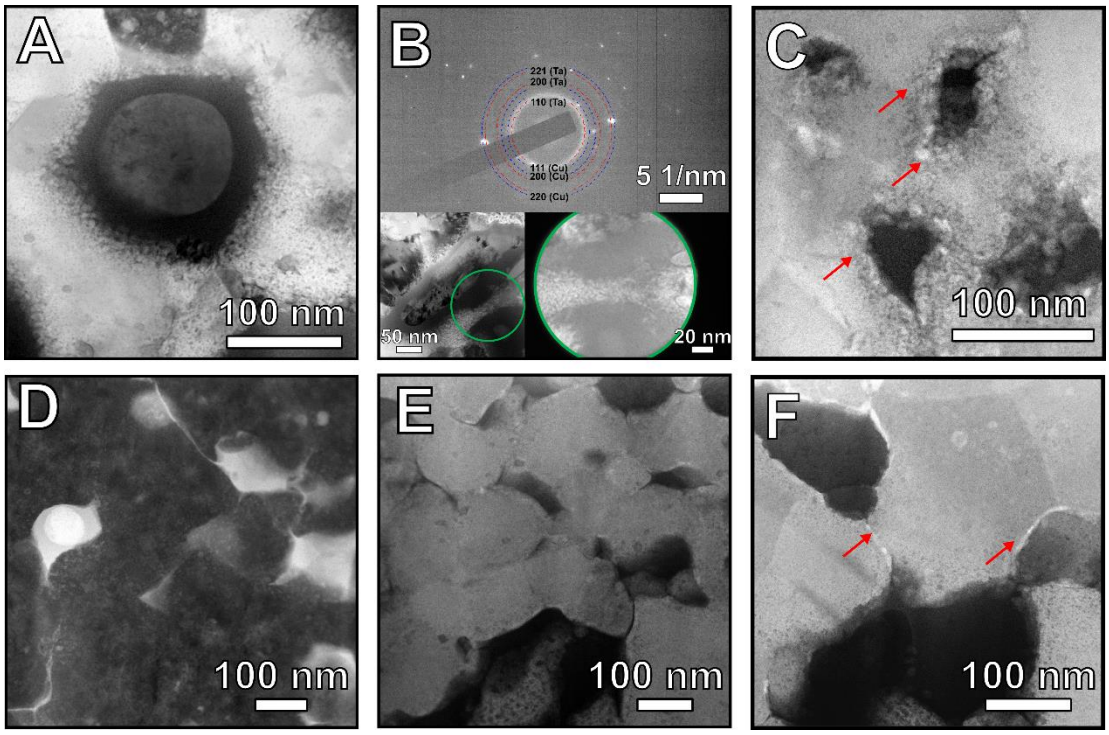

Figure 13: Large Tantalum phase post irradiation at room temperature (A-C) 100 dpa and (D-F) 200 Dpa. (A) Amorphous ring in large Ta phase in 100 dpa RT (~400 nm from irradiated surface), (B) SAED of the amorphous region around Ta with the area used to take SAED in 100 dpa at RT (~200 nm from the irradiated surface). Standard lattice spacings for Cu (blue) and Ta (red) are overlaid to the SAED pattern. (Srinivasan et al. 2020)

Alternatively, in the corresponding 573 K irradiations (**Figure 14** A and B), where diffusion is significant for thermal reordering, larger Ta sacrificial particles do not exhibit any disordering. Existence of critical amorphization temperature has been confirmed in many previous studies. For instance, Ribis et al. (Ribis et al. 2011) showed amorphization of ODS particles at RT while regaining crystallinity at 773 K, and Lescoat et al. observed

amorphization of oxide particles (>50 nm) in ODS steels with existence of critical amorphization temperature (Lescoat et al. 2011). Moreover, mixing/dissolution of solute in the solvent lattice in "driven" alloys is a result of competition between forced mixing (ballistic effects) and thermal diffusion, where the forcing parameter 'γ' (given by $\gamma = \Gamma_b/\Gamma_t$ (UENISHI et al. 1992)), decreases with temperature.

Additionally, in high dose cases (≥100 dpa) at 573 K, the large Ta particles developed a patterned structure with implanted Cu atoms as observed in Figures 6(E-F) due to the energetic recoils. Energy dispersive spectroscopy (EDS) line scans (**Figure 14** C and C') along the pattern, confirmed an increased concentration of Cu and a depletion of Ta in patterned regions within the Ta particles, indicating knock out of Ta atoms by implanted Cu atoms. As Cu and Ta are phase separating (positive enthalpy of mixing), at elevated temperatures the implantation of Cu leads to a re-arrangement and the development of a spinodal microstructure through short-range diffusion. In addition to the Cu ion implantation, the large Ta particles has undergone ballistic dissolution within the surrounding microstructure (**Figure 14** A and B). The Nelson, Hudson, and Mazey (NHM) model describes precipitate dissolution at a displacement rate *k*, due to scattering of atoms from precipitates of radius r_p, number density ρ, and solute concentration C_p, through the following equation (Nelson, Hudson, and Mazey 1972; Wilkes 1979),

$$\frac{dr_p}{dt} = -yk + \frac{3DC}{4\pi r_p C_p} - r_p^2 D\rho \tag{9}$$

where *C* is the total solute concentration, *D* is the solute diffusion coefficient, and *y* is a constant representing thickness of atom layers scattered from the precipitate per dpa.

Considering sputtering of tantalum atoms, the NHM model suggested a y-value of 10^4 cm/dpa, which was utilized for the calculation. Using the above equation for a Ta particle of average radius 25 nm (from TEM), a negative rate of change was calculated (i.e., $dr/dt < 0$), indicating dissolution of large Ta particles.

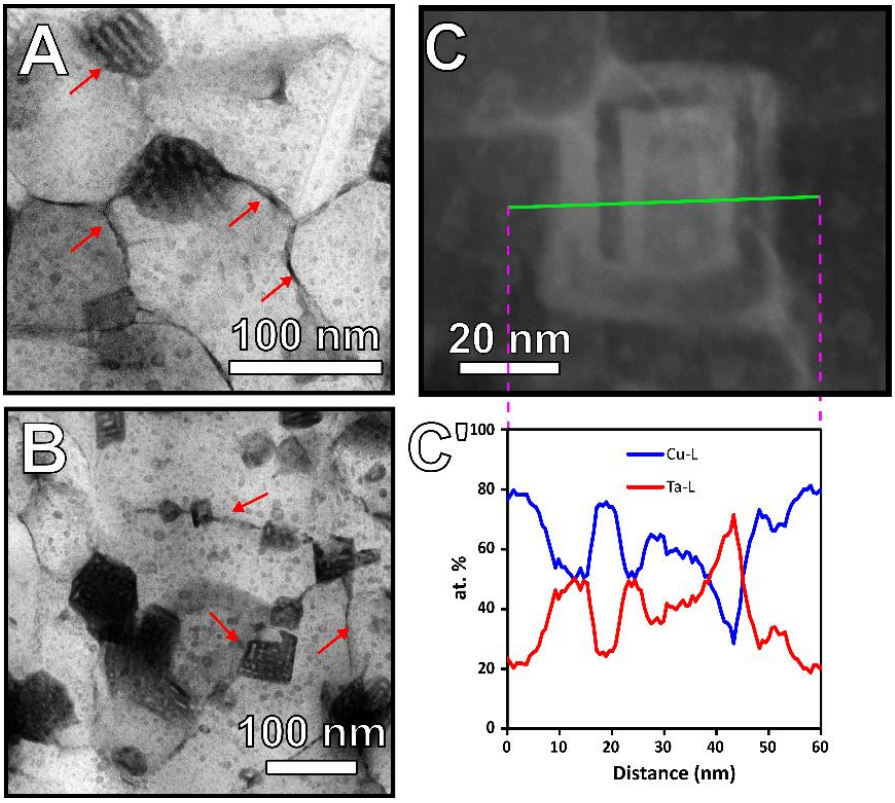

Figure 14: (A-B) STEM BF images from 100 and 200 dpa and 573 K respectively of large Ta precipitate with implanted copper, where Ta is ballistically ejected to surrounding lattice and grain boundaries (C) HAADF image of a Ta particle with patterns of implanted copper where tantalum is ballistically ejected, (C') Line scan of the highlighted area in C showing an increase in copper and decrease in tantalum concentration in the patterned region within the tantalum particle indicating knocking out of tantalum by implanted copper. (Srinivasan et al. 2020)

Dissolution of the larger particles led to a local enrichment of Ta solute in the nearby (surrounding) lattice regions. However, as the material was irradiated further (Radiation enhanced diffusion) and the temperature increased (γ reduces), these supersaturated Ta

regions began to form nanoclusters (**Figure 15 (B-C)**), a process which requires diffusion-controlled redistribution of Ta. We emphasize that this process under non-irradiated conditions is only possible along GBs, which offer faster diffusion pathways; since it cannot occur in the Cu lattice, where Ta diffusion is extremely slow even near the melting point. Moreover, under irradiation, the tendency to form Ta nanoclusters may be similar in atomic origin to the formation of stable nano emulsions found in liquid Cu–Ta alloys, stabilized by a negative and strongly curvature-dependent tension of the Cu-Ta interfaces (Frolov and Mishin 2010), which limit any coarsening due to balance between the deterministic reaction and very slow stochastic lattice diffusion force. Such an analogy is supported by the high degree of intense cascading effects, which saturates the structure with point defects. This disordered state offers a "liquid-like" environment for nanocluster formation and provides a pathway for local short-circuit diffusion for Ta redistribution within the lattice. Analogous to the stabilized nano-emulsions of Cu-Ta reported by Frolov et al. (Frolov and Mishin 2010), these newly generated Ta based clusters also resist coarsening despite the intense irradiation and temperature exposure, retaining an average diameter < 10 nm.

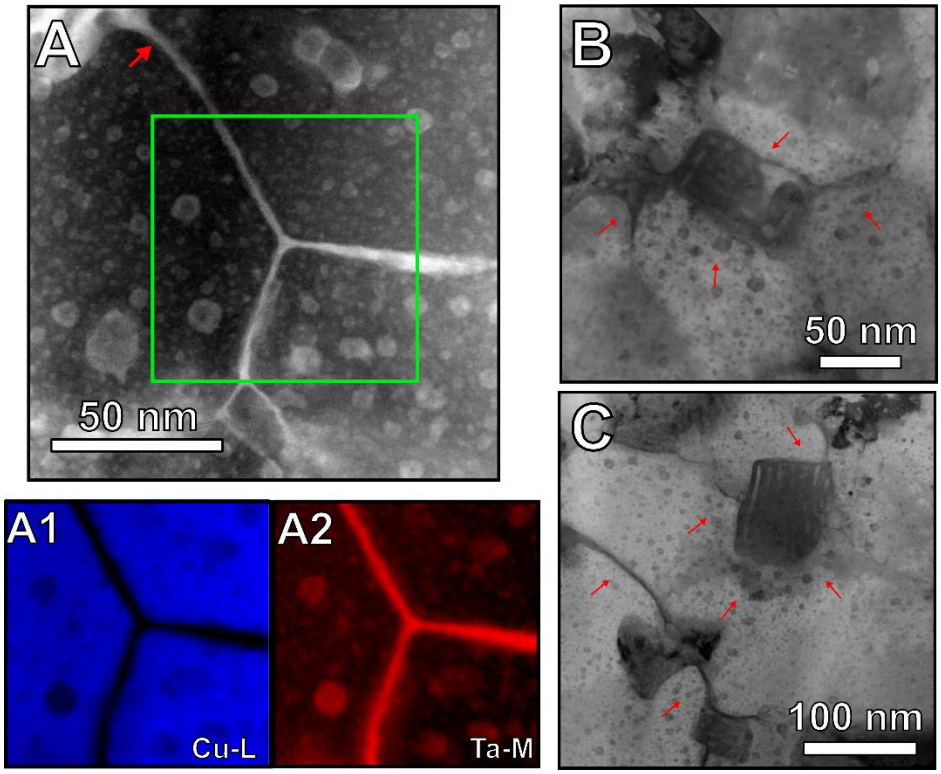

Figure 15: (A) HAADF image of a Cu10at%Ta tested at 200 dpa and 573 K showing a dissolving Ta particle preferentially diffusing along a GB, (A1-A2) EELS Cu-K map in blue and Ta-L map in red, of the region highlighted in green in C, showing diffusion of tantalum along grain boundaries, (B-C) STEM BF images from 200 dpa and 573 K of large Ta particle with implanted copper (~300 and 600 nm from irradiated surface respectively), where Ta is ballistically ejected to lattice and grain boundaries and increased density of Ta nanoclusters in the nearby region indicating re-precipitation after dissolution. (Srinivasan et al. 2020)

In addition to Ta saturation within the lattice, electron energy loss spectroscopy (EELS) analysis along a GB triple junction (**Figure 15**(A-A2)) in a 200 dpa 573 K sample showed that these regions were also being enriched with Ta solute from nearby large Ta particles, which were undergoing ballistic dissolution. Marwick had speculated such segregation of slow diffusing solute elements (inverse Kirkendall effect) to the sinks due to difference in vacancy diffusion coefficients of the alloy constituents (Marwick 1978). The Ta solute atoms diffusing along the intergranular regions are eventually precipitated as nanoclusters due to supersaturation of Ta solute, resulting in a high cluster density within

these regions as well (Figure 15A). Russell had predicted this behavior of dissolution and re-precipitation of second phase particles due to recoils, where the dissolved large particle will be replaced with finer particles with continued irradiation (Russell 1993). Likewise, Chen et al. and Lu et al. have reported dissolution of larger particles and precipitation of fine dispersoids in ODS alloys after high dose self-ion and helium pre-implanted self-ion irradiations respectively (Chen et al. 2015; C. Lu et al. 2017). While Certain et al. observed dissolution of nanoclusters in 14YWT at low temperatures while being stable at high temperatures, due to diffusion of dissolved solute back to the parent cluster, with no new precipitation (Certain et al. 2013). Atom probe analysis in **Figure 16** provided additional proof of short-circuit diffusion in the form of compositional modulation along the GBs due to decrease in total surface energy of the Ta phase, which is the precursor to cluster formation (Figure 16C). Correspondingly, the role of this short circuit diffusion of Ta at mobile GBs has been analyzed previously and has been shown to leave behind residual clusters within the lattice; thereby allowing a second mechanism to increase sink concentration (Figure 16D and E) (Koju et al. 2016).

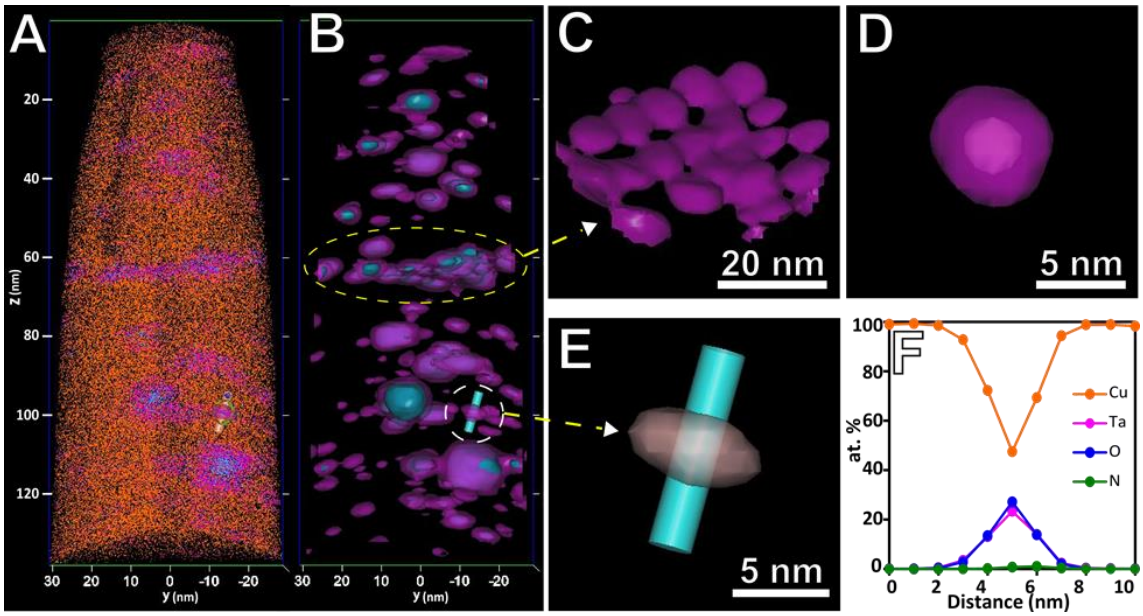

Figure 16: (A) Atom distribution map of APT specimen prepared from the irradiated surface (to a depth of 140 nm) of 100 dpa irradiation at 573K, where Cu is shown in orange, Ta in purple and O in blue; (B) Ta and O delineated with 5 at. % Ta iso-concentration surface in purple and 21 at. % O iso-concentration surface in blue; (C) GB circled in (B) showing continuous Ta interface along the grain boundary; (D) 5 at.% Ta iso-concentration surface surrounding a 21% O iso-concentration surface, representing a core-shell structured Ta particle; (E) A cylinder passing through the Ta particle circled in (B); (F) 1D concentration profile generated from the cylinder shown in (E), showing a representative chemical composition for the Ta precipitates. (Srinivasan et al. 2020)

Moreover, it is interesting to note that the ascribed microstructural evolution process observed from irradiating this matter at elevated temperatures is similar to the mechanical dissolution experienced during the initial synthesis of the material via high energy mechanical alloying. That is, synthesis through ball milling also introduces a high density of non-equilibrium linear and point defects, as well as the creation of super saturated solid solutions. This combination leads to enriched Ta regions which evolve through phase separation and short-circuit diffusion at elevated temperatures to yield increased cluster densities and homogenous dispersions. This microstructure can then be restored to the initial state of dissolution through application of additional mechanical alloying and the

generation of new defects in a repetitive manner yielding the final-end state each time. This idea of rejuvenation through mechanical alloying is analogous to the irradiation process where larger particles can be re-dissolved and smaller particles precipitated and coarsened, which is typically a dynamic balance between the ballistic mixing effects and thermal diffusion induced decomposition in a driven system. Interestingly, even with the application of high dose of radiation and temperature, the rate of coarsening of the small clusters (< 10nm) is still extremely sluggish as noted in TEM images, and the core-shell structure of the nanoclusters with oxygen rich core also seems to be maintained post irradiation (**Figure 17)**. This is only possible through the radiation induced generation and decomposition of metastable solid solutions, in a system with a positive enthalpy of mixing between the respective constituents. Such an analogy will hold true as long as the system remains free of minor constituents that would form ordered or ceramic phases, and the precipitating phase is in surplus to those as in the case of Ta in Cu. Various computational and experimental studies have exploited the role of compositional self-organization (steady state) in binary alloys with positive heat of mixing, observed at a specific range of temperature and shearing rates, in maintaining refined microstructure during high temperature irradiations or ball milling for long durations (Enrique and Bellon 2000; Pochet et al. 1996; Enrique and Bellon 2001). Further, Chee et. al. reported the maximum temperature of patterning regime (temperature for microscopic coarsening, T_{max}) for various Cu based alloys, where systems with high positive heat of mixing like Cu-Nb and Cu-V experienced a higher T_{max} (>773 K) (Chee et al. 2010). Additionally, high density of sinks have been predicted to have a positive role in stabilizing irradiation induced

patterning (Shu, Bellon, and Averback 2015). No evident coarsening of clusters in NC Cu-Ta even at 723 K could indicate a large patterning regime due to high sink density and positive enthalpy of mixing, which is an area to be explored further in detail.

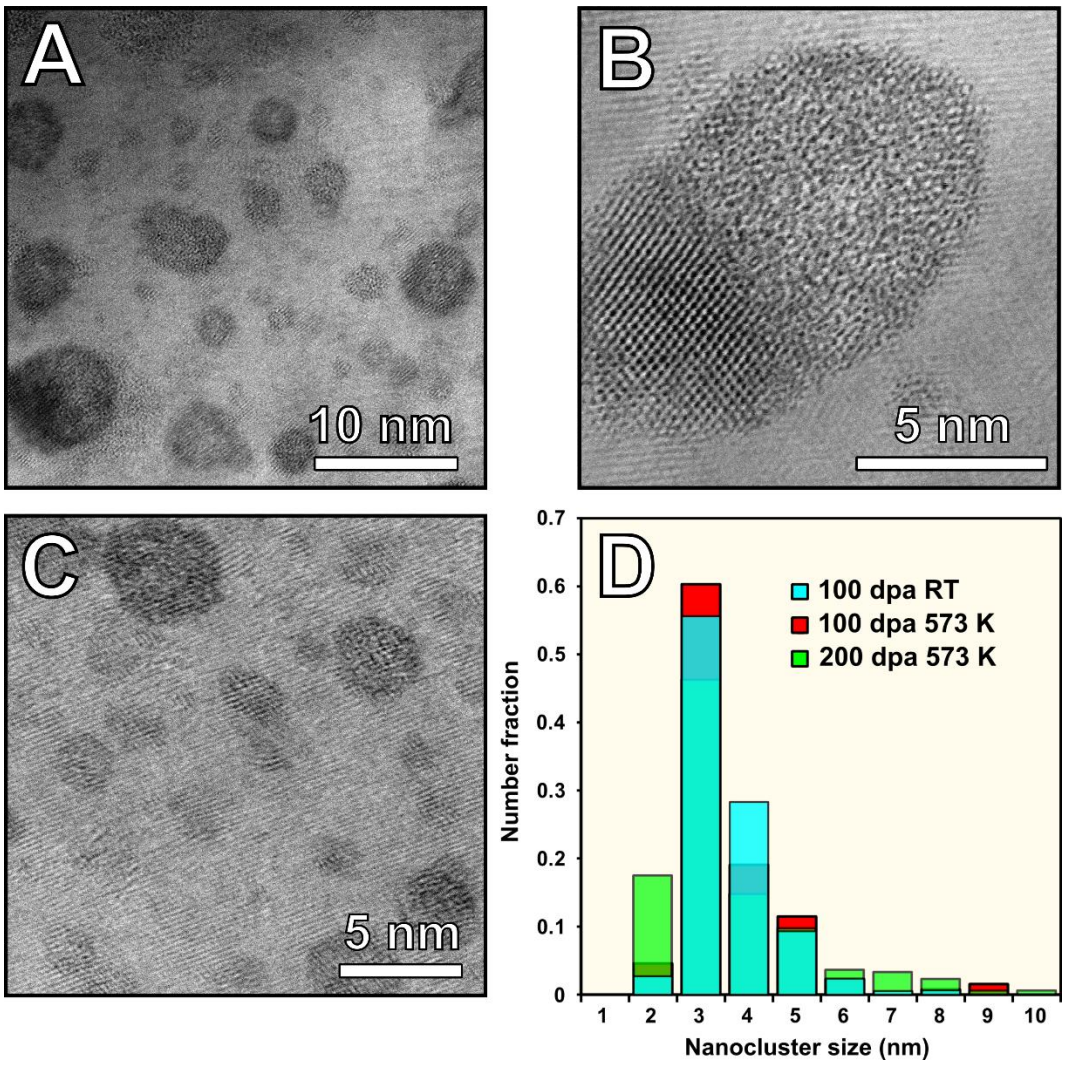

Figure 17: Ta nanocluster stability. (A-B) HR BF STEM image of a Ta cluster in 10 dpa at 723 K, (C) Ta NCs shown for 200 dpa RT, exhibiting stable core-shell microstructure (D) Tantalum nanocluster size distribution calculated from APT for 100 dpa RT and 100 dpa at 573 K is in good agreement with 200 dpa at 573 K calculated from TEM. (Srinivasan et al. 2020)

Altogether, the response of NC Cu-Ta at each damage level and temperature, with respect to grain growth and phase changes is depicted in **Figure 18,** where initial grain

growth observed till 10 dpa (possibly due to dissolution of clusters), gets saturated at 100 dpa and beyond due to precipitation of more new clusters pinning the grain boundaries. Ballistic mixing at RT in the Ta interface induces dissolution at doses ≥ 100 dpa. As the dose and temperature increases, short circuit diffusion of Ta occurs through grain boundaries and phase separation gains dominance, thereby precipitating more smaller clusters from the supersaturated regions and replenishing the sink density. Therefore, designing alloys employing positively phase separating elements in their makeup with sacrificial phases, plays a key role in developing radiation tolerance whereby the number of available interfaces acting as potent and stable sinks is increased significantly as demonstrated here. Thus, this paves a pathway for development of cutting-edge structural materials for extreme radiation applications, such as space exploration and next generation nuclear reactors.

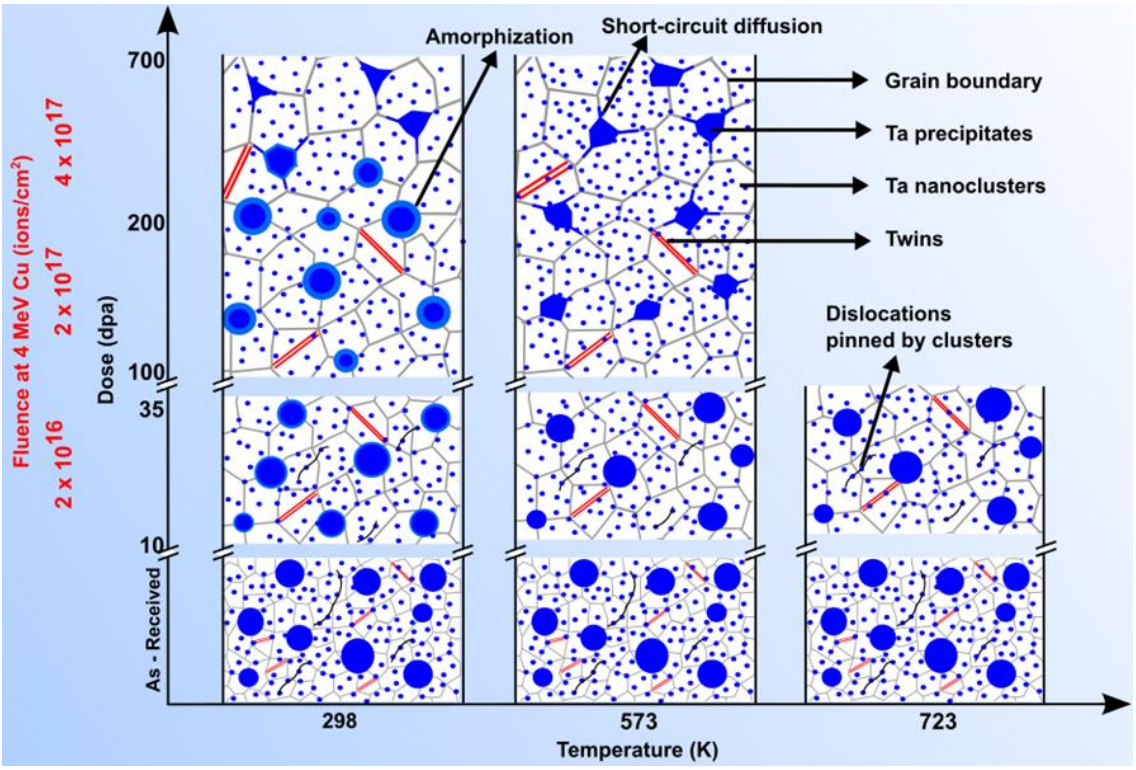

Figure 18: Radiation response mechanism in nanocrystalline Cu-Ta. Condensed microstructural response and phase changes in NC Cu-Ta at different irradiation conditions characterized in this study. Copper matrix is represented in white and the blue blobs represent tantalum. (Srinivasan et al. 2020)

4.4 Conclusions

In summary, an exceptional radiation tolerance along with microstructural stability in an immiscible NC Cu-10at.% Ta is experimentally demonstrated and the following important conclusions can be drawn:

- Very minimum radiation hardening at room temperature and 573 K, up to 100 dpa, as compared to many advanced structural materials from literature.

- Marginal increase in grain size from 50 nm in the as received condition to around 110 nm and 140 nm at high doses of 100 and 200 dpa respectively, with negligible effect of irradiation temperatures on the grain size.

- A very low swelling % was observed at 100 dpa (0.2%) and 200 dpa at room temperature, while no voids were observed at the corresponding 573 K irradiations and other lower doses, indicating remarkable swelling resistance.

- The larger Ta phases disintegrate and segregate along copper grain boundaries and eventually re-precipitates as Ta rich nanoclusters at high doses (≥ 100 dpa), with no apparent coarsening of the nanoclusters.

The key aspects for the observed radiation response are, the stability of nanoclusters which is partly attributed to emulsion-like behavior due to the phase separating nature of the material system; and their replenishment by the dissolution of sacrificial phase. This enables restoring the microstructure to initial state with additional doses in a repetitive manner, evolving a self-healing mechanism in the material while maintaining superior mechanical strength and temperature properties.

CHAPTER 5

5 HELIUM PARTITIONING TO TANTALUM NANOCLUSTERS IN NANOCRYSTALLINE CU-10TA

5.1 Introduction

Major development of advanced structural materials for next generation reactors is challenging due to harsh reactor environment viz. high energy neutron exposure, temperature and corrosion environment (Murty and Charit 2008; S.J. Zinkle and Was 2013). In addition to the displacement cascade caused by high energy radiation, Helium, generated by nuclear (n, α) reactions is particularly more detrimental as it exacerbates the effects from displacement damage. Due to its low solubility in metals and high binding energy with vacancy, helium tends to exist as helium vacancy complexes, thereby stabilizing the vacancy clusters (from reemission) and forming helium bubbles, which grows further to large voids (S.-H. Li, Li, and Han 2019; Farrell 1980; Trinkaus and Singh 2003; Lucas 1984). These defect interaction (low migration energy of helium) and complex microstructural evolutions (with T, dose, dose rate, He conc), aggravates the radiation-induced degradation through void swelling, surface blistering and helium embrittlement (Dai, Odette, and Yamamoto 2012).

Increasing the interface concentration that acts as sinks for the radiation induced defects such as grain boundaries, phase boundaries and dislocations have been explored and are believed to be promising strategies to alleviate radiation effects (Xinghang Zhang et al. 2018). For instance, experimental evidence has shown that refining grain size down to nano

can improve radiation tolerance significantly (El-Atwani et al. 2017), provided the microstructure is stable. Likewise, many studies have reported enhanced radiation resistance of ODS and NFA (Nanostructured Ferritic alloys) compared to conventional austenitic, RAFM steels attributed to the high density of uniformly dispersed nano-oxides (Hoelzer et al. 2020; Odette and Hoelzer 2010). Metallic nanolayers (e.g., Cu-Nb, Cu-Mo and Cu-V) are another attractive group of materials widely researched at different layer thickness validating the importance of interface concentration in effective suppression of radiation induced defects and helium bubble swelling (Demkowicz, Misra, and Caro 2012; W. Han et al. 2013). Specifically, immiscible and semi-coherent (e.g., fcc/bcc) interfaces have been proclaimed to offer promising radiation tolerance compared to their miscible (e.g., Al/Nb, Fe/W) and coherent (e.g., fcc/fcc: Ag/Ni) counterparts due to the presence of a large concentration of misfit dislocations at their interface (X. Zhang et al. 2010; Yu et al. 2013; N. Li, Martin, et al. 2009; N. Li, Fu, et al. 2009).

The motivation of this study is to understand the cumulative defect trapping efficiency and stability of a material system possessing a combination of immiscible heterophase interfaces and nanocrystalline grain boundaries decorated with nano precipitates to intense helium concentrations. One such immiscible system: bulk Cu-10at.%Ta, with nanocrystalline microstructure and bimodal distribution of precipitates (nanoclusters and large particles) has shown promising radiation tolerance to high dose heavy ion irradiation (Srinivasan et al. 2020). Thus, we use this immiscible Cu-Ta system (Cu-10at.% Ta) with numerous immiscible fcc/bcc interfaces, to evaluate the stability and tolerance of such a system to high helium and temperature levels.

5.2 Methodology

5.2.1 Irradiation experiments and SRIM analysis

NC Cu-Ta cylindrical specimens with 3 mm diameter and ~1.2 mm tall, were mechanically polished to a mirror finish and irradiated with 200 keV helium ions. The beam was raster scanned with a frequency of ~1.1 kHz in x and y. A flux of 1.85×10^{13} ions cm^{-2} s^{-1} in a Danfysik implantor was used to achieve a fluence of 1×10^{17} ions cm^{-2} at room temperature (RT) and 723 K. The samples were mounted to the heating stage with silver paste for good thermal conduction and the stage temperature was monitored through a thermocouple attached to the stage. Depth-dependent damage and ion concentration profiles were calculated using Stopping and Range of Ions in Matter (SRIM) software utilizing the Kinchin Pease model, which gives the best correlation with the internationally adopted Norgett, Robinson, and Torrens (NRT) displacement model (Stoller et al. 2013). The simulation was performed for Cu-10at.%Ta with threshold displacement energy of copper and tantalum set to 30 eV and 90 eV respectively ("Standard Practice for Neutron Radiation Damage Simulation by Charged-Particle Irradiation" 96). Damage profiles in displacements per atom (dpa, **Figure 19**), indicate a damage level of 0.5 dpa near the surface (relatively flat), with peak damage of 2.5 dpa occurring at 0.5 μm and peak helium concentration of 4 at.% at 0.7 μm.

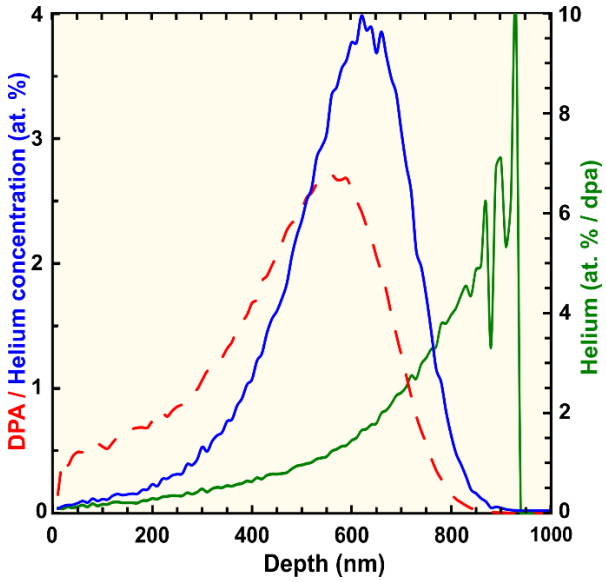

Figure 19: SRIM Damage profile. Dpa profile and helium concentration in at. % for NC-Cu-10at. %Ta irradiated with 200 keV He^{++} ions to a fluence of 1 x 10^{17} ions cm^{-2}.

5.2.2 Microstructural and Atom probe characterization

For transmission electron microscopy (TEM) characterizations carried out in ARM-200F, samples were prepared using a Focused Ion beam (FIB) FEI Nova 500 to get cross section liftouts of the top irradiated region of interest which were thinned to electron transparency till 2 keV and were plasma cleaned in Ar prior to TEM observations to reduce contamination. Bubbles were visualized using the phase contrast HAADF STEM images. Bubbles and Grain statistics were obtained by area method calculated using ImageJ software. Atom probe analysis was carried out similar to the procedure outline in section 4.2.7.

5.3 Results and Discussion

5.3.1 Bubble distribution

At room temperature, few tiny helium bubbles of ~1-2 nm start to be observed at the Ta nanoclusters at the irradiation depth of >200 nm. When moved further down at ~400 nm, in addition to the bubbles observed at the nanoclusters, minute bubbles of <1 nm were found in a few regions to be uniformly distributed in the matrix as seen from the HAADF images in **Figure 20** (B2 and B3). Furthermore, at the peak damage region, small bubbles were also observed along few grain boundaries (**Figure 20** B2) and some larger Ta precipitate interfaces as well (**Figure 20** B4). Nevertheless, the bubbles at these grain boundaries remained small (~2nm) potentially due to the sequestering effect from tantalum nanoclusters present at the grain boundaries minimizing and increasing the threshold for coalescence. Considerable fraction of bubbles (2-3 nm) was observed at the nanoclusters and interestingly more along the defected core of the core-shell structure exhibited by these nanoclusters in addition to their interfaces.

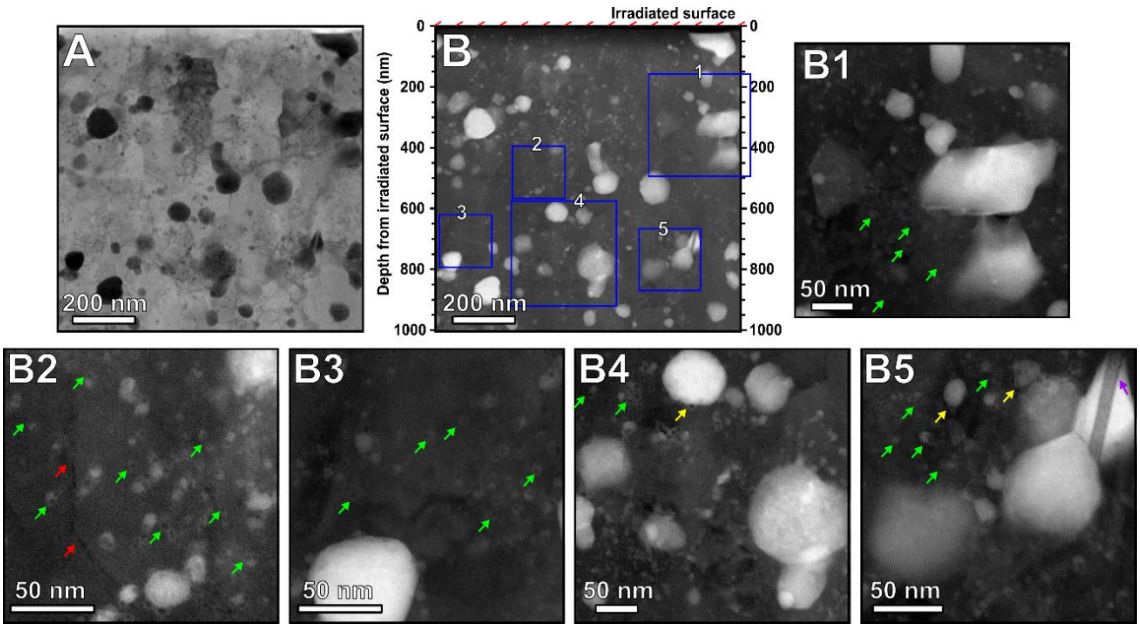

Figure 20: Helium bubble distribution at room temperature. (A) Low magnification BF STEM image showing the complete damage region from the irradiated surface. (B) Corresponding HAADF STEM image of A. B1-B5 represents high magnification HAADF image at various irradiation depth in image B. Arrows point to bubbles at various interfaces such as Red- Grain boundaries, Yellow-Large Ta interfaces and Green- Ta nanoclusters.

Microstructure evolution at various irradiation depths for the specimen irradiated at 723 K is shown in **Figure 21**. No bubbles could be detected below ~180-200 nm, indicating a critical helium concentration of ~0.17 - 0.2 at.% He required for bubbles to initiate and to be observed at Ta nanoclusters. In other words, critical helium concentration per interface area in Cu-Ta is ~7.8-9.9 atoms/nm^2. At depth levels of around 200-400 nm (0.2-1 at.% He), small bubbles of 2-3 nm were observed primarily along the Ta nanoclusters and few grain boundaries indicating the preference of helium bubbles to segregate to these interfaces before aggregating at the matrix or grain boundaries. No bubbles were observed in the bulk (within the grains). At further higher doses (>400 nm) close to the peak damage region (1-4 at.% He), larger bubbles of size 4-5 nm were observed along the grain boundaries (**Figure 21** A5-6) and within the grains (**Figure 21** A7-8). At the peak helium

concentration zone, the largest bubble observed was around 10 nm with no evident faceting observed. Even at the peak helium concentration, many of the bubbles associated with the nanoclusters in both matrix and grain boundaries were observed to remain within 3-4 nm indicating the potential of these clusters in resisting bubble coarsening (**Figure 21** A3&8). Furthermore, SEM imaging of the irradiated surface showed no prominent blistering for both room temperature and 723 K conditions.

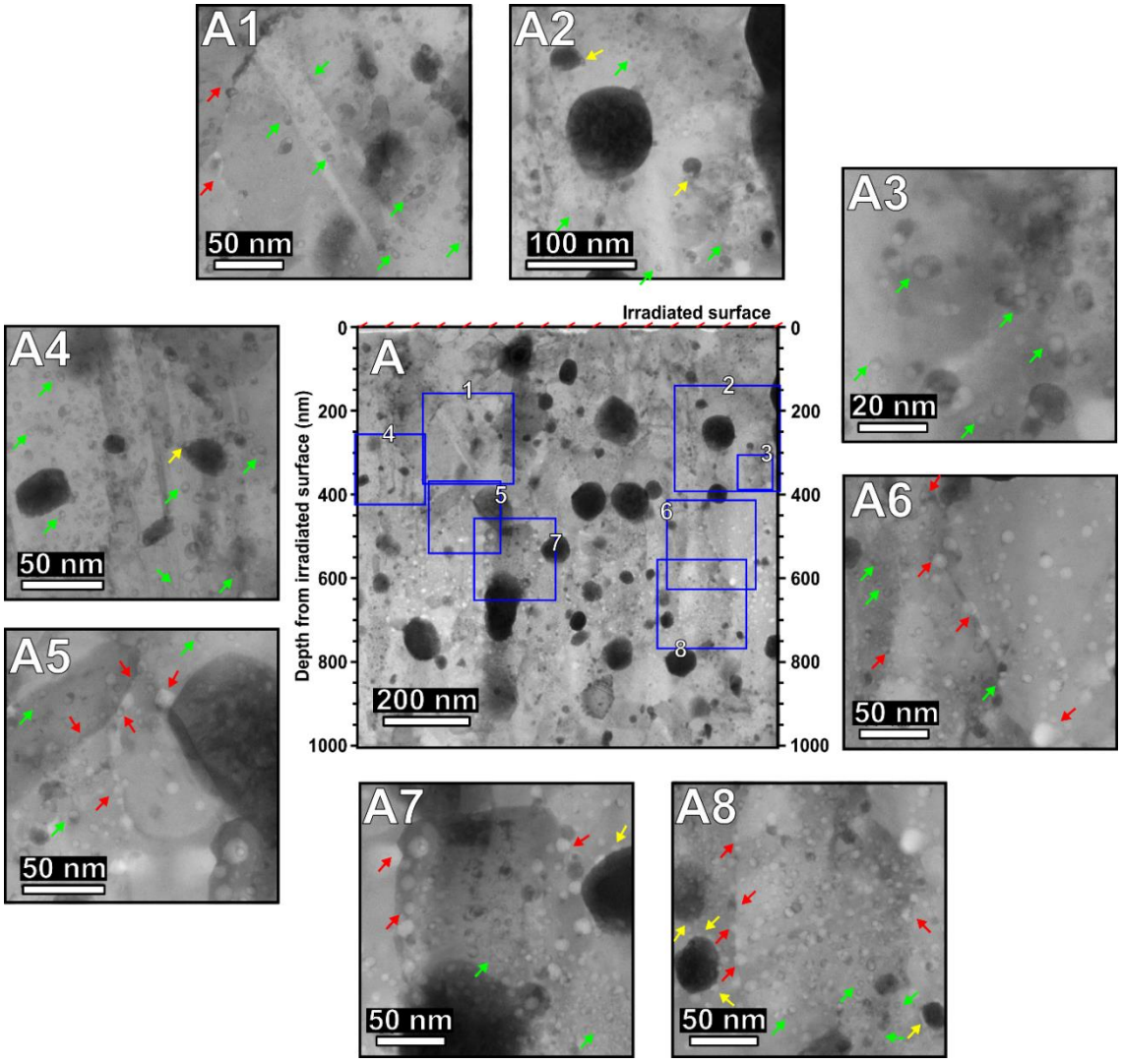

Figure 21: Helium bubble distribution at 723 K. (A) Low magnification BF STEM image showing the complete damage region from the irradiated surface. A1-A8 are high

magnification images at various irradiation depths in image A. Arrows point to bubbles at various interfaces such as Red- Grain boundaries, Yellow-Large Ta interfaces and Green-Ta nanoclusters.

5.3.2 Swelling and Microstructural stability at 723 K

Figure 22 shows helium bubble statistics for the 723 K implantation. At 723 K and dose levels of 1 dpa and 0.5 at.% He, the swelling is as low as 0.05%. As the dose and helium concentration increased, the swelling % increased to an average peak swelling of ~0.7% at the peak damage region (2.5 dpa and 4 at.% He). This swelling% is comparable/slightly lesser than that observed in candidate NFA 14YWT and Cu-V nanolayers at a similar dose and helium levels (Q. Li et al. 2014; Fu et al. 2010). The bubble density measured at ~400 nm from irradiated depth was around $1.2x10^{23}/m^3$ similar to the nanocluster density which is in the order of $\sim 6.6x10^{23}/m^3$ further agreeing with the TEM observation where most of the bubbles were associated with Ta nanoclusters <400 nm. Furthermore, to a He concentration and dose of 3 at.% and 2.5 dpa respectively at 723 K, the nanocrystalline grain size is maintained at an average of ~85 nm from 50 nm in the as-received state, indicating the stability of the clusters and its effectiveness in pinning the grain boundaries at such high helium levels.

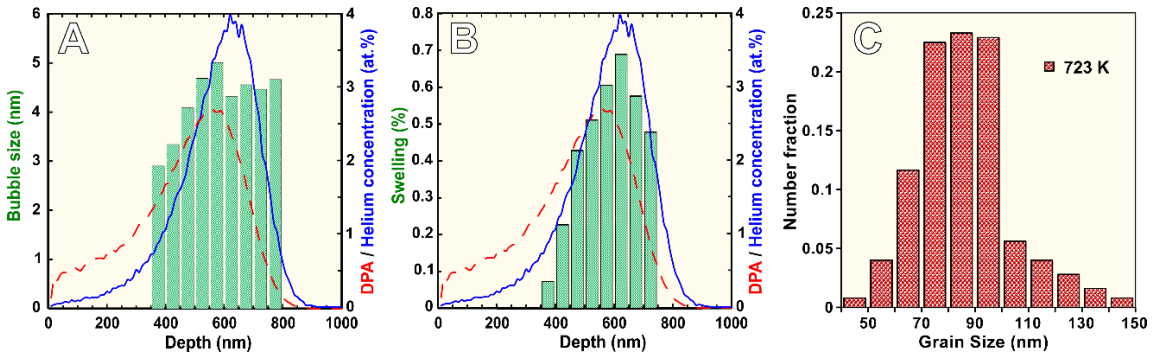

Figure 22: Helium bubble and grain statistics at 723 K. (A) Bubble size distribution as a function of irradiation depth (dose) (B) Calculated swelling % along the irradiation depth (C) Grain size distribution of the sample irradiated at 723 K obtained from the depth span of 100-600 nm from the irradiated surface.

5.3.3 Helium partitioning to nanoclusters

Atom probe analysis was carried out to further analyze the efficiency of these Ta clusters in trapping helium by mapping the locations of helium atoms with respect to tantalum clusters and the copper matrix. **Figure 23** B and C show the slice taken from the APT tip of room temperature irradiated sample in **Figure 23**A, ~225 nm from the irradiated surface. The 2D contour density maps for Cu, He and Ta show the presence of high-density regions of helium which are coinciding with that of tantalum indicating the preferential partitioning of helium to the nanoclusters. The iso-concentration surface generated for tantalum and helium (**Figure 24**) also indicated a vast majority of helium going into tantalum.

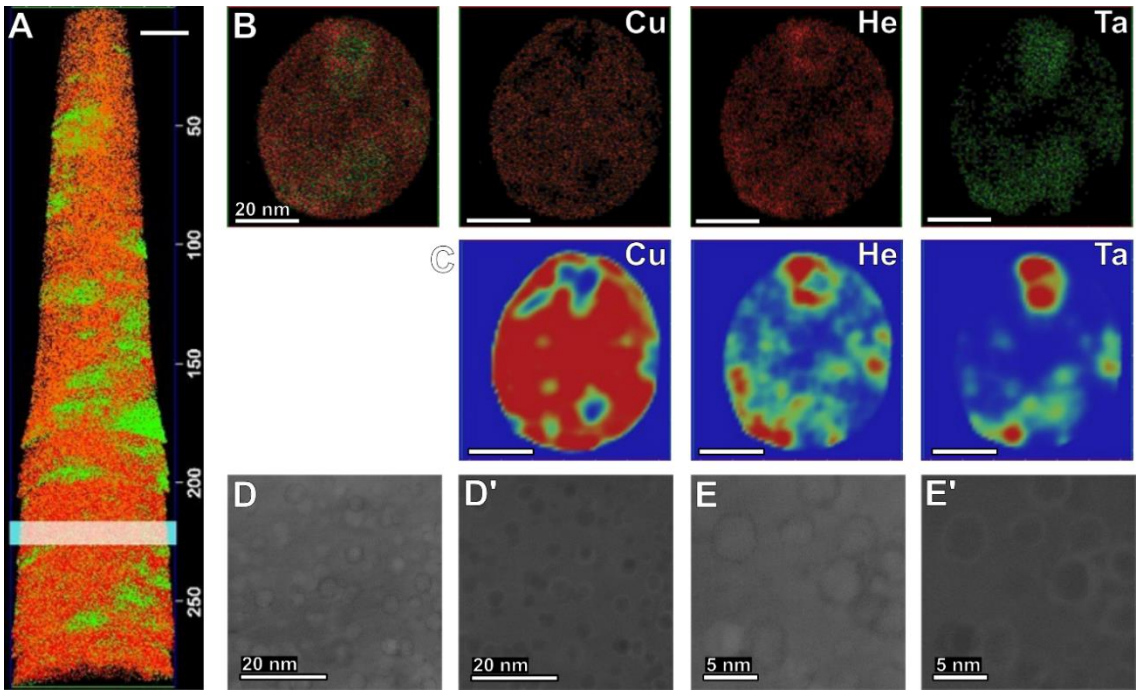

Figure 23: Helium partitioning in Ta clusters. (A) Atom distribution map of an APT specimen prepared from the irradiated surface (to a depth of ~300 nm) for the room temperature irradiation, where Cu is shown in orange and Ta in green (B) A slice taken from the highlighted region in APT needle in A showing the distribution of Cu, He and Ta atoms in that slice (C) 2-D contour density map of the atom distribution in B (D-E) High resolution BF STEM images and the corresponding HAADF images (D'-E') for 723 K irradiation showing the presence of lighter Helium at the core of the nanoclusters similar to the atom probe data.

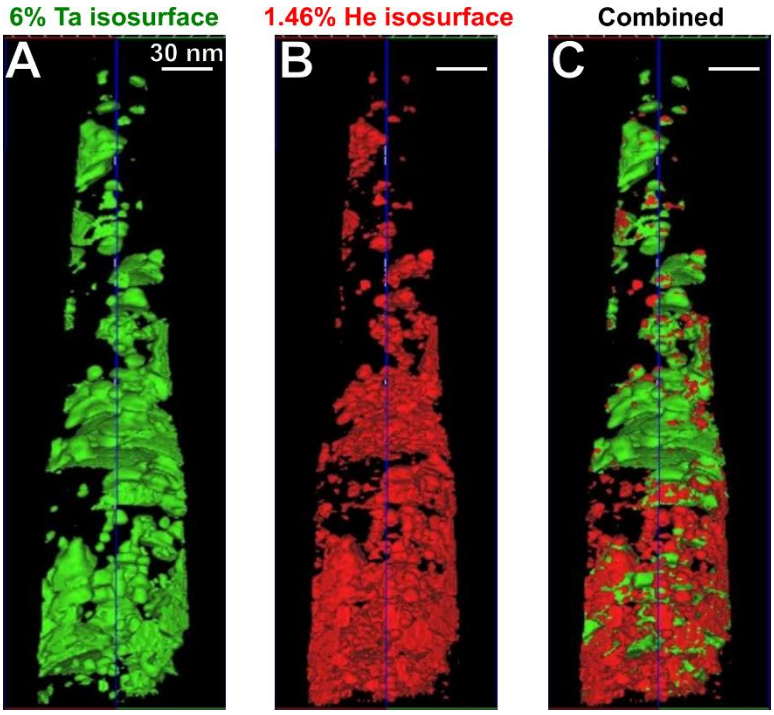

Figure 24: Iso-concentration surfaces of Tantalum (6%) and helium (1.46%) generated for the tip irradiated at room temperature. (Surface values were taken from the compositional data generated by the He proxigram)

To put in perspective, the helium concentration in copper matrix and in tantalum precipitates were calculated using proxigrams from atom probe data to be ~0.23 and 1.46 at.% helium respectively (**Table 2**). This high affinity of tantalum to helium reduces the amount of helium available freely to bind with vacancies and form large helium bubbles at the matrix and grain boundaries. Such high binding of helium to tantalum was observed W-5Ta where the binding energy further increased the addition of more helium atoms to tantalum (Ipatova et al. 2021). Additionally, the radial distribution function of various elements (**Figure 25**) with respect to tantalum also shows the increased affinity of helium towards tantalum further pointing that the Ta nanoclusters are the preferential sites for helium segregation and bubble nucleation in Cu-Ta.

Table 2. Matrix and precipitate compositions generated from helium proxigram

Ta Precipitate Compositions			Cu Matrix Composition	
Cu	86.23		**Cu**	96.20
Ta	6.00		**Ta**	1.24
He	1.46		**He**	0.23
O	3.59		**O**	0.58
N	0.66		**N**	0.17
C	0.02		**C**	0.01
Fe	0.10		**Fe**	0.02
H	1.92		**H**	1.53

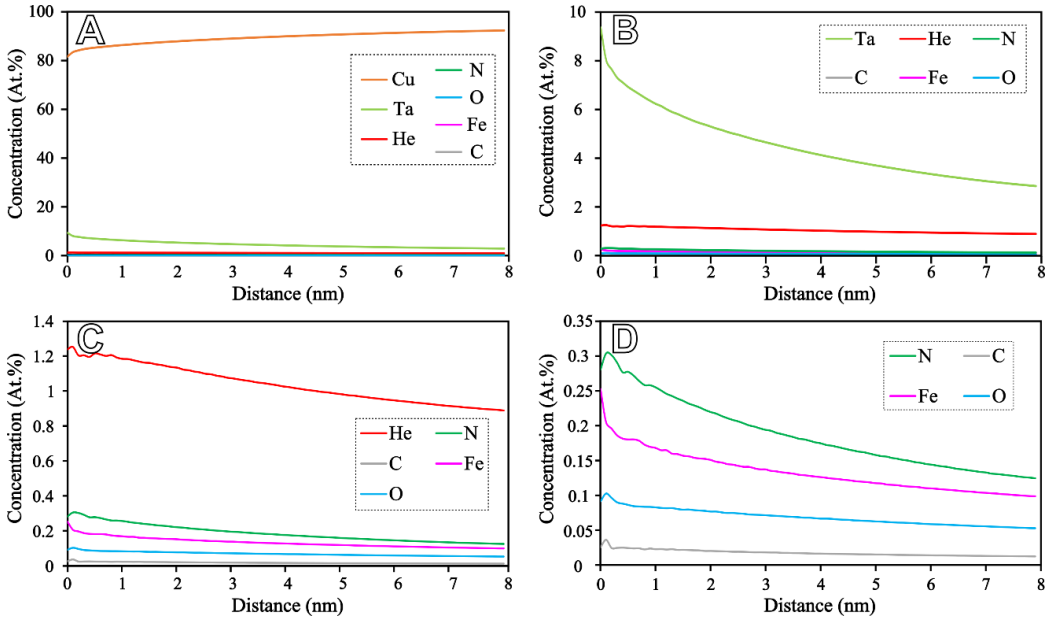

Figure 25: Radial distribution of concentration with respect to tantalum in Cu-10at.%Ta irradiated at RT

Immiscible semi-coherent heterophase boundaries have been considered effective sinks for radiation induced defects due to their high density of misfit dislocation interfaces

(MDIs). Based on O-lattice theory prediction, the lattice parameter ratio of Ta and Cu (0.91) indicates a high density of areal MDIs at their fcc/bcc interface which are efficient sinks for radiation induced defects, much similar to Cu-Nb interfaces (S.-H. Li, Li, and Han 2019). The effectiveness of these MDI's in absorbing defects is evident from the observed high critical helium concentration/interface of ~7.8-9.9 atoms/nm^2 in Cu/Ta compared to other interfaces like Cu-V or Cu-Mo (S.-H. Li, Li, and Han 2019). Likewise, high resolution TEM images of the nanoclusters from 723 K irradiation in **Figure 23** (D-E) also show low-density core structure within the shell of tantalum nanoclusters indicating helium accumulation and bubble nucleation within the tantalum nanoclusters whose growth is typically limited by the size of the clusters. Earlier works on the chemistry of the nanoclusters indicated that the nanoclusters exhibit a core-shelled structure with the core rich in oxygen and vacancies embedded in tantalum shell (Hornbuckle et al. 2015). Such vacancy trapping mechanisms have been reported in oversized solutes and have been proposed as an effective mechanism to suppress void swelling (Smidt and Sprague 1973). Thus, in addition to the misfit dislocations in the semi-coherent interfaces of these nanoclusters, the defected cores provide additional free volume for effective helium trapping and serve as preferred nucleation sites for helium bubbles in Cu-10at.%Ta as seen in **Figure 23** (D-E).

5.4 Conclusions

In summary, helium irradiation was carried out on NC Cu-10at.%Ta to a peak helium concentration of 4 at.% He at room temperature and 723 K to understand the sink efficiency of Ta nanoclusters and bulk swelling behavior of the alloy. The TEM analysis of cavity

distribution shows a large density of bubbles associated with the nanoclusters and swelling of 0.8% at peak damage region at 723 K. This is further confirmed through APT data which indicates high affinity of helium to tantalum leading to preferential nucleation of helium bubbles tantalum nanoclusters in Cu-10at.%Ta. In addition to the nanocluster interfaces, the defected cores also seem to provide additional free volume for helium trapping. This is confirmed from low peak swelling observed at 723 K indicating the efficiency of these nanoclusters in suppressing swelling by acting as effective trapping sites for helium atoms sequestrating helium bubbles.

CHAPTER 6

6 EFFECT OF TA CONCENTRATION ON THE HIGH DOSE SELF-ION IRRADIATION BEHAVIOR OF CU-TA ALLOY

6.1 Introduction

Designing and developing materials that can withstand harsh nuclear environments is of great importance to ensure the safe and efficient performance of reactors (G.S. Was et al. 2019). Nanocrystalline materials are known to be a promising candidate for radiation tolerant structures owing to their high density of interfaces that can neutralize radiation induced defects (Wurster and Pippan 2009; Chang et al. 2013). However, their microstructural instability to stimuli such as temperature, stress, and intense radiation render their potential to not be completely utilized (Jin, Cao, and Short 2019). Through years of computational research and eventual experimental efforts, grain boundary stabilization has become viable through solute addition that either lower the grain boundary energy (thermodynamic stabilization) or form atomic clusters that pin the grain boundary restraining the grain boundary mobility (kinetic stabilization) (Carl C. Koch et al. 2013; C. C. Koch et al. 2008). Such kinetically stabilized systems such as immiscible metal alloys introduce numerous types of sharp and diffused interfaces between the phases in addition to grain boundaries, due to their phase separating nature (Koju et al. 2016).

In such materials with high sink density, irradiation induced point defects primarily interact with and potentially accumulates at the interfaces (grain boundaries and heterophase boundaries). Such defect accumulation can affect the structural stability of

interfaces causing grain growth (Kaoumi, Motta, and Birtcher 2008), coarsening, dissolution, or disordering of second phase particles (Wharry, Swenson, and Yano 2017), depending on nature and sink efficiency of the interface (W. Z. Han et al. 2012). As mentioned before, since the concern with grain growth in nanocrystalline materials can be addressed by appropriate solute additions that segregate to and pin the grain boundary, the overall behavior of such system depends on the behavior and stability of the second phase particles. Mechanisms of phase stability (eg., ballistic dissolution, Ostwald ripening, inverse Ostwald ripening, etc.) in systems driven far from equilibrium either through processing or through high energy irradiation have been vastly discussed theoretically and experimentally in various alloys (Russell, n.d.; 1993; Nelson, Hudson, and Mazey 1972; Wilkes 1979).

Recent work on nanocrystalline Cu-10at.%Ta discussed in Chapter 4 has shown exceptional microstructural stability and self-healing of radiation damage through re-precipitation of Ta clusters (Srinivasan et al. 2020). Though the response of second phase particles and their role in stabilizing and increasing the sink density have been shown in the previous study, the effect of solute concentration has not been studied to understand the role of different types of precipitates and to the prospect of optimizing the composition for improved radiation resistance. Thus in this work, we study and compare the high dose self-ion irradiation response of Cu-3at.%Ta and Cu-10at.%Ta to understand the role of tantalum concentration (precipitates) in the radiation response.

6.2 Methodology

6.2.1 Irradiation experiments and SRIM analysis

NC Cu-3Ta and Cu-10Ta cylindrical specimens with 3 mm diameter and ~1.2 mm tall, were mechanically polished to a mirror finish and irradiated with defocused 4 MeV $^{63}Cu^{++}$ ions as described in section 4.2.2. A flux of ~9 x 10^{12} ions cm^{-2} s^{-1} was used to achieve fluences of 2-2.2 x 10^{17} at room temperature (RT) and 573 K. Damage profiles in displacements per atom (dpa, **Figure 26**:), indicate a damage level of 100 dpa near the surface (relatively flat), with peak damage of ~300 dpa occurring at ~1 µm.

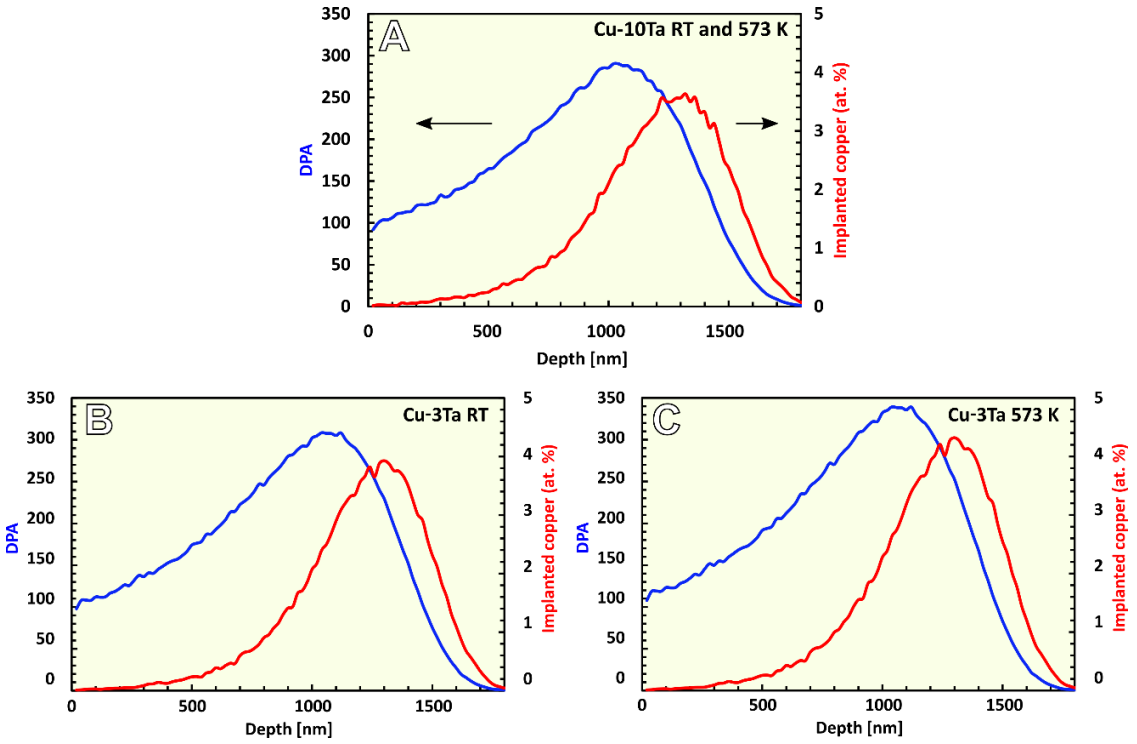

Figure 26: SRIM Damage profile. Dpa profile and range for NC Cu-10Ta and Cu-3Ta alloys irradiated with 4 MeV Cu^{++} ions at room temperature and 573 K.

6.2.2 Microstructural and Atom Probe characterization

For transmission electron microscopy (TEM) characterizations carried out in ARM-200F, samples were prepared using a Focused Ion beam (FIB) FEI Nova 500 to get cross-section liftouts of the top irradiated region of interest which were thinned to electron transparency till 2 keV and were plasma cleaned in Ar prior to TEM observations to reduce contamination. Grain size statistics were obtained from depths spanning 100-600 nm from the irradiated surface using ImageJ software.

6.3 Results and Discussion

6.3.1 Composition optimization: As-received microstructure comparison

Initially, the composition of Cu-Ta alloys was optimized to reduce the concentration of large tantalum precipitates without compromising much on nanocluster density and grain size. Through microstructural analysis of various processed alloy compositions (**Figure 27**), NC Cu-3Ta was identified to be the optimum composition for the above-mentioned criteria.

As received microstructure of Cu-10Ta and Cu-3Ta shown in **Figure 27 (A and C)** depicts the key differences in their microstructure. Cu-10Ta exhibits a nanocrystalline copper grain size in the order of 50 nm while Cu-3Ta has a slightly larger grain size of 99 nm. With respect to the tantalum phase, Cu-10Ta has a bimodal size distribution with the presence of large incoherent Ta precipitates (~30 nm in average) and smaller nanoclusters (~3 nm in average). On the other hand, Cu-3Ta possesses majorly just the nanoclusters

with a very limited concentration of large precipitates. Previous atom-probe studies have also indicated a nanocluster density of 6.5 x 10^{23} /m^3 and 5.4 x 10^{23} /m^3 (18% lesser) in Cu-10Ta and Cu-3Ta respectively post ECAE processing at 700 C. However, the effect of large Ta precipitates in the micrometer regime cannot be precisely included in the cluster density calculation due to the small sampling size in an atom probe tip. This could mean a slightly lower effective cluster density in the bulk compared to the reported atom probe values. Due to the near absence of such large precipitates in Cu-3Ta and those regions being replaced by nanoclusters, the relative number density of nanoclusters in Cu-3Ta in comparison to Cu-10Ta should be effectively higher than the atom probe comparison. This in addition to the absence of incoherent interfaces could result in a potentially better sink concentration and efficiency in Cu-3Ta.

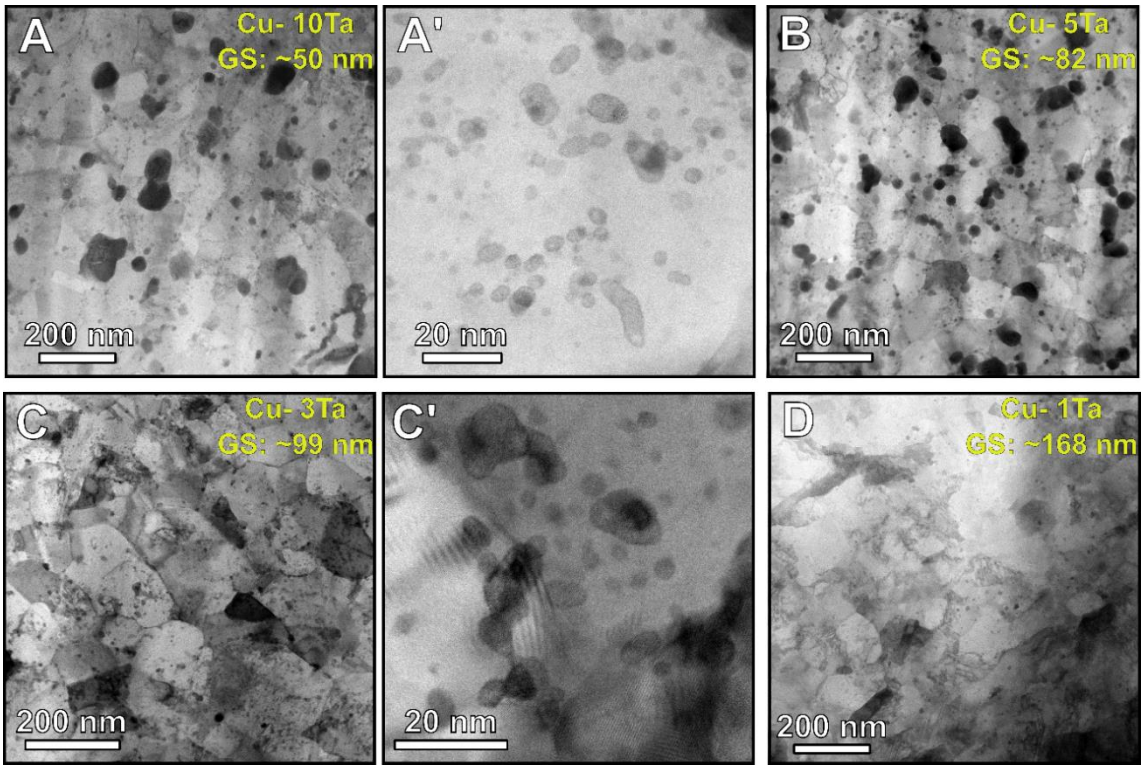

Figure 27: As-received microstructure. STEM images of (A-A') Cu-10at. %Ta, (B) Cu-5at. %Ta (C-C') Cu-3at. %Ta (D) Cu-1at. %Ta depicting the difference in grain size and density of large and small tantalum precipitates

6.3.2 Microstructure post room temperature implantation

Post irradiation to a dose of 100 dpa at room temperature, the grain size in Cu-10Ta increased from 50 nm to 110 nm and Cu-3Ta though had a higher initial grain size of 99 nm, exhibited a small grain growth to an average of ~160 nm still maintaining a nanocrystalline microstructure (see **Figure 28**A-A'). Looking at the tantalum phase stability, the high dose-rate in heavy ion and the low irradiation temperature resulted in disordering of the large incoherent tantalum precipitate interfaces in Cu-10Ta (**Figure 28**B'). However, in Cu-3Ta, owing to the limited density of large Ta precipitates, no such amorphization was observed (**Figure 28**B). The limited density of large precipitates and more clusters replacing them, act as efficient defect sinks thereby preventing/ increasing the threshold of such defect accumulation and amorphization in the fewer large tantalum precipitates available in Cu-3Ta.

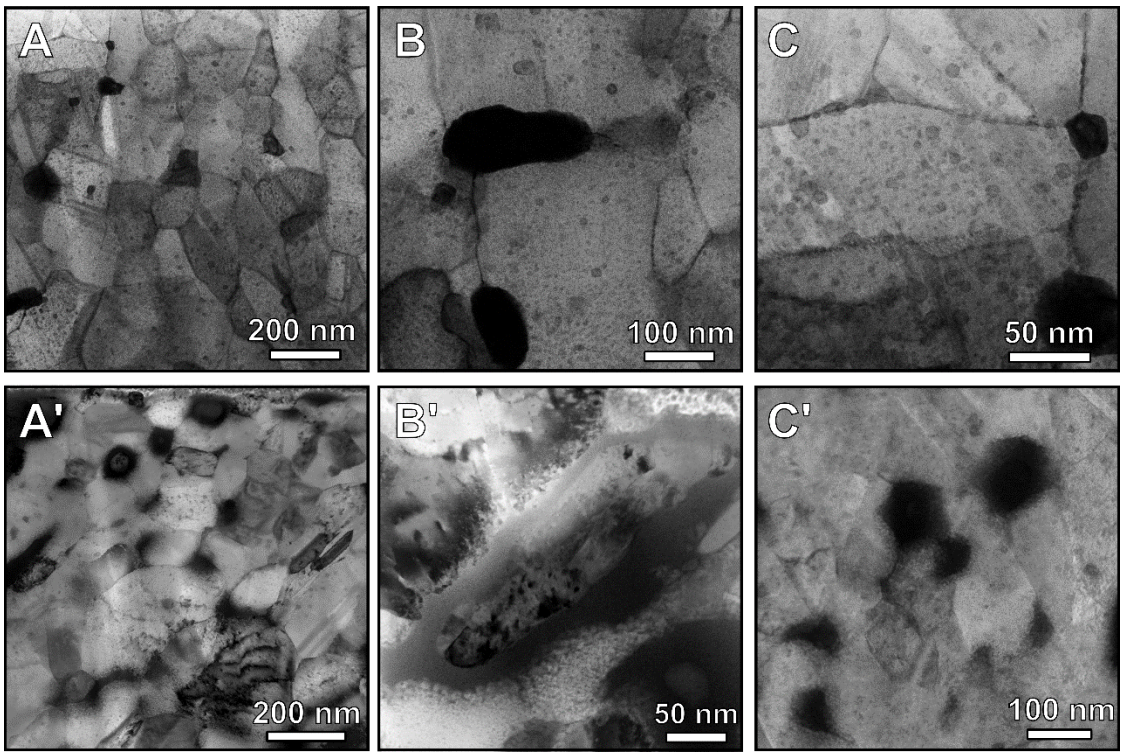

Figure 28: Post irradiation microstructure at RT of Cu-3at.%Ta and Cu-10at.%Ta. BF STEM microstructure of (A-C) NC Cu3Ta alloy (A'-C') Cu-10Ta post-irradiation to 100 dpa at RT highlighting the microstructure and phase stability

As a result, the large precipitates in Cu-10Ta underwent disordering dissolution as seen from tantalum short-circuit diffusion observed in a few grain boundaries. In addition, significant reduction in Ta cluster density was evidently observed in many grains indicating dissolution of the nanoclusters **Figure 28**C'. In Cu-3Ta few large tantalum precipitates showed similar pipe-diffusion along the grain boundaries as observed in Cu-10Ta, while most of the grain boundaries were still decorated with nanoclusters (**Figure 28**C). Interestingly, TEM images also indicated lesser Ta cluster dissolution i.e., higher density of Ta clusters observed in Cu-3Ta compared to Cu-10Ta after irradiation to 100 dpa at room temperature as seen in **Figure 29**.

Additionally, sporadic void formation was also observed in both these alloys after some incubation time (**Figure 29** B-C'). In Cu-10Ta, voids of an average size of ~12 nm were mainly observed to be formed along the large tantalum interfaces which showed initial transient disordering, followed by dissolution. The maximum swelling observed was ~0.25%. On the other hand, in Cu-3Ta, the voids were smaller in the order of ~ 7nm in average and comparatively lesser in density than Cu-10Ta. The voids in Cu-3Ta were mostly confined to the grain boundaries with a maximum swelling of 0.07%.

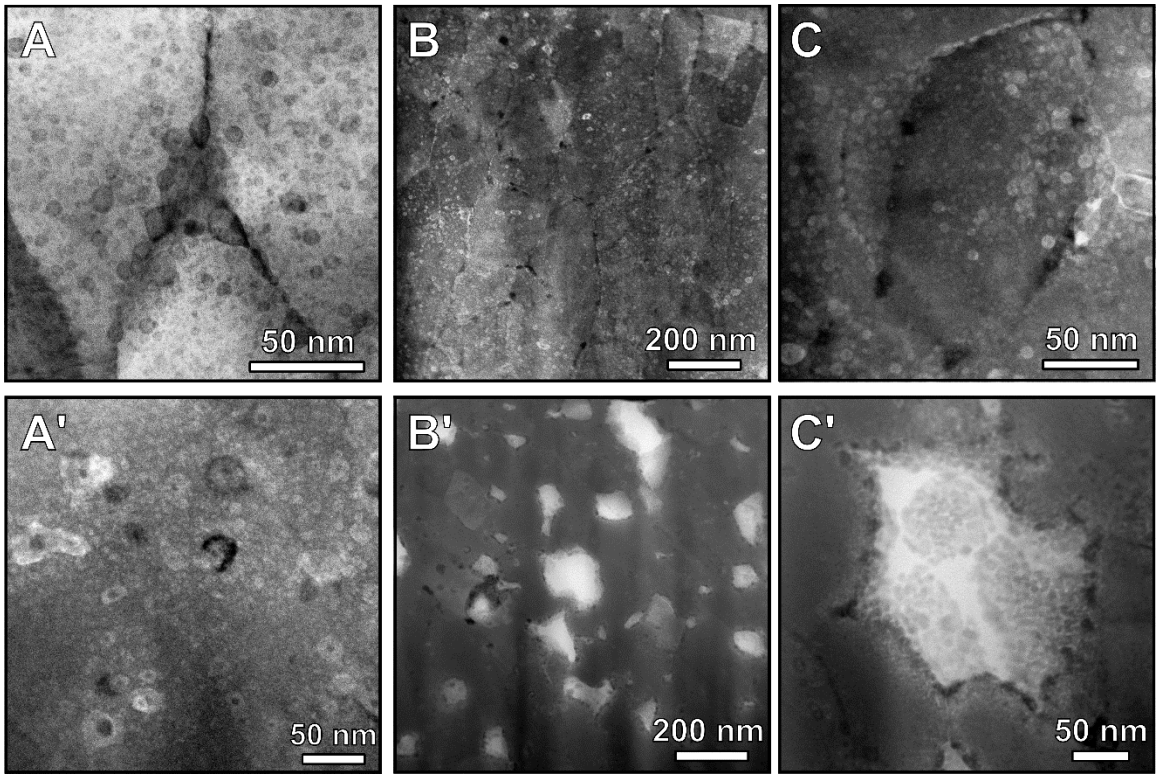

Figure 29: Post irradiation microstructure at RT of Cu-3at.%Ta and Cu-10at.%Ta. BF STEM microstructure of (A-C) NC Cu3Ta alloy (A'-C') Cu-10Ta post-irradiation to 100 dpa at RT highlighting the nanocluster stability and void formation

6.3.3 Microstructure post 573 K implantation

At 573 K, no voids were observed in both Cu-10Ta and Cu-3Ta, with no amorphization in Cu-10Ta as well. Cu-10Ta also showed a significant increase in cluster density due to thermally enabled nanocluster re-precipitation from the dissolved large and small precipitates. Similar short circuit diffusion of large Ta precipitates and cluster precipitation were observed in Cu-3Ta as well indicating the presence of microstructure rejuvenation mechanism in both the alloys (see **Figure 30)**.

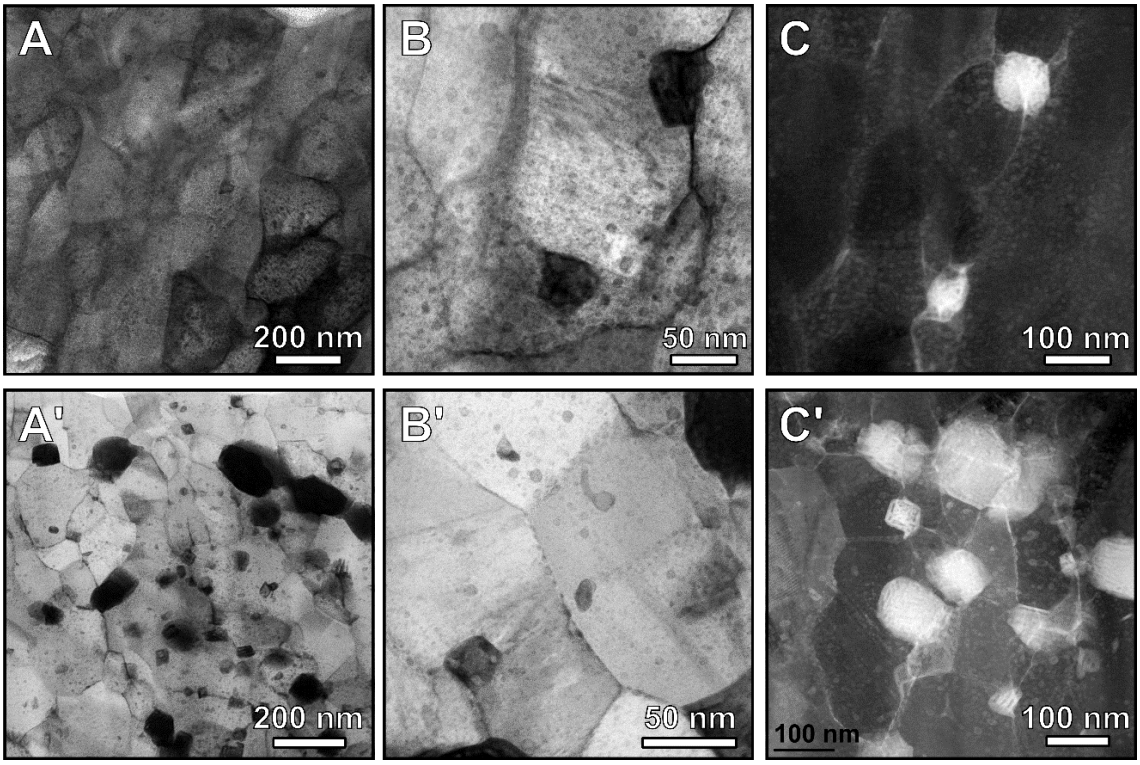

Figure 30: Post irradiation microstructure at 300 °C of Cu-3at.%Ta and Cu-10at.%Ta. Microstructure irradiated to 100 dpa at 300 C of (A-C) NC Cu-3Ta alloy showing stable grains and nanoclusters and voids along some grain boundaries (A'-C') Cu-10Ta.

Though Cu-10Ta microstructure is able to self-heal with more nanoclusters at 300 C, the TEM microstructure shows an evident reduction in cluster density indicating significant cluster dissolution at room temperature irradiation. While Cu-3Ta shows nearly unaffected cluster density even irradiating to 100 dpa at room temperature and is able to retain its nanocrystalline microstructure. Likewise, Hornbuckle et al have shown better long term thermal stability of the microstructure of Cu-3Ta compared to Cu-10Ta (Hornbuckle, Solanki, and Darling 2021). Previous studies on Cu-10Ta have characterized the coherency and misfit strain of the precipitates with respect to temperature, which indicated the presence of coherent, semi-coherent and incoherent precipitates ($d < 3.898$ nm, 3.898 to 15.592 nm, and >15.592 nm, respectively) (Rajagopalan et al. 2017). The incoherent interfaces were observed to be the preferential sites for atomic mixing and disordering in Cu-10Ta. Various previous works have observed a significant effect of ballistic interface mixing in incoherent interfaces compared to their coherent and semi-coherent counterpart (Motta and Lemaignan 1992b; Lescoat et al. 2011). On the other hand, in Cu-3Ta, only 1% of the total precipitates were incoherent, while the rest all were coherent/semi-coherent. These semi-coherent and coherent interfaces have been largely believed to be efficient defect sinks due to large density of misfit dislocations (S.-H. Li, Li, and Han 2019).

Overall, limited density of large precipitates and more clusters replacing them, improve the sink efficiency and density, thereby suppressing such defect accumulation in the large tantalum precipitates and grain boundaries, while maintaining the nanocrystalline grains in Cu-3Ta. Further experiments need to be carried out to compare other aspects of radiation

tolerance such as bubble evolution and swelling to validate the enhanced performance of Cu-3Ta.

6.4 Conclusions

The phase stability and its effect on radiation tolerance of two different compositions of Cu-Ta system (3 at.% Ta and 10 at.% Ta) are studied using high dose heavy ion irradiation at Rt and 573 K. The results indicate that Cu-3Ta shows more promise to high dose radiation and better resistance to radiation induced atomic mixing than Cu-10Ta owing to the near absence of the incoherent large Ta precipitates. Furthermore, the void swelling observed was lesser than that of Cu-10Ta indicating the presence of potentially higher semi-coherent cluster density which needs to be confirmed comprehensively with additional experiments.

CHAPTER 7

7 IN-SITU TEM CAVITY EVOLUTION WITH ANNEALING POST HELIUM AND DUAL ION IRRADIATION IN CU-10TA AND CU-3TA

7.1 Introduction

Damage evolution under an intense radiation environment can be explained using a binary collision approximation that constitutes two phases (lasting <ps), namely the first ballistic collision phase that creates the disorder in the lattice and the thermal spike phase where the excess kinetic energy is dissipated and the microstructure restores partially, leaving behind the final disrupted state of the lattice (Stoller 2012). In other words, during these stages, >70% of the radiation induced point defects to annihilate instantaneously while the remaining small portion of the defects constitutes the freely migrating vacancies and interstitials. These defects evolve within the microstructure by either agglomerating, annihilating or migrating to the sinks depending on the material microstructure, properties (migration energy, solute binding energy) and irradiation conditions (Ion type, energy, dose and irradiation temperature). Agglomeration of defects is highly unfavorable since it can lead to the formation of defect clusters such as bubbles, SFTs etc that can hinder dislocation plasticity causing hardening or further evolve into cavities causing swelling and grain boundary embrittlement that degrade the material performance (Stiegler and Mansur 1979). While research efforts focus on designing materials with a large fraction of interfaces to neutralize these defects (Xinghang Zhang et al. 2018), it is of utmost importance to understand the defect clustering, evolution, and interaction of these defects

with the interfaces in these advanced materials with a high density of sinks for continuous improvement of existing materials.

TEM with in-situ ion irradiation and annealing is a powerful tool to obtain valuable insights and real-time observation on the behavior of a material under various stimuli such as intense radiation and high temperatures to understand the fundamental mechanisms. Various observations of damage accumulation, defect and precipitate evolution have been achieved to understand the defect kinetics and response mechanism of the material (Kirk et al. 2009; Birtcher et al. 2005). Furthermore, nanocrystalline metals and alloys are largely studied in-situ to understand the effect of a large fraction of grain boundaries and sink concentration on the defect evolution (Muntifering et al. 2016). For instance, Sun et. al studied the interaction of different grain boundaries with defect clusters through in-situ Kr irradiation in nanocrystalline Ni (Sun et al. 2013). Likewise, in-situ helium irradiation was utilized to confirm preferential formation and evolution of bubbles at the grain boundaries in nanocrystalline and UFG W (El-Atwani et al. 2015).

NC Cu-Ta is an immiscible system that has shown great microstructural stability and promising response to various aspects of radiation, stress and temperatures. In the previous chapter, we compared the high dose heavy ion irradiation response focusing mainly on the microstructural and phase stability of Cu-10Ta with that of an optimized composition (i.e., Cu-3Ta), which showed a slightly enhanced response in Cu-3Ta. In this chapter, to extend this comparison to other avenues of irradiation damage and to elucidate the fundamental mechanisms involved in the radiation tolerance of NC Cu-Ta, in-situ helium and dual beam (helium + heavy ion) irradiation coupled with isochronal annealing was carried out.

Specifically, this study focused on evaluating the individual and synergistic effects of helium and heavy ion irradiation effects on the microstructural stability, defect evolution and its interaction with grain boundaries and tantalum precipitates in both the alloys for drawing a comparison.

7.2 Methodology

7.2.1 Sample preparation for in-situ irradiation experiments

Samples for in-situ TEM irradiation were prepared from bulk cylindrical specimens of Cu-10Ta and Cu-3Ta polished to mirror finish (see Chapter 3 for details on processing and consolidation). Focused ion beam Nova Nanolab was utilized to liftout and thin electron transparent lamellae which were eventually cleaned at 2 keV to remove amorphous damage created during the thinning process. The lamellae were mounted on the top of the post (see **Figure 31**) unlike the traditional side-mounting on the post in the copper half-moon TEM grids to avoid shadowing effects during the in-situ irradiation experiments.

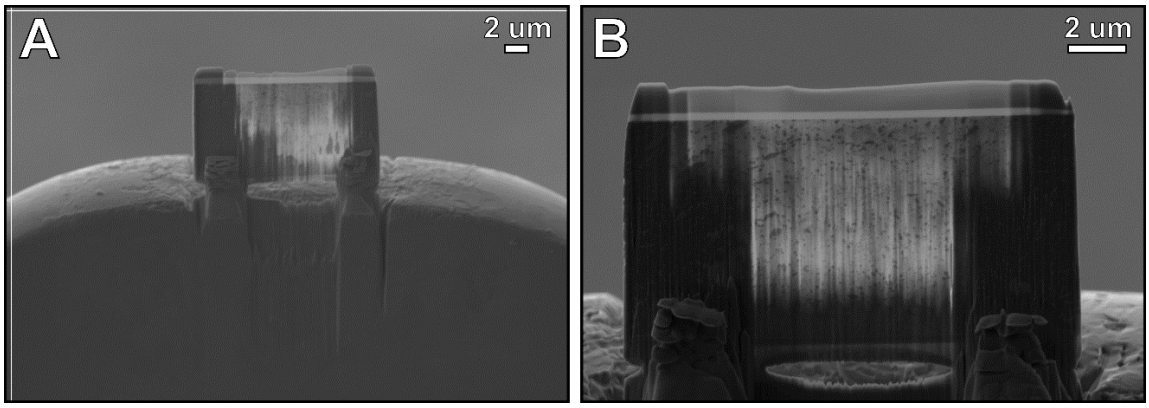

Figure 31: (A-B) TEM lamella of Cu-10Ta welded to the top of the post in TEM grid as preferred for in-situ irradiation.

7.2.2 In-situ irradiation experiments

In-situ irradiation was carried out in I^3TEM facility in the Department of Radiation Solid Interactions at Sandia National Laboratories. Jeol JEM 2100 TEM equipped with ion accelerators normal to the electron beam column. During irradiation, the sample was tilted 30 degrees from the electron beam column so that the electron and ion beam made 30 and 60 degrees with the sample normal respectively. The first set of films (Cu-3Ta and Cu-10Ta) were irradiated with 10 keV helium ions to a fluence of $5x10^{17}$ ions cm^{-2}. Next, concurrent He^+ and Au^{4+} ion irradiation was carried out on another two lamellae (Cu-3Ta and Cu-10Ta) with 10 keV He^+ and 2.8 MeV Au^{4+} ions to a fluence of $5x10^{17}$ ions cm^{-2} and $5x10^{15}$ ions cm^{-2} respectively. The irradiations were carried out at room temperature with a flux/dose rate of $1x10^{14}$ $cm^{-2}s^{-1}$ and $1x10^{12}$ $cm^{-2}s^{-1}$ respectively for He^+ and Au^{4+} ions respectively.

SRIM damage profile calculated similar to previous chapter for both these irradiation conditions (**Figure 32**) with an incidence angle of 60 degrees. Damage profiles indicate a damage of ~40 dpa and ~50 at.% He in helium irradiated samples and an additional 60 dpa more (~100 dpa) in samples irradiated with both He and Au ions as seen in the **Figure 32**. It should be remembered that the calculated dose and implanted levels are an over-estimation to actual damage due to loss of defects and gas atoms to the surface through diffusion in thin film irradiation. Hence direct quantitative comparison to ex-situ irradiation will not be meaningful.

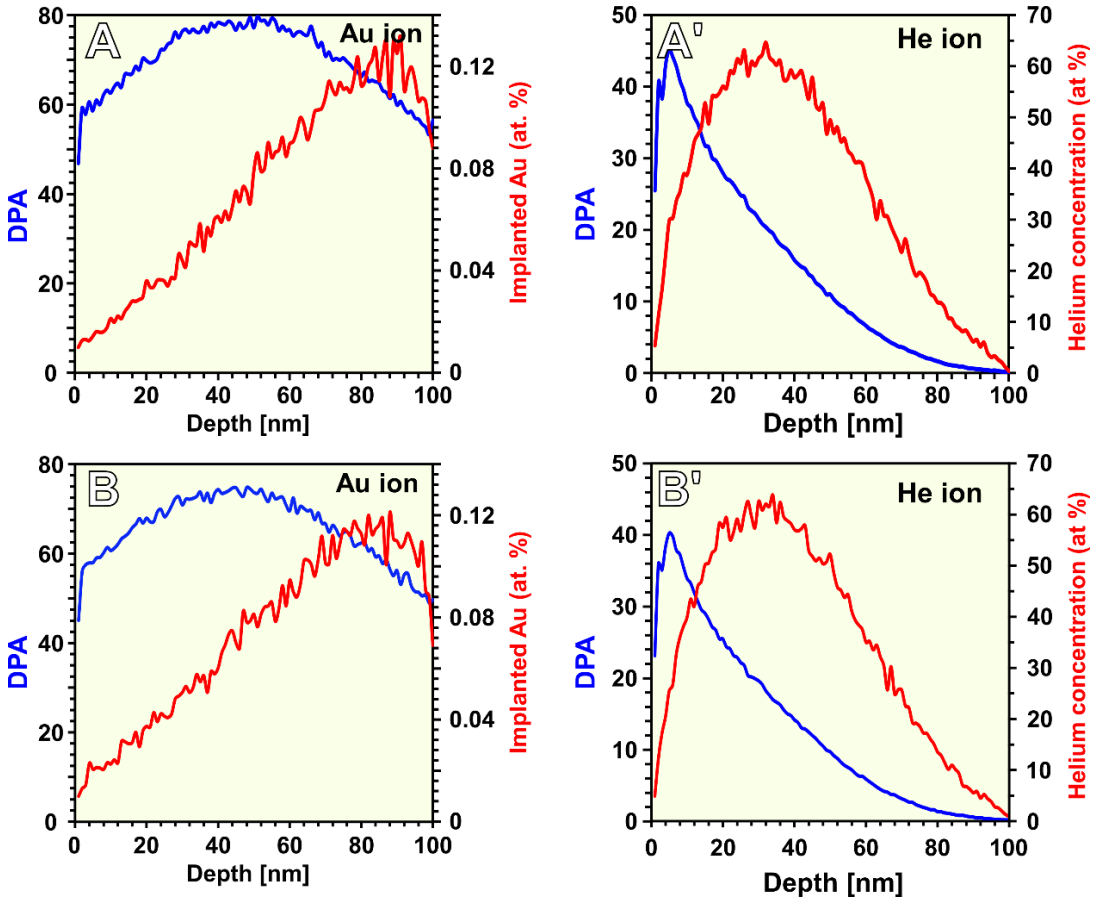

Figure 32. SRIM Dpa profile and range for (A-B) NC Cu-3Ta and (A'-B') Cu-10Ta alloys irradiated with 10 keV He^{+} and Au^{4+} ions to a fluence of $5x10^{17}$ and $5x10^{15}$ ions/cm^2 respectively.

7.2.3 In-situ annealing

Isochronal annealing was carried out inside the TEM using a Gatan heating stage at a ramp rate of 10 C/min. Annealing was carried out in steps of 50 °C from room temperature till 450 °C (~0.4 T_m) to study the evolution of bubbles systematically at each temperature. After every 50-degree ramp in temperature, the sample was held at that temperature for 10 minutes for drift stabilization before images were captured. The study could not be extended beyond 450 °C due to de-wetting induced disintegration of the TEM thin film.

Videos were recorded during both the irradiation and annealing experiments to enable a thorough analysis of the experiment.

7.2.4 Microstructural characterization

In-situ imaging and videos during irradiation and annealing were captured in BF TEM mode at 200 keV. Post-mortem ex-situ characterization of the microstructure was carried out in both BF TEM with Fresnel contrast for bubble identification and STEM mode for grain size and defect loop identification. A high defocus of ~ 1 um was adopted to image cavities where the cavity size variation is minimal. The difference in cavity diameter due to defocus should be <0.5 as estimated in (C. A. Taylor et al. 2020). Image J software was utilized to obtain grain size and bubble statistics at each annealing step.

7.3 Results and Discussion

7.3.1 Microstructural evolution during in-situ irradiation at room temperature

Time-dependent microstructural evolution with dose during in-situ helium irradiation to high helium levels of ~50 at.% helium and ~40 dpa indicated no bubble nucleation during the irradiation process. During the combined heavy-ion and helium irradiation, extensive generation of black spot damage within the matrices and at grain boundaries was observed in both the alloys, could be associated with the heavy ion strike indicating dislocation loop nucleation due to the displacement cascades in heavy ion irradiation, unlike the helium irradiation alone. No evidence of bubble nucleation was observed during the dual beam irradiation as well which had similar helium levels as the helium irradiation,

coupled with combined displacement damage of (40+60) dpa. After a week of incubation post-irradiation, the films were imaged again to look for bubbles and defects. Fresnel contrast with under focused TEM images showed the presence of tiny bubbles of ~ 1nm homogeneously distributed at the matrix and grain boundaries in all four cases as seen in **Figure 33**. This requirement of incubation time has been observed in other alloys like Zirconium alloys (C. Taylor et al. 2017), though the reasoning is not well understood as the helium is capable of migration via interstitials in copper even at 25 K (Wichert et al. 1985). Any effect of tantalum on delaying diffusion to a longer timescale needs to be looked at in the future. It was hard to detect any dislocation loops in the post-irradiation TEM and STEM images due to the overwhelming contrast from numerous nanoclusters. Hence, no correlation could be drawn between the black spot damage region and the bubble nucleation. The bubble size did not vary significantly between the two compositions (Cu-3Ta and Cu-10Ta) and the irradiation types (He and He+Au), though the bubble density in Cu-3Ta was slightly lower than that of Cu-10Ta.

Looking at the phase stability (**Figure 33**A4-D4), no disordering and dissolution of the tantalum precipitates or segregation at grain boundaries were observed in the present irradiation conditions to 70 dpa and 70 at.% He unlike the ex-situ heavy ion irradiation to doses 100-600 dpa where disordering of the large precipitates and eventual dissolution and segregation of Ta at grain boundaries was observed at room temperature [Chapter 4]. However, some of these large precipitates' interfaces were susceptible to cavity accumulation forming chains of those cavities especially in Cu-10Ta as seen in **Figure 33** (C1 and D1). Post helium irradiation there was negligible grain growth in Cu-3Ta (~99nm)

while there was a marginal grain growth from 50 nm to ~80 nm in Cu-10Ta (**Figure 33**C4). Dual beam irradiation (He+Au) led to a minimal grain growth with an average grain size of ~98 nm and ~135 nm in Cu-10Ta and Cu3Ta respectively (**Figure 33** D4 and B4) indicating extraordinary microstructural stability in both the alloys.

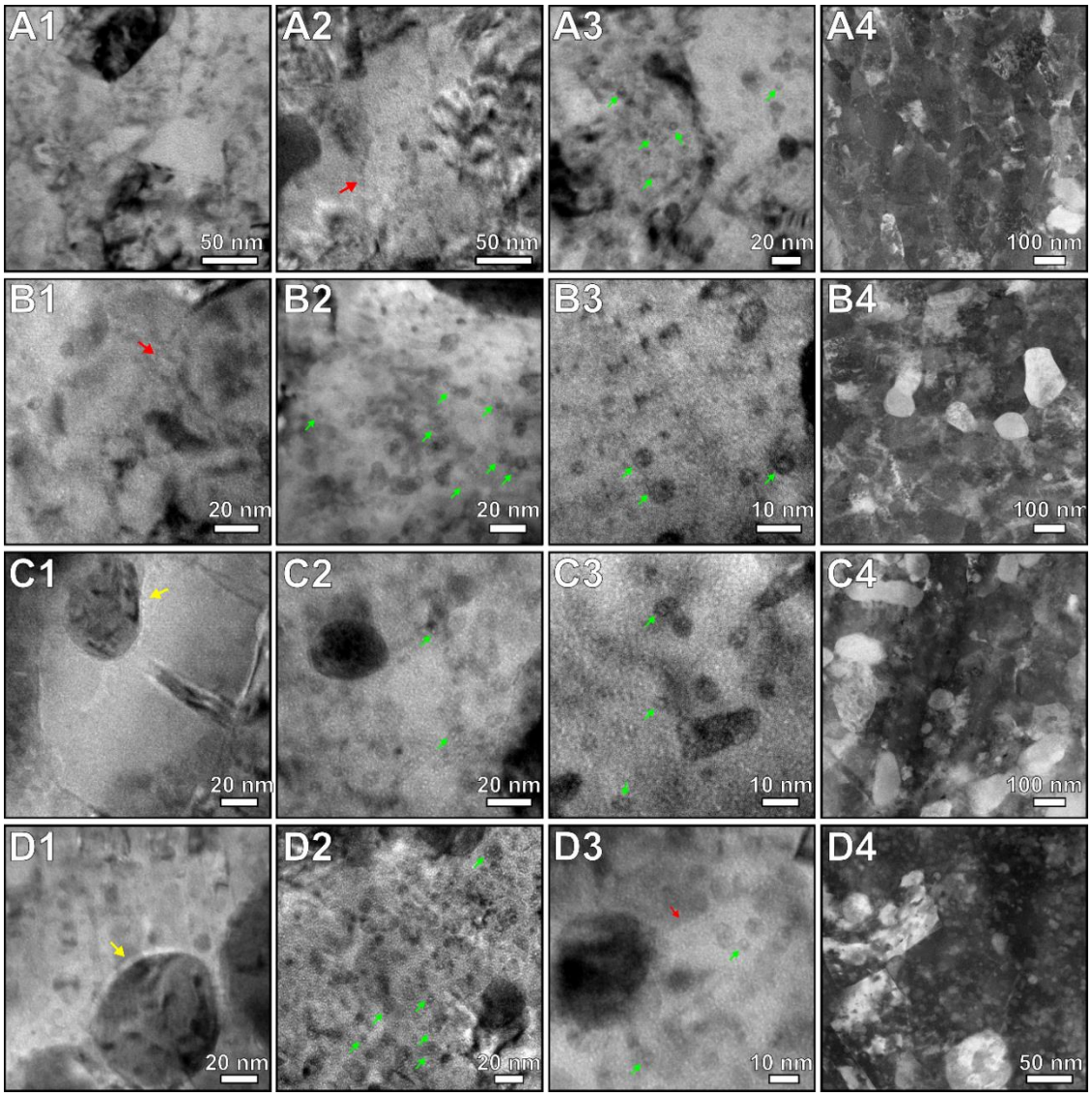

Figure 33: Post-irradiation microstructure showing the uniform areal distribution of bubbles and stable microstructure: Under focus TEM images (1-3) and HAADF STEM images (4) of Cu-3Ta irradiated with (A) He ions, (B) He+Au ions and Cu-10Ta irradiated with (C) He ions and (D) He+Au ions. Arrows point to bubbles at various locations: Red- Grain boundaries, Yellow- Large tantalum precipitates and Green- Ta nanoclusters.

7.3.2 Cavity evolution with annealing

The irradiated films were then subjected to isochronal annealing inside the TEM to gain more insights on the cavity evolution, coarsening mechanisms, and microstructural changes with temperature in both the alloys. As the annealing temperature increased more bubbles were observed to migrate to the sinks (grain boundaries and Ta interfaces). For instance, in helium implanted Cu-10Ta, as the annealing temperature increased, the homogenous bubble distribution as seen in **Figure 34**A & B till 150 C is slowly overtaken by more bubbles preferentially located at the grain boundaries as the temperature approached 400 °C and above (**Figure 34** C&D) indicating the effectiveness of the grain boundaries to act as helium bubble sinks. High sink efficiency of grain boundaries have been observed in NC Cu has been attributed to the interstitial emission mechanism operating at the grain boundaries (Bai et al. 2010). In other words, the comparatively slowly migrating vacancy cluster when approaches a grain-boundary loaded with interstitials, recombines with those interstitials which the grain boundary re-emits. Moreover, the matrix bubble density reduced from 1.9×10^{24} /m^3 at room temperature to 9×10^{23} /m^3 at 100 °C and 8.5 and 5.3×10^{23} /m^3 at 400 °C and 450 °C respectively indicating both bubble migration to sinks and coarsening of the bubbles with increasing temperature.

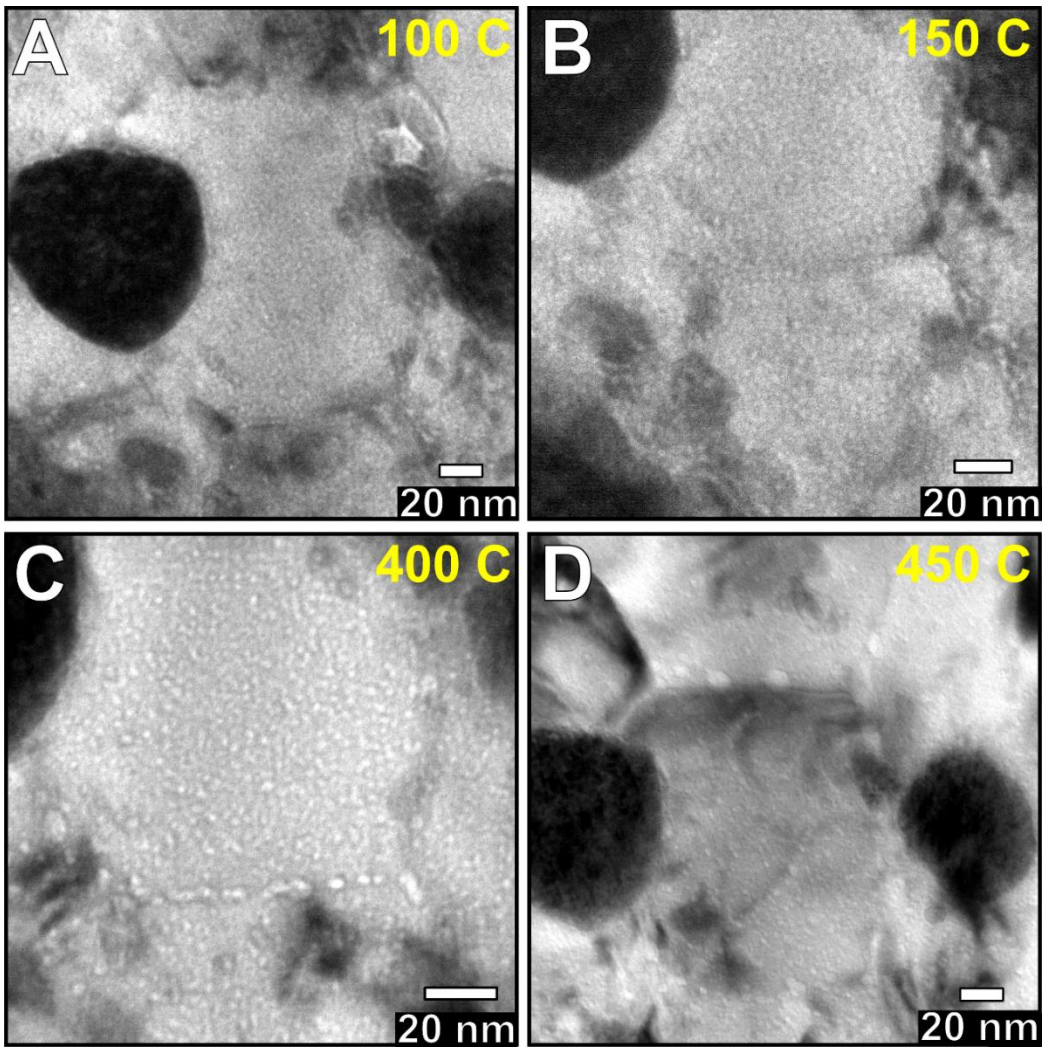

Figure 34: Bubble evolution with annealing in helium implanted Cu-10Ta

Additionally various bubble coarsening mechanisms involved in Cu-Ta alloys are explored using the videos recorded during the annealing expriments. In metals, helium bubble coarsening has been proposed and modeled to occur mainly via two mechanisms viz., the high activation energy Ostwald's ripening where the smaller bubbles undergo thermal resolution and the dissolved helium atoms get reabsorbed at larger ones (Villacampa et al. 2018) and the low activation energy migration and coalescence (MC)

mechanism which primarily occurs through random walk (or biased migration (Gruber 1967)) of the helium bubbles driven by diffusion and vapor transport mechanisms (Singh and Trinkaus 1992; Schroeder and Fichtner 1991; Goodhew 1983). Other mechanisms like cascade coalescence mechanisms have also been proposed to play a role in the formation of huge bubbles through volume expansion (Hou et al. 2010). In-situ annealing provides us with more insights and experimental evidence to support various helium bubble coarsening mechanisms in metals.

During annealing of helium implanted Cu-Ta alloys, random vibratory movement of helium bubbles was observed at grain boundary without any directional bias. For instance, **Figure 35** corresponds to the image sequence from the annealing video of helium implanted Cu-10Ta between 400-450 ° C, where one of the bubbles moves back and forth to another bubble in a random fashion. Given the not very high maximum annealing temperature (~0.4 T_m) such diffusion-driven migration is more commonly observed in grain boundaries that have higher diffusivity. This random walk is often referred to as the Brownian type motion of helium bubbles that is reported in many other materials as well like Fe and Fe-9Cr (Ono, Arakawa, and Hojou 2002), Fe-Cr-Ni (L. Wang et al. 2019), V(Tyler and Goodhew 1980), Cu (Willertz and Shewmon 1970) and Al (Ono et al. 1992; 2009) which enables migration and coalescence of helium bubbles at intermediate to moderately high temperatures.

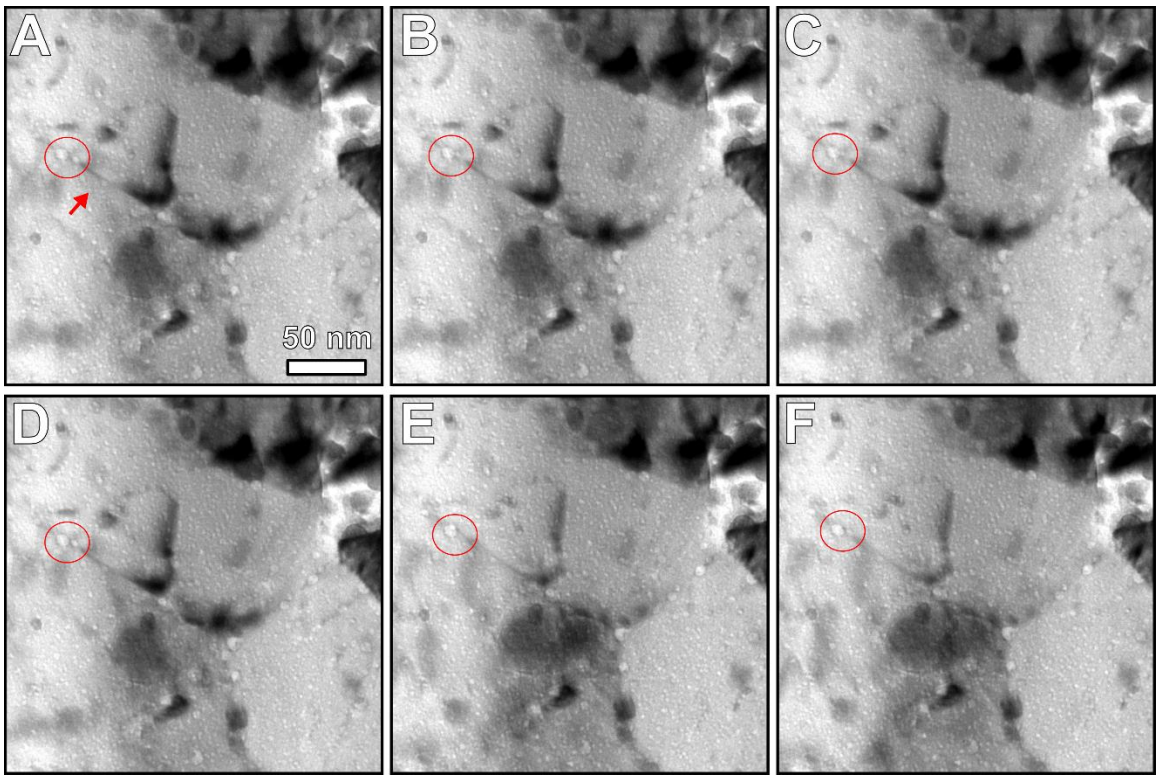

Figure 35: Image sequence of helium bubble exhibiting Brownian motion at grain boundaries captured during annealing from 400-450 °C of helium implanted Cu-10Ta

No evidence of Ostwald's ripening was observed due to its high thermal activation energy requirement which could come in the picture at much higher temperatures. Furthermore, the bubbles did not exhibit any prominent facet formation until 450 ° C (0.4 T_m). Additionally, some of the bubbles were observed to coalesce in a way that one of the bubbles extends on its side close to a nearby bubble and eventually coalesce into a single bubble as captured in the image sequence in **Figure 36**. Thus, the experimental observations in this work favor migration coalescence (MC) as a dominant bubble coarsening mechanism in Cu-Ta alloys present at these experimental conditions.

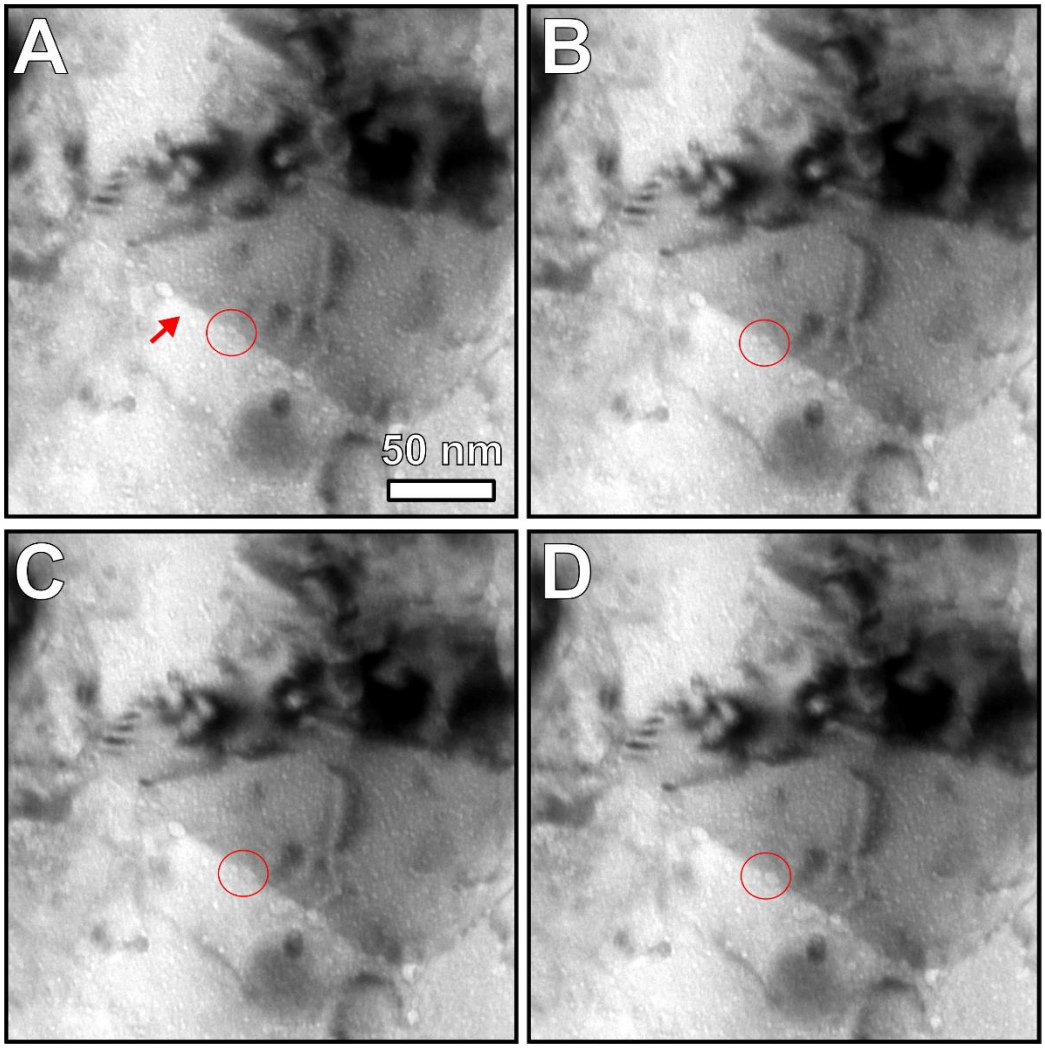

Figure 36: Image sequence of helium bubble coalescence at grain boundaries captured during annealing from 400-450 °C of helium implanted Cu-10Ta.

Now we focus on the comparison of the bubble evolution in the two alloys irradiated with He and dual beam (He+Au) (**Figure 37** and **Figure 38).** Firstly, in helium irradiated samples, post-annealing till 450 °C, Cu-10Ta possessed bubbles of average diameter ~2.3 nm and ~5 nm at matrix and grain boundaries respectively while the corresponding Cu-3Ta possessed bubbles of ~1.5 and 1.85 nm at the matrix and grain boundaries **Figure 37** A2&B2. Furthermore, the bubble density in helium implanted Cu-3Ta was much lesser

than that of Cu-10Ta. Additionally, the large tantalum interfaces in Cu-10Ta were observed to be decorated with helium bubbles which were coalescing to channels. A similar trend was observed between the two alloys to annealing post dual beam irradiation (**Figure 38)**, were slightly smaller bubbles at both matrix and grain boundaries in Cu-3Ta indicating the enhanced effectiveness of Cu-3Ta in reducing bubble growth compared to Cu-10Ta.

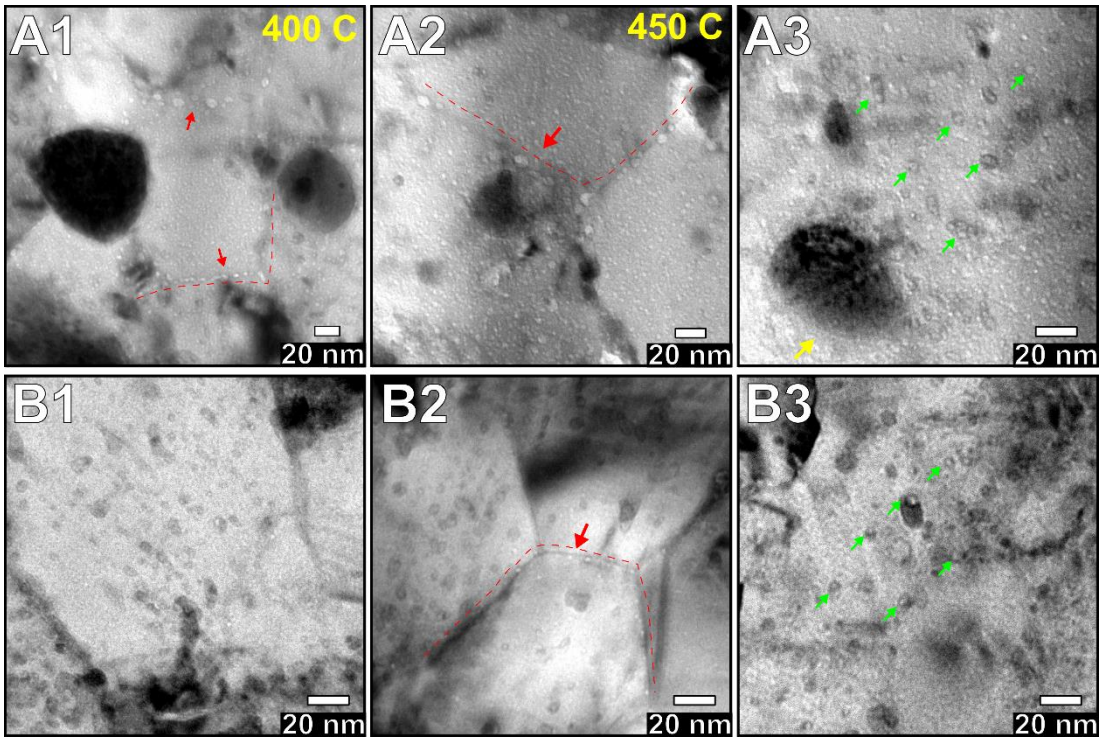

Figure 37: Post annealing He bubble distribution in He irradiated samples (A) Cu-10Ta and (B) Cu-3Ta post annealing temperatures of (1) 400 °C and (2-4) 450 °C.

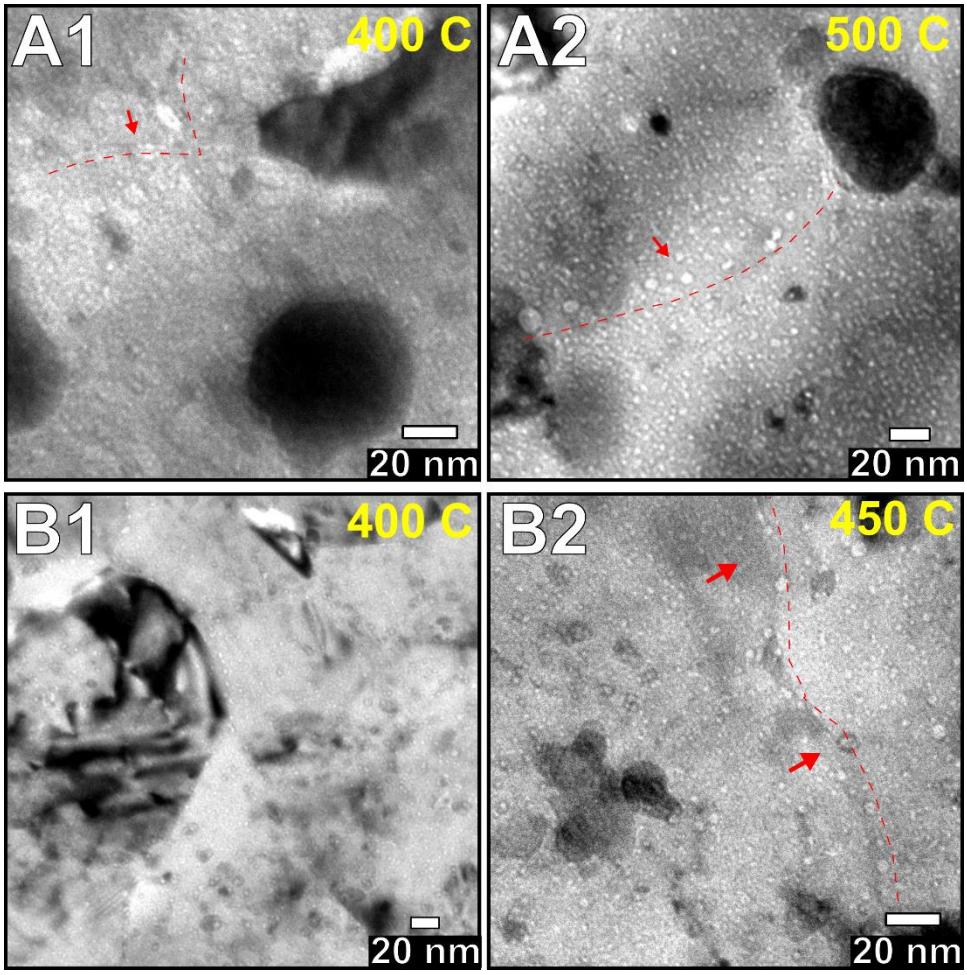

Figure 38: Post annealing He bubble distribution in He+Au irradiated samples (A) Cu-10Ta and (B) Cu-3Ta

Furthermore, no dissolution or short circuit diffusion of large Ta was observed in both the alloys till 450 °C indicating the stability of the large tantalum phases at <100 dpa. The nanoclusters were also observed to be stable in size and structure as the annealing temperature increased. It should be noted that numerous bubbles were associated with the nanoclusters at all temperatures and their size as well did not coarsen significantly with temperature, irradiation condition, and the alloy composition (**Figure 39**). They remained <3nm which is the typical size of these nanoclusters indicating the efficiency of these

nanoclusters in sequestering helium bubbles irrespective of different irradiation conditions and composition. Moreover, with an increase in temperature more tantalum nanoclusters were observed to be associated with helium bubbles to potentially utilize all high-density dispersed interfaces and reduce the amount of helium available for aggregating and swelling.

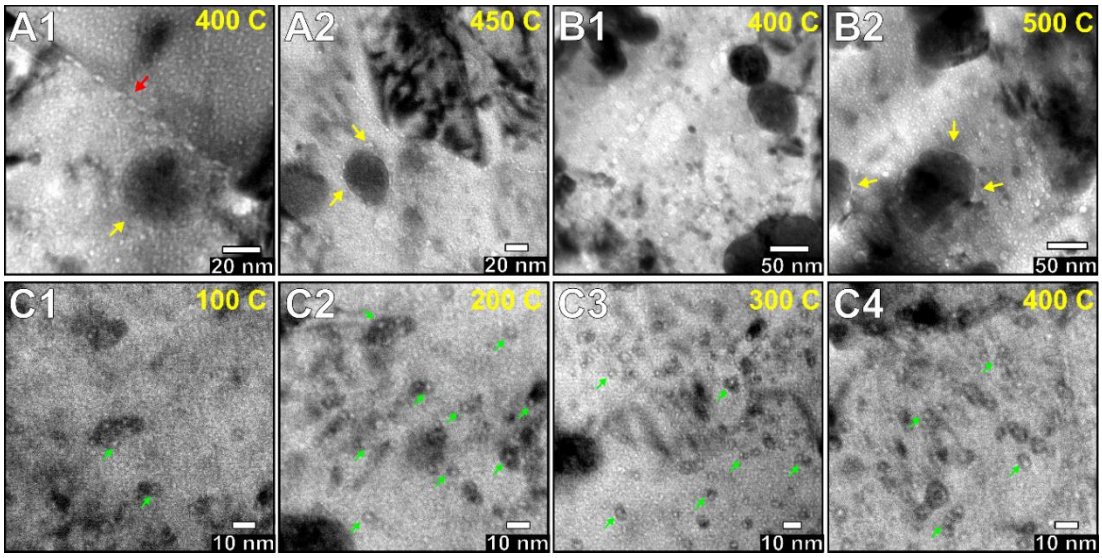

Figure 39: Ta phase post annealing. Large Ta precipitates in (A1-A2) He implanted Cu-10Ta (B1-B2) He+Au implanted Cu-10Ta (C1-C4) Bubble evolution with annealing temperature at Ta nanoclusters in Cu-3Ta irradiated with He+Au

Cavity size evolution with temperature was calculated and plotted for different cases (**Figure 40**) to aid quantitative analysis and comparison of both the alloys and irradiation conditions. Firstly, the bubble evolution with annealing in helium implanted Cu-10Ta (**Figure 40A)** shows that the bubble size in the matrix remains fairly constant at ~ 2nm till 400 °C after which it begins to increase with a bubble size of ~2.5 nm at 450 °C. On the other hand, the rate of growth is much higher for the bubbles at the grain boundaries which peaked at an average of ~5.5 nm at 450 °C. This bubble size evolution is consistent with the density evolution**.** The bubble density in the matrix decreased from ~1.9×10^{24} m^{-3} at

room temperature to ~9x10^{23} m^{-3} at 100 °C indicating coarsening migration of bubbles from the matrix to the sinks like grain boundaries and phase boundaries. The bubble density reduction is sluggish till 400 °C after which it reduced to 5 x10^{23} m^{-3} at 450 °C indicating eventual bubble coarsening at the matrix. Comparing this bubble size evolution in Cu-10Ta irradiated with helium to that of dual beam ion (**Figure 40** B) indicate a similar bubble size in the matrix which needs detailed comparison to understand the role of heavy-ion displacement cascade in bubble evolution.

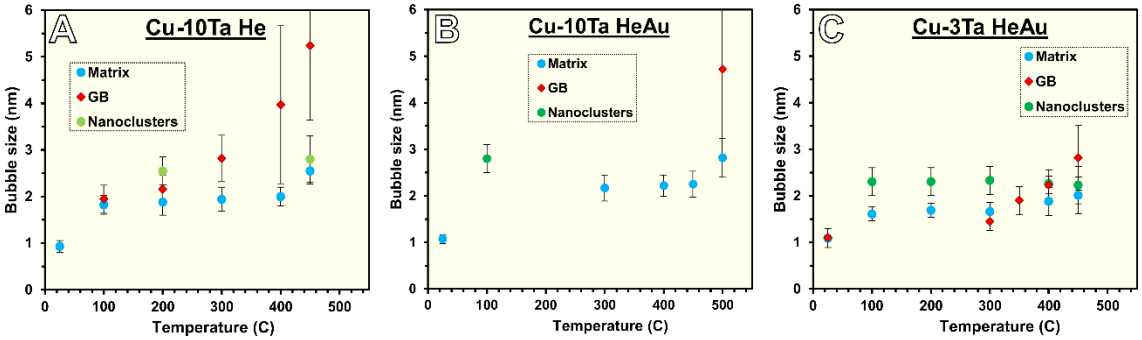

Figure 40: Cavity evolution at matrix and interfaces with annealing temperature

Next, the post-annealing bubble growth and evolution in Cu-3Ta irradiated with He+Au ions (**Figure 40** C) show bubbles of average size <2nm in the matrix till 450 C which is almost similar/slightly smaller than that of Cu-10Ta. Likewise, the cavity size at grain boundaries at 450 °C is ~2.7 nm which is much smaller than that in Cu-10Ta at 500 °C (~5nm). Moreover, the cavity growth rate at the grain boundaries is much smaller than that in Cu-10Ta irradiated with helium. Similarly, for a given condition the bubble density in Cu10Ta was almost 1.5 times higher than in Cu-3Ta. For instance, the matrix bubble density at room temperature was 2x10^{24} and 1.4x10^{24} /m^{3} in Cu10Ta and Cu3Ta respectively. At 450 °C, the bubble number density dropped in both to 5.2x10^{23} and

$4.1x10^{23}$ /m^3 respectively with the Cu-3Ta still possessing a smaller density of bubbles in the matrix. Overall, smaller bubbles at grain boundaries and lesser bubble density in Cu-3Ta highlights that Cu-3Ta can offer better resistance to bubble swelling compared to Cu-10Ta, while maintaining the microstructural stability with intense radiation. This is primarily attributed to the high fraction of essential coherent/incoherent precipitates that act as effective defect sinks in Cu-3Ta inspite of a slightly larger grain size.

7.4 Conclusions

In summary, room temperature implantations of helium and concurrent He+Au were carried out inside TEM in Cu-10Ta and Cu-3Ta followed by isochronal annealing up to 723 K to understand the microstructural stability and cavity evolution in both the alloys. The room temperature irradiation to high helium concentration and dpa levels did not lead to significant coarsening of grains in both Cu10Ta and Cu-3Ta. Overall grain sizes remained <150 nm indicating extraordinary microstructural stability in both the alloys. No dissolution and disordering of tantalum phases were observed indicating the phase stability at the present irradiation conditions <100 dpa. Few days post-irradiation, tiny bubbles of ~ 1nm was observed to be homogenously distributed in both the alloys and irradiation conditions. Further evolution of these bubbles with annealing till 450 °C indicated random migration coalescence to be a dominant coarsening mechanism involved. Comparison of bubble evolution and statistics in Cu-3Ta and Cu-10Ta at similar conditions showed smaller bubble size and density in Cu-3Ta indicating an overall enhanced resistance of Cu-3Ta to swelling to both helium and dual beam irradiation at high temperatures.

CHAPTER 8

8 SUMMARY AND FUTURE WORK

Nanocrystalline (NC) and dispersion strengthened alloys possess great potential for structural applications like nuclear reactors due to their combination of exceptional strength, creep properties, and high interface/sink concentration for neutralizing radiation induced defects. However, their inherent shortcomings such as microstructural and phase instability to such an intense reactor environment suppress their potential from being completely utilized. In this dissertation, the radiation resistance of stable bulk NC Cu-Ta system is systematically studied at several temperatures and dose levels attained using self-ion irradiation (high dose), helium ion irradiation, and in-situ helium and dual beam irradiations. The practical implications from this study will aid engineering NC materials with stable interfaces for structural and radiation applications. The main insights gathered from this dissertation are summarized below:

(1) Self-ion irradiation of Cu-10Ta (Chapter 4) to several doses till 600 peak dpa and at various temperatures showed promising resistance to radiation hardening and lattice swelling due to the presence of enormous stable interfaces in the material as grain boundaries and phase boundaries (Ta precipitates). At high doses, the microstructure further self-heals by re-precipitating Ta nanoclusters after the dissolution of Ta from both large and small Ta precipitates. This self-healing behavior and extraordinary stability of the nanoclusters are attributed to the immiscible nature of Ta in Cu (high positive enthalpy of mixing).

(2) Under helium irradiation (Chapter 5), the helium bubbles were observed to be preferentially segregating at the Ta nanoclusters (through TEM characterization and atom probe analysis) revealing their efficiency in acting as trapping sites for helium, sequestering helium bubbles, and suppressing swelling.

(3) Compositional optimization of Cu-Ta to reduce the concentration of large tantalum precipitates was performed (Cu-3at.%Ta) and radiation tolerance of the compositionally optimized Cu-3Ta to high dose self-ion irradiation was compared with Cu-10Ta. The results reveal promising phase stability and radiation tolerance in Cu-3Ta compared to Cu-10Ta (Chapter 6).

(4) Further comparison of both the compositions to helium and dual beam irradiations were carried out in-situ coupled with annealing till 450 °C to understand the microstructural response, defect evolution and underlying mechanisms involved in both the alloys (Chapter 7). The dual beam irradiation confirmed the microstructural stability in both the alloys till ~70 dpa and 70 at.% He. The cavity evolution at various temperatures in matrix and grain boundaries revealed an overall better resistance in Cu-3Ta to bubble growth and swelling at high helium and temperature levels.

Overall, this dissertation provides valuable insights on the radiation response of a microstructurally stabilized nanocrystalline alloy system to further the understanding of radiation damage mechanisms in a new class of materials and provide a pathway to superior design strategies for developing radiation tolerant structures with stable interfaces.

This dissertation, through systematic irradiation experiments, presented promising stability and radiation tolerance in NC Cu-Ta alloy compared to various candidate ferritic-martensitic steels, ODS alloys, and nanolayered materials. As a part of continuing the existing research efforts, additional experiments can be performed on these irradiated samples in the future to gain more insights on the unexplored aspects of radiation effects in stable NC alloys which include:

i. Characterizing the defect characteristics using Positron Annihilation spectroscopy.

Positrons are highly sensitive to vacancy-vacancy and vacancy-solute complexes making Positron Annihilation Spectroscopy (PAS) a powerful tool to obtain information about defect accumulation in irradiated materials at scales not detectable on TEM (Selim 2021). For instance, characteristic positron lifetime obtained from this technique can provide information on the type (e.g.,1-D, 2-D, 3-D defects) and size of defects ranging from monovacancy to nanovoids, to SFTs, dislocations, etc. (Meslin et al. 2010). In addition to positron lifetime measurements, Doppler broadening (DB) and coincident Doppler broadening techniques (CDB) of PAS can provide useful chemical information at the defect sites (Parente et al. 2015; Y. L. Liu et al. 2021). Thus, PAS can be utilized as an effective complementary tool to TEM and APT to obtain valuable insights on defect size, density, critical temperature to form defect clusters from monovacancies and understanding of its chemical interaction with solute (Ta) atoms.

ii. Analyzing the relation between grain boundary character and sink efficiency behavior using ACOM TEM.

Sink strength and efficiency of the interfaces such as grain boundaries have been observed to be dependent on the grain boundary orientation and character (W. Z. Han et al. 2012). Furthermore, the grain boundary characteristics can be affected as a result of defect interaction and accumulation at the grain boundaries. Studying the effect of grain boundary character and misorientation on the defect denuded zone formation (sink efficiency and stability) and on the cumulative radiation response of NC Cu-Ta is critical to a better understanding of the role of interface nature on the radiation performance of stable nanocrystalline alloys.

iii. In-situ tension testing using push-to-pull (PTP) device.

Irradiation in metals leads to excessive hardening which could result in embrittlement. Hence it is highly necessary to study the ductility of the material in response to irradiation. Since the ion induced radiation damage spans only a depth of few nanometers it is often challenging to use conventional techniques to measure tensile and yield properties. Advances in in-situ TEM mechanical testing enable measuring mechanical properties at nanoscale (Schuler et al. 2019) in addition to visualization of elastic and plastic deformation, dislocation interaction with grain boundaries and other real-time microstructural changes. Push to pull device fabricated by Bruker corporation (**Figure 41**) can be utilized to perform in-situ TEM tensile testing of nanocrystalline Cu-Ta to get more insights on ductility post-irradiation.

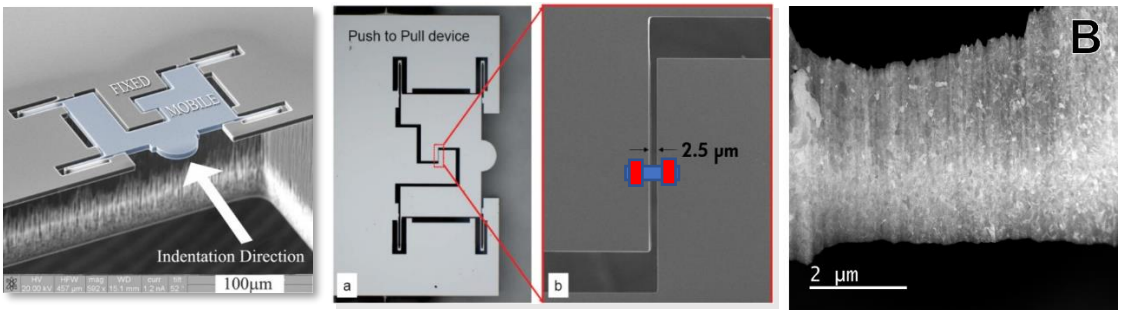

Figure 41: (A) Schematic of push-to-pull (PTP) device fabricated by Bruker *("Hysitron Push-to-Pull Device" n.d.)*. (B) A sample FIB lamella prepared for mounting on to the PTP device.

Furthermore, for attaining broader practical applications and to push the limits of temperature and strength requirements, it is vital to extend this design strategy to other candidate metals with higher strength and melting temperature (e.g., Fe, Ni, Ti etc.,) utilizing appropriate immiscible solute addition. For instance, based on a similar design strategy, several other nanocrystalline and ultra-fine-grained alloys such as a Fe based trimiscible alloy (Fe-Cu-Ag) and Ni based alloy containing rare-earth alloying addition of Y and Zr at various concentrations (Ni-Y-Zr) are being developed and studied. Preliminary characterization of Fe-Cu-Ag has shown the presence of nanocrystalline microstructure with anomalous mechanical response. Further in-detail characterization under various thermal, mechanical and radiation conditions is a part of future work.

REFERENCES

Alamo, A., J.L. Bertin, V.K. Shamardin, and P. Wident. 2007. “Mechanical Properties of 9Cr Martensitic Steels and ODS-FeCr Alloys after Neutron Irradiation at 325°C up to 42dpa.” *Journal of Nuclear Materials* 367–370 (August): 54–59. https://doi.org/10.1016/j.jnucmat.2007.03.166.

Alamo, A, M Horsten, X Averty, E.I Materna-Morris, M Rieth, and J.C Brachet. 2000. “Mechanical Behavior of Reduced-Activation and Conventional Martensitic Steels after Neutron Irradiation in the Range 250–450°C.” *Journal of Nuclear Materials* 283–287 (December): 353–57. https://doi.org/10.1016/S0022-3115(00)00076-3.

Allen, T.R., J. Gan, J.I. Cole, M.K. Miller, J.T. Busby, S. Shutthanandan, and S. Thevuthasan. 2008. “Radiation Response of a 9 Chromium Oxide Dispersion Strengthened Steel to Heavy Ion Irradiation.” *Journal of Nuclear Materials* 375 (1): 26–37. https://doi.org/10.1016/j.jnucmat.2007.11.001.

Arshad, Salman N., Timothy G. Lach, Mohsen Pouryazdan, Horst Hahn, Pascal Bellon, Shen J. Dillon, and Robert S. Averback. 2013. “Dependence of Shear-Induced Mixing on Length Scale.” *Scripta Materialia* 68 (3): 215–18. https://doi.org/10.1016/j.scriptamat.2012.10.027.

Ashkenazy, Yinon, Nhon Q. Vo, Daniel Schwen, Robert S. Averback, and Pascal Bellon. 2012. “Shear Induced Chemical Mixing in Heterogeneous Systems.” *Acta Materialia* 60 (3): 984–93. https://doi.org/10.1016/j.actamat.2011.11.014.

Atwater, Harry A., Carl V. Thompson, and Henry I. Smith. 1988. “Ion-bombardment-enhanced Grain Growth in Germanium, Silicon, and Gold Thin Films.” *Journal of Applied Physics* 64 (5): 2337–53. https://doi.org/10.1063/1.341665.

Aydogan, E., J.S. Weaver, S.A. Maloy, O. El-Atwani, Y.Q. Wang, and N.A. Mara. 2018. “Microstructure and Mechanical Properties of FeCrAl Alloys under Heavy Ion Irradiations.” *Journal of Nuclear Materials* 503 (May): 250–62. https://doi.org/10.1016/j.jnucmat.2018.03.002.

Bai, Xian-Ming, Arthur F. Voter, Richard G. Hoagland, Michael Nastasi, and Blas P. Uberuaga. 2010. “Efficient Annealing of Radiation Damage Near Grain Boundaries via Interstitial Emission.” *Science* 327 (5973): 1631–34. https://doi.org/10.1126/science.1183723.

Beyerlein, I.J., A. Caro, M.J. Demkowicz, N.A. Mara, A. Misra, and B.P. Uberuaga. 2013. “Radiation Damage Tolerant Nanomaterials.” *Materials Today* 16 (11): 443–49. https://doi.org/10.1016/j.mattod.2013.10.019.

Bhatia, M. A., M. Rajagopalan, K. A. Darling, M. A. Tschopp, and K. N. Solanki. 2017. "The Role of Ta on Twinnability in Nanocrystalline Cu–Ta Alloys." *Materials Research Letters* 5 (1): 48–54. https://doi.org/10.1080/21663831.2016.1201160.

Birtcher, R.C., M.A. Kirk, K. Furuya, G.R. Lumpkin, and M-O. Ruault. 2005. "In Situ Transmission Electron Microscopy Investigation of Radiation Effects." *Journal of Materials Research* 20 (7): 1654–83. https://doi.org/10.1557/JMR.2005.0242.

Campos, Marcos F de, Jailton C Damasceno, Rogério Machado, and Carlos A Achete. n.d. "UNCERTAINTY ESTIMATION OF LATTICE PARAMETERS MEASURED BY X-RAY DIFFRACTION," 7.

Certain, A., S. Kuchibhatla, V. Shutthanandan, D.T. Hoelzer, and T.R. Allen. 2013. "Radiation Stability of Nanoclusters in Nano-Structured Oxide Dispersion Strengthened (ODS) Steels." *Journal of Nuclear Materials* 434 (1–3): 311–21. https://doi.org/10.1016/j.jnucmat.2012.11.021.

Chang, Yong-Qin, Qiang Guo, Jing Zhang, Lin Chen, Yi Long, and Fa-Rong Wan. 2013. "Irradiation Effects on Nanocrystalline Materials." *Frontiers of Materials Science* 7 (2): 143–55. https://doi.org/10.1007/s11706-013-0199-3.

Chee, S.W., B. Stumphy, N.Q. Vo, R.S. Averback, and P. Bellon. 2010. "Dynamic Self-Organization in Cu Alloys under Ion Irradiation." *Acta Materialia* 58 (12): 4088–99. https://doi.org/10.1016/j.actamat.2010.03.039.

Chen, Tianyi, Eda Aydogan, Jonathan G. Gigax, Di Chen, Jing Wang, Xuemei Wang, S. Ukai, F.A. Garner, and Lin Shao. 2015. "Microstructural Changes and Void Swelling of a 12Cr ODS Ferritic-Martensitic Alloy after High-Dpa Self-Ion Irradiation." *Journal of Nuclear Materials* 467 (December): 42–49. https://doi.org/10.1016/j.jnucmat.2015.09.016.

Cheng, G.M., W.Z. Xu, Y.Q. Wang, A. Misra, and Y.T. Zhu. 2016. "Grain Size Effect on Radiation Tolerance of Nanocrystalline Mo." *Scripta Materialia* 123 (October): 90–94. https://doi.org/10.1016/j.scriptamat.2016.06.007.

Clark, G. J., A. D. Marwick, R. H. Koch, and R. B. Laibowitz. 1987. "Effects of Radiation Damage in Ion-implanted Thin Films of Metal-oxide Superconductors." *Applied Physics Letters* 51 (2): 139–41. https://doi.org/10.1063/1.98594.

Dai, Y., G.R. Odette, and T. Yamamoto. 2012. "The Effects of Helium in Irradiated Structural Alloys." In *Comprehensive Nuclear Materials*, 141–93. Elsevier. https://doi.org/10.1016/B978-0-08-056033-5.00006-9.

Darling, K. A., M. Rajagopalan, M. Komarasamy, M. A. Bhatia, B. C. Hornbuckle, R. S. Mishra, and K. N. Solanki. 2016. “Extreme Creep Resistance in a Microstructurally Stable Nanocrystalline Alloy.” *Nature* 537 (7620): 378–81. https://doi.org/10.1038/nature19313.

Darling, K.A., A.J. Roberts, Y. Mishin, S.N. Mathaudhu, and L.J. Kecskes. 2013. “Grain Size Stabilization of Nanocrystalline Copper at High Temperatures by Alloying with Tantalum.” *Journal of Alloys and Compounds* 573 (October): 142–50. https://doi.org/10.1016/j.jallcom.2013.03.177.

Demkowicz, M. J., R. G. Hoagland, and J. P. Hirth. 2008. “Interface Structure and Radiation Damage Resistance in Cu-Nb Multilayer Nanocomposites.” *Physical Review Letters* 100 (13): 136102. https://doi.org/10.1103/PhysRevLett.100.136102.

Demkowicz, M.J., A. Misra, and A. Caro. 2012. “The Role of Interface Structure in Controlling High Helium Concentrations.” *Current Opinion in Solid State and Materials Science* 16 (3): 101–8. https://doi.org/10.1016/j.cossms.2011.10.003.

Dolph, Corey K., Douglas J. da Silva, Matthew J. Swenson, and Janelle P. Wharry. 2016. “Plastic Zone Size for Nanoindentation of Irradiated Fe–9%Cr ODS.” *Journal of Nuclear Materials* 481 (December): 33–45. https://doi.org/10.1016/j.jnucmat.2016.08.033.

Duan, Binghuang, Cornelia Heintze, Frank Bergner, Andreas Ulbricht, Shavkat Akhmadaliev, Elvira Oñorbe, Yann de Carlan, and Tieshan Wang. 2017. “The Effect of the Initial Microstructure in Terms of Sink Strength on the Ion-Irradiation-Induced Hardening of ODS Alloys Studied by Nanoindentation.” *Journal of Nuclear Materials* 495 (November): 118–27. https://doi.org/10.1016/j.jnucmat.2017.08.014.

El-Atwani, O., K. Hattar, J. A. Hinks, G. Greaves, S. S. Harilal, and A. Hassanein. 2015. “Helium Bubble Formation in Ultrafine and Nanocrystalline Tungsten under Different Extreme Conditions.” *Journal of Nuclear Materials* 458 (March): 216–23. https://doi.org/10.1016/j.jnucmat.2014.12.095.

El-Atwani, O., J.E. Nathaniel, A.C. Leff, B.R. Muntifering, J.K. Baldwin, K. Hattar, and M.L. Taheri. 2017. “The Role of Grain Size in He Bubble Formation: Implications for Swelling Resistance.” *Journal of Nuclear Materials* 484 (February): 236–44. https://doi.org/10.1016/j.jnucmat.2016.12.003.

Enrique, Raúl A., and Pascal Bellon. 2000. “Compositional Patterning in Systems Driven by Competing Dynamics Of Different Length Scale.” *Physical Review Letters* 84 (13): 2885–88. https://doi.org/10.1103/PhysRevLett.84.2885.

———. 2001. “Compositional Patterning in Immiscible Alloys Driven by Irradiation.” *Physical Review B* 63 (13): 134111. https://doi.org/10.1103/PhysRevB.63.134111.

Farrell, K. 1980. “Experimental Effects of Helium on Cavity Formation during Irradiation—a Review.” *Radiation Effects* 53 (3–4): 175–94. https://doi.org/10.1080/00337578008207114.

Fave, Loïc, Manuel A. Pouchon, Max Döbeli, Martina Schulte-Borchers, and Akihiro Kimura. 2014. “Helium Ion Irradiation Induced Swelling and Hardening in Commercial and Experimental ODS Steels.” *Journal of Nuclear Materials* 445 (1–3): 235–40. https://doi.org/10.1016/j.jnucmat.2013.11.004.

Fischer-Cripps, Anthony C. 2004. *Nanoindentation*. 2nd ed. Mechanical Engineering Series. New York: Springer-Verlag. https://www.springer.com/gp/book/9780387220451.

———. 2011. “Nanoindentation Testing.” In *Nanoindentation*, edited by Anthony C. Fischer-Cripps, 21–37. Mechanical Engineering Series. New York, NY: Springer New York. https://doi.org/10.1007/978-1-4419-9872-9_2.

Fleetwood, Daniel M, Peter S Winokur, and Paul E Dodd. 2000. “An Overview of Radiation E□ects on Electronics in the Space Telecommunications Environment.” *Microelectronics Reliability*, 10.

Frolov, T., K.A. Darling, L.J. Kecskes, and Y. Mishin. 2012. “Stabilization and Strengthening of Nanocrystalline Copper by Alloying with Tantalum.” *Acta Materialia* 60 (5): 2158–68. https://doi.org/10.1016/j.actamat.2012.01.011.

Frolov, T., and Y. Mishin. 2010. “Stable Nanocolloidal Structures in Metallic Systems.” *Physical Review Letters* 104 (5): 055701. https://doi.org/10.1103/PhysRevLett.104.055701.

Fu, E. G., A. Misra, H. Wang, Lin Shao, and X. Zhang. 2010. “Interface Enabled Defects Reduction in Helium Ion Irradiated Cu/V Nanolayers.” *Journal of Nuclear Materials* 407 (3): 178–88. https://doi.org/10.1016/j.jnucmat.2010.10.011.

Fu, E.G., H. Wang, J. Carter, Lin Shao, Y.Q. Wang, and X. Zhang. 2013. “Fluence-Dependent Radiation Damage in Helium (He) Ion-Irradiated Cu/V Multilayers.” *Philosophical Magazine* 93 (8): 883–98. https://doi.org/10.1080/14786435.2012.735773.

Getto, E., Z. Jiao, A.M. Monterrosa, K. Sun, and G.S. Was. 2015. “Effect of Irradiation Mode on the Microstructure of Self-Ion Irradiated Ferritic-Martensitic Alloys.”

Journal of Nuclear Materials 465 (October): 116–26. https://doi.org/10.1016/j.jnucmat.2015.05.016.

Gigax, Jonathan G., Eda Aydogan, Tianyi Chen, Di Chen, Lin Shao, Y. Wu, W.Y. Lo, Y. Yang, and F.A. Garner. 2015. "The Influence of Ion Beam Rastering on the Swelling of Self-Ion Irradiated Pure Iron at 450 °C." *Journal of Nuclear Materials* 465 (October): 343–48. https://doi.org/10.1016/j.jnucmat.2015.05.025.

Goodhew, P. J. 1983. "On the Migration of Helium Bubbles." *Radiation Effects* 78 (1–4): 381–83. https://doi.org/10.1080/00337578308207386.

Gruber, E. E. 1967. "Calculated Size Distributions for Gas Bubble Migration and Coalescence in Solids." *Journal of Applied Physics* 38 (1): 243–50. https://doi.org/10.1063/1.1708962.

Han, Weizhong, Michael J. Demkowicz, Nathan A. Mara, Engang Fu, Subhasis Sinha, Anthony D. Rollett, Yongqiang Wang, John S. Carpenter, Irene J. Beyerlein, and Amit Misra. 2013. "Design of Radiation Tolerant Materials Via Interface Engineering." *Advanced Materials* 25 (48): 6975–79. https://doi.org/10.1002/adma.201303400.

Han, W.Z., M.J. Demkowicz, E.G. Fu, Y.Q. Wang, and A. Misra. 2012. "Effect of Grain Boundary Character on Sink Efficiency." *Acta Materialia* 60 (18): 6341–51. https://doi.org/10.1016/j.actamat.2012.08.009.

Hattar, K., D. C. Bufford, and D. L. Buller. 2014. "Concurrent in Situ Ion Irradiation Transmission Electron Microscope." *Nuclear Instruments and Methods in Physics Research Section B: Beam Interactions with Materials and Atoms* 338 (November): 56–65. https://doi.org/10.1016/j.nimb.2014.08.002.

Hoelzer, D.T., C.P. Massey, S.J. Zinkle, D.C. Crawford, and K.A. Terrani. 2020. "Modern Nanostructured Ferritic Alloys: A Compelling and Viable Choice for Sodium Fast Reactor Fuel Cladding Applications." *Journal of Nuclear Materials* 529 (February): 151928. https://doi.org/10.1016/j.jnucmat.2019.151928.

Hornbuckle, B. C., T. Rojhirunsakool, M. Rajagopalan, T. Alam, G. P. Purja Pun, R. Banerjee, K. N. Solanki, Y. Mishin, L. J. Kecskes, and K. A. Darling. 2015. "Effect of Ta Solute Concentration on the Microstructural Evolution in Immiscible Cu-Ta Alloys." *JOM* 67 (12): 2802–9. https://doi.org/10.1007/s11837-015-1643-x.

Hornbuckle, B. C., K. N. Solanki, and K. A. Darling. 2021. "Perceived Stability versus Resistance at Prolonged High Temperature Exposure: Optimizing Nanocrystalline Alloys against Grain Growth." *Materials Science and Engineering: A.*

Hosemann, Peter, Daniel Kiener, Yongqiang Wang, and Stuart A. Maloy. 2012. “Issues to Consider Using Nano Indentation on Shallow Ion Beam Irradiated Materials.” *Journal of Nuclear Materials* 425 (1–3): 136–39. https://doi.org/10.1016/j.jnucmat.2011.11.070.

Hou, Qing, Yulu Zhou, Jun Wang, and Aihong Deng. 2010. “Cascade Coalescence of Noble Gas Bubbles in Materials.” *Journal of Applied Physics* 107 (8): 084901. https://doi.org/10.1063/1.3354088.

“Hysitron Push-to-Pull Device.” n.d. Bruker.Com. Accessed October 6, 2019. https://www.bruker.com/products/surface-and-dimensional-analysis/nanomechanical-test-instruments/nanomechanical-upgrade-options/push-to-pull-device.html.

Ipatova, I., G. Greaves, S. Pacheco-Gutiérrez, S. C. Middleburgh, M. J. D. Rushton, and E. Jimenez-Melero. 2021. “In-Situ TEM Investigation of Nano-Scale Helium Bubble Evolution in Tantalum-Doped Tungsten at 800°C.” *Journal of Nuclear Materials* 550 (July): 152910. https://doi.org/10.1016/j.jnucmat.2021.152910.

Jiao, Z., and G.S. Was. 2010. “The Role of Irradiated Microstructure in the Localized Deformation of Austenitic Stainless Steels.” *Journal of Nuclear Materials* 407 (1): 34–43. https://doi.org/10.1016/j.jnucmat.2010.07.006.

Jin, Miaomiao, Penghui Cao, and Michael P. Short. 2019. “Mechanisms of Grain Boundary Migration and Growth in Nanocrystalline Metals under Irradiation.” *Scripta Materialia* 163 (April): 66–70. https://doi.org/10.1016/j.scriptamat.2018.12.038.

Kale, C., S. Turnage, P. Garg, I. Adlakha, S. Srinivasan, B. C. Hornbuckle, K. Darling, and K. N. Solanki. 2019. “Thermo-Mechanical Strengthening Mechanisms in a Stable Nanocrystalline Binary Alloy – A Combined Experimental and Modeling Study.” *Materials & Design* 163 (February): 107551. https://doi.org/10.1016/j.matdes.2018.107551.

Kaoumi, D., A. T. Motta, and R. C. Birtcher. 2008. “A Thermal Spike Model of Grain Growth under Irradiation.” *Journal of Applied Physics* 104 (7): 073525. https://doi.org/10.1063/1.2988142.

Kirk, Marquis A., Peter M. Baldo, Amelia C.Y. Liu, Edward A. Ryan, Robert C. Birtcher, Zhongwen Yao, Sen Xu, et al. 2009. “In Situ Transmission Electron Microscopy and Ion Irradiation of Ferritic Materials.” *Microscopy Research and Technique* 72 (3): 182–86. https://doi.org/10.1002/jemt.20670.

Klassen, T., U. Herr, and R.S. Averback. 1997. “BALL MILLING OF SYSTEMS WITH POSITIVE HEAT OF MIXING: EFFECT OF TEMPERATURE IN Ag-Cu.” *Acta Materialia* 45 (7): 2921–30. https://doi.org/10.1016/S1359-6454(96)00388-6.

Knaster, J., A. Moeslang, and T. Muroga. 2016. “Materials Research for Fusion.” *Nature Physics* 12 (5): 424–34. https://doi.org/10.1038/nphys3735.

Koch, C. C., R. O. Scattergood, K. A. Darling, and J. E. Semones. 2008. “Stabilization of Nanocrystalline Grain Sizes by Solute Additions.” *Journal of Materials Science* 43 (23–24): 7264–72. https://doi.org/10.1007/s10853-008-2870-0.

Koch, Carl C., Ronald O. Scattergood, Mostafa Saber, and Hasan Kotan. 2013. “High Temperature Stabilization of Nanocrystalline Grain Size: Thermodynamic versus Kinetic Strategies.” *Journal of Materials Research* 28 (13): 1785–91. https://doi.org/10.1557/jmr.2012.429.

Koch, C.C. 1993. “The Synthesis and Structure of Nanocrystalline Materials Produced by Mechanical Attrition: A Review.” *Nanostructured Materials* 2 (2): 109–29. https://doi.org/10.1016/0965-9773(93)90016-5.

———. 1997. “Synthesis of Nanostructured Materials by Mechanical Milling: Problems and Opportunities.” *Nanostructured Materials* 9 (1–8): 13–22. https://doi.org/10.1016/S0965-9773(97)00014-7.

Koju, R. K., K. A. Darling, L. J. Kecskes, and Y. Mishin. 2016. “Zener Pinning of Grain Boundaries and Structural Stability of Immiscible Alloys.” *JOM* 68 (6): 1596–1604. https://doi.org/10.1007/s11837-016-1899-9.

Koju, R. K., K. A. Darling, K. N. Solanki, and Y. Mishin. 2018. “Atomistic Modeling of Capillary-Driven Grain Boundary Motion in Cu-Ta Alloys.” *Acta Materialia* 148 (April): 311–19. https://doi.org/10.1016/j.actamat.2018.01.027.

Kolli, R. Prakash, and David N. Seidman. 2007. “Comparison of Compositional and Morphological Atom-Probe Tomography Analyses for a Multicomponent Fe-Cu Steel.” *Microscopy and Microanalysis* 13 (4): 272–84. https://doi.org/10.1017/S1431927607070675.

Krumwiede, D.L., T. Yamamoto, T.A. Saleh, S.A. Maloy, G.R. Odette, and P. Hosemann. 2018. “Direct Comparison of Nanoindentation and Tensile Test Results on Reactor-Irradiated Materials.” *Journal of Nuclear Materials* 504 (June): 135–43. https://doi.org/10.1016/j.jnucmat.2018.03.021.

Lescoat, M.-L., I. Monnet, J. Ribis, P. Dubuisson, Y. de Carlan, J.-M. Costantini, and J. Malaplate. 2011. “Amorphization of Oxides in ODS Materials under Low and High

Energy Ion Irradiations." *Journal of Nuclear Materials* 417 (1–3): 266–69. https://doi.org/10.1016/j.jnucmat.2011.01.065.

Li, Nan, E. G. Fu, H. Wang, J. J. Carter, L. Shao, S. A. Maloy, A. Misra, and X. Zhang. 2009. "He Ion Irradiation Damage in Fe/W Nanolayer Films." *Journal of Nuclear Materials*, Particle Beam Induced Radiation Effects in Materials, 389 (2): 233–38. https://doi.org/10.1016/j.jnucmat.2009.02.007.

Li, Nan, M. S. Martin, O. Anderoglu, A. Misra, L. Shao, H. Wang, and X. Zhang. 2009. "He Ion Irradiation Damage in Al/Nb Multilayers." *Journal of Applied Physics* 105 (12): 123522. https://doi.org/10.1063/1.3138804.

Li, Qian, C. M. Parish, K. A. Powers, and M. K. Miller. 2014. "Helium Solubility and Bubble Formation in a Nanostructured Ferritic Alloy." *Journal of Nuclear Materials* 445 (1): 165–74. https://doi.org/10.1016/j.jnucmat.2013.10.048.

Li, Shi-Hao, Jing-Ting Li, and Wei-Zhong Han. 2019. "Radiation-Induced Helium Bubbles in Metals." *Materials* 12 (7): 1036. https://doi.org/10.3390/ma12071036.

Liu, C., C. Yu, N. Hashimoto, S. Ohnuki, M. Ando, K. Shiba, and S. Jitsukawa. 2011. "Micro-Structure and Micro-Hardness of ODS Steels after Ion Irradiation." *Journal of Nuclear Materials* 417 (1–3): 270–73. https://doi.org/10.1016/j.jnucmat.2011.01.067.

Liu, Joyce C., Jian Li, and J. W. Mayer. 1990. "Temperature Effect on Ion-irradiation-induced Grain Growth in Cu Thin Films." *Journal of Applied Physics* 67 (5): 2354–58. https://doi.org/10.1063/1.345530.

Liu, Y.L., L.G. Song, Y. Chen, R.Y. Bai, Z. Wang, T. Zhu, P. Zhang, et al. 2021. "Study on the Interaction between He and Defects Induced by He-Ion Irradiation in W and W5Re Alloy." *Fusion Engineering and Design* 162 (January): 112118. https://doi.org/10.1016/j.fusengdes.2020.112118.

Lu, Chenyang, Zheng Lu, Xu Wang, Rui Xie, Zhengyuan Li, Michael Higgins, Chunming Liu, Fei Gao, and Lumin Wang. 2017. "Enhanced Radiation-Tolerant Oxide Dispersion Strengthened Steel and Its Microstructure Evolution under Helium-Implantation and Heavy-Ion Irradiation." *Scientific Reports* 7 (1): 40343. https://doi.org/10.1038/srep40343.

Lu, Fengyuan, Mengbing Huang, Faisal Yaqoob, Maik Lang, Fereydoon Namavar, Christina Trautmann, Hongtao Sun, Rodney C. Ewing, and Jie Lian. 2012. "Displacive Radiation-Induced Structural Contraction in Nanocrystalline ZrN." *Applied Physics Letters* 101 (4): 041904. https://doi.org/10.1063/1.4738772.

Lucas, A. A. 1984. “Helium in Metals.” *Physica B+C*, Proceedings of the 4th General Conference of the Condensed Matter Division of the EPS, 127 (1): 225–39. https://doi.org/10.1016/S0378-4363(84)80035-2.

Lupinacci, A., K. Chen, Y. Li, M. Kunz, Z. Jiao, G.S. Was, M.D. Abad, A.M. Minor, and P. Hosemann. 2015. “Characterization of Ion Beam Irradiated 304 Stainless Steel Utilizing Nanoindentation and Laue Microdiffraction.” *Journal of Nuclear Materials* 458 (March): 70–76. https://doi.org/10.1016/j.jnucmat.2014.11.050.

Ma, E. 2005. “Alloys Created between Immiscible Elements.” *Progress in Materials Science* 50 (4): 413–509. https://doi.org/10.1016/j.pmatsci.2004.07.001.

Marwick, A D. 1978. “Segregation in Irradiated Alloys: The Inverse Kirkendall Effect and the Effect of Constitution on Void Swelling.” *Journal of Physics F: Metal Physics* 8 (9): 1849–61. https://doi.org/10.1088/0305-4608/8/9/008.

Meslin, E., M. Lambrecht, M. Hernández-Mayoral, F. Bergner, L. Malerba, P. Pareige, B. Radiguet, et al. 2010. “Characterization of Neutron-Irradiated Ferritic Model Alloys and a RPV Steel from Combined APT, SANS, TEM and PAS Analyses.” *Journal of Nuclear Materials* 406 (1): 73–83. https://doi.org/10.1016/j.jnucmat.2009.12.021.

Miller, M.K., and E.A. Kenik. 2004. “Atom Probe Tomography: A Technique for Nanoscale Characterization.” *Microscopy and Microanalysis* 10 (3): 336–41. https://doi.org/10.1017/S1431927604040577.

Misra, A., M. J. Demkowicz, X. Zhang, and R. G. Hoagland. 2007. “The Radiation Damage Tolerance of Ultra-High Strength Nanolayered Composites.” *JOM* 59 (9): 62–65. https://doi.org/10.1007/s11837-007-0120-6.

Mohamed, Walid, Brandon Miller, Douglas Porter, and Korukonda Murty. 2016. “The Role of Grain Size on Neutron Irradiation Response of Nanocrystalline Copper.” *Materials* 9 (3): 144. https://doi.org/10.3390/ma9030144.

Motta, Arthur T., and Clément Lemaignan. 1992a. “A Ballistic Mixing Model for the Amorphization of Precipitates in Zircaloy under Neutron Irradiation.” *Journal of Nuclear Materials* 195 (3): 277–85. https://doi.org/10.1016/0022-3115(92)90519-Q.

———. 1992b. “A Ballistic Mixing Model for the Amorphization of Precipitates in Zircaloy under Neutron Irradiation.” *Journal of Nuclear Materials* 195 (3): 277–85. https://doi.org/10.1016/0022-3115(92)90519-Q.

Muntifering, Brittany, Sarah Jane Blair, Cajer Gong, Aaron Dunn, Remi Dingreville, Jianmin Qu, and Khalid Hattar. 2016. "Cavity Evolution at Grain Boundaries as a Function of Radiation Damage and Thermal Conditions in Nanocrystalline Nickel." *Materials Research Letters* 4 (2): 96–103. https://doi.org/10.1080/21663831.2015.1121165.

Murty, K.L., and I. Charit. 2008. "Structural Materials for Gen-IV Nuclear Reactors: Challenges and Opportunities." *Journal of Nuclear Materials* 383 (1–2): 189–95. https://doi.org/10.1016/j.jnucmat.2008.08.044.

"Nano Indentation." n.d. Accessed August 23, 2019. http://home.iitk.ac.in/~kbalani/vl-kb/nano.html.

Nelson, R.S., J.A. Hudson, and D.J. Mazey. 1972. "The Stability of Precipitates in an Irradiation Environment." *Journal of Nuclear Materials* 44 (3): 318–30. https://doi.org/10.1016/0022-3115(72)90043-8.

Nordlund, Kai, Steven J. Zinkle, Andrea E. Sand, Fredric Granberg, Robert S. Averback, Roger E. Stoller, Tomoaki Suzudo, et al. 2018. "Primary Radiation Damage: A Review of Current Understanding and Models." *Journal of Nuclear Materials* 512 (December): 450–79. https://doi.org/10.1016/j.jnucmat.2018.10.027.

Odette, G. R., and D. T. Hoelzer. 2010. "Irradiation-Tolerant Nanostructured Ferritic Alloys: Transforming Helium from a Liability to an Asset." *JOM* 62 (9): 84–92. https://doi.org/10.1007/s11837-010-0144-1.

Oliver, W. C., and G. M. Pharr. 1992. "An Improved Technique for Determining Hardness and Elastic Modulus Using Load and Displacement Sensing Indentation Experiments." *Journal of Materials Research* 7 (6): 1564–83. https://doi.org/10.1557/JMR.1992.1564.

Ono, K., K. Arakawa, and K. Hojou. 2002. "Formation and Migration of Helium Bubbles in Fe and Fe–9Cr Ferritic Alloy." *Journal of Nuclear Materials* 307–311 (December): 1507–12. https://doi.org/10.1016/S0022-3115(02)01268-0.

Ono, K., S. Furuno, K. Hojou, T. Kino, K. Izui, O. Takaoka, N. Kubo, K. Mizuno, and K. Ito. 1992. "In-Situ Observation of the Migration and Growth of Helium Bubbles in Aluminum." *Journal of Nuclear Materials* 191–194 (September): 1269–73. https://doi.org/10.1016/0022-3115(92)90678-E.

Ono, K., M. Miyamoto, K. Arakawa, and R.C. Birtcher. 2009. "Dynamical Response of Helium Bubble Motion to Irradiation with High-Energy Self-Ions in Aluminum at High Temperature." *Philosophical Magazine* 89 (6): 513–24. https://doi.org/10.1080/14786430802629493.

Parente, P., T. Leguey, V. de Castro, T. Gigl, M. Reiner, C. Hugenschmidt, and R. Pareja. 2015. “Characterization of Ion-Irradiated ODS Fe–Cr Alloys by Doppler Broadening Spectroscopy Using a Positron Beam.” *Journal of Nuclear Materials* 464 (September): 140–46. https://doi.org/10.1016/j.jnucmat.2015.04.033.

Pochet, P., Pascal Bellon, L. Chaffron, and G. Martin. 1996. “Phase Transformations under Ball Milling: Theory versus Experiment.” *Materials Science Forum* 225–227 (July): 207–16. https://doi.org/10.4028/www.scientific.net/MSF.225-227.207.

Rajagopalan, M., K. Darling, S. Turnage, R.K. Koju, B. Hornbuckle, Y. Mishin, and K.N. Solanki. 2017. “Microstructural Evolution in a Nanocrystalline Cu-Ta Alloy: A Combined in-Situ TEM and Atomistic Study.” *Materials & Design* 113 (January): 178–85. https://doi.org/10.1016/j.matdes.2016.10.020.

Rajagopalan, M., K.A. Darling, C. Kale, S.A. Turnage, R.K. Koju, B.C. Hornbuckle, Y. Mishin, and K.N. Solanki. 2019. “Nanotechnology Enabled Design of a Structural Material with Extreme Strength as Well as Thermal and Electrical Properties.” *Materials Today* 31 (December): 10–20. https://doi.org/10.1016/j.mattod.2019.09.024.

Ribis, J., M.-L. Lescoat, Y. de Carlan, J.-M. Costantini, I. Monnet, T. Cozzika, F. Delabrouille, and J. Malaplate. 2011. “Stability of Nano-Oxides upon Heavy Ion Irradiation of an ODS Material.” *Journal of Nuclear Materials* 417 (1–3): 262–65. https://doi.org/10.1016/j.jnucmat.2010.12.068.

Rojhirunsakool, Tanaporn, Kristopher A. Darling, Mark A. Tschopp, Ganga P. Purja Pun, Yuri Mishin, Rajarshi Banerjee, and Laszlo J. Kecskes. 2015. “Structure and Thermal Decomposition of a Nanocrystalline Mechanically Alloyed Supersaturated Cu–Ta Solid Solution.” *MRS Communications* 5 (2): 333–39. https://doi.org/10.1557/mrc.2015.34.

Russell, K C. n.d. “PHASE STABILITY UNDER IRRADIATION.” *PROGRESS IN MATERIALS SCIENCE*, 206.

Russell, K.C. 1993. “Phase Instability under Cascade Damage Irradiation.” *Journal of Nuclear Materials* 206 (2–3): 129–38. https://doi.org/10.1016/0022-3115(93)90120-N.

Sagaradze, V. V, V. I Shalaev, V. L Arbuzov, B. N Goshchitskii, Yun Tian, Wan Qun, and Sun Jiguang. 2001. “Radiation Resistance and Thermal Creep of ODS Ferritic Steels.” *Journal of Nuclear Materials* 295 (2): 265–72. https://doi.org/10.1016/S0022-3115(01)00511-6.

Sauvage, X, L Renaud, B Deconihout, D Blavette, D. H Ping, and K Hono. 2001. “Solid State Amorphization in Cold Drawn Cu/Nb Wires.” *Acta Materialia* 49 (3): 389–94. https://doi.org/10.1016/S1359-6454(00)00338-4.

Schroeder, Herbert, and Paulo F. P. Fichtner. 1991. “On the Coarsening Mechanisms of Helium Bubbles — Ostwald Ripening versus Migration and Coalescence.” *Journal of Nuclear Materials* 179–181 (March): 1007–10. https://doi.org/10.1016/0022-3115(91)90261-5.

Schuler, Jennifer D., Christopher M. Barr, Nathan M. Heckman, Guild Copeland, Brad L. Boyce, Khalid Hattar, and Timothy J. Rupert. 2019. “In Situ High-Cycle Fatigue Reveals Importance of Grain Boundary Structure in Nanocrystalline Cu-Zr.” *JOM* 71 (4): 1221–32. https://doi.org/10.1007/s11837-019-03361-7.

Segal, V. M. 1995. “Materials Processing by Simple Shear.” *Materials Science and Engineering: A* 197 (2): 157–64. https://doi.org/10.1016/0921-5093(95)09705-8.

Selim, F.A. 2021. “Positron Annihilation Spectroscopy of Defects in Nuclear and Irradiated Materials- a Review.” *Materials Characterization* 174 (April): 110952. https://doi.org/10.1016/j.matchar.2021.110952.

Shu, Shipeng, P. Bellon, and R. S. Averback. 2015. “Role of Point-Defect Sinks on Irradiation-Induced Compositional Patterning in Model Binary Alloys.” *Physical Review B* 91 (21): 214107. https://doi.org/10.1103/PhysRevB.91.214107.

Singh, B.N., and H. Trinkaus. 1992. “An Analysis of the Bubble Formation Behaviour under Different Experimental Conditions.” *Journal of Nuclear Materials* 186 (2): 153–65. https://doi.org/10.1016/0022-3115(92)90330-N.

Smidt, F. A., and J. A. Sprague. 1973. “Suppression of Void Nucleation by a Vacancy Trapping Mechanism.” *Scripta Metallurgica* 7 (5): 495–501. https://doi.org/10.1016/0036-9748(73)90102-6.

Srinivasan, S., C. Kale, B.C. Hornbuckle, K.A. Darling, M.R. Chancey, E. Hernández-Rivera, Y. Chen, et al. 2020. “Radiation Tolerance and Microstructural Changes of Nanocrystalline Cu-Ta Alloy to High Dose Self-Ion Irradiation.” *Acta Materialia* 195 (August): 621–30. https://doi.org/10.1016/j.actamat.2020.05.061.

Srour, J. R., and J. M. McGarrity. 1988. “Radiation Effects on Microelectronics in Space.” *Proceedings of the IEEE* 76 (11): 1443–69. https://doi.org/10.1109/5.90114.

“Standard Practice for Neutron Radiation Damage Simulation by Charged-Particle Irradiation.” 96.

Stassinopoulos, E. G., and J. P. Raymond. 1988. “The Space Radiation Environment for Electronics.” *Proceedings of the IEEE* 76 (11): 1423–42. https://doi.org/10.1109/5.90113.

Stiegler, J O, and L K Mansur. 1979. “Radiation Effects in Structural Materials.” *Annual Review of Materials Science* 9 (1): 405–54. https://doi.org/10.1146/annurev.ms.09.080179.002201.

Stoller, R.E. 2012. “Primary Radiation Damage Formation.” In *Comprehensive Nuclear Materials*, 293–332. Elsevier. https://doi.org/10.1016/B978-0-08-056033-5.00027-6.

Stoller, R.E., M.B. Toloczko, G.S. Was, A.G. Certain, S. Dwaraknath, and F.A. Garner. 2013. “On the Use of SRIM for Computing Radiation Damage Exposure.” *Nuclear Instruments and Methods in Physics Research Section B: Beam Interactions with Materials and Atoms* 310 (September): 75–80. https://doi.org/10.1016/j.nimb.2013.05.008.

Sun, C., M. Song, K. Y. Yu, Y. Chen, M. Kirk, M. Li, H. Wang, and X. Zhang. 2013. “In Situ Evidence of Defect Cluster Absorption by Grain Boundaries in Kr Ion Irradiated Nanocrystalline Ni.” *Metallurgical and Materials Transactions A* 44 (4): 1966–74. https://doi.org/10.1007/s11661-013-1635-9.

Swenson, M.J., and J.P. Wharry. 2017. “Nanocluster Irradiation Evolution in Fe-9%Cr ODS and Ferritic-Martensitic Alloys.” *Journal of Nuclear Materials* 496 (December): 24–40. https://doi.org/10.1016/j.jnucmat.2017.08.045.

Taylor, Caitlin A., Joshua D. Sugar, David B. Robinson, Norman C. Bartelt, Ryan B. Sills, and Khalid Hattar. 2020. “Using In Situ TEM Helium Implantation and Annealing to Study Cavity Nucleation and Growth.” *JOM* 72 (5): 2032–41. https://doi.org/10.1007/s11837-020-04117-4.

Taylor, Caitlin, Daniel Bufford, Brittany Muntifering, David Senor, Mackenzie Steckbeck, Justin Davis, Barney Doyle, Daniel Buller, and Khalid Hattar. 2017. “In Situ TEM Multi-Beam Ion Irradiation as a Technique for Elucidating Synergistic Radiation Effects.” *Materials* 10 (10): 1148. https://doi.org/10.3390/ma10101148.

Toloczko, M.B., F.A. Garner, V.N. Voyevodin, V.V. Bryk, O.V. Borodin, V.V. Mel’nychenko, and A.S. Kalchenko. 2014. “Ion-Induced Swelling of ODS Ferritic Alloy MA957 Tubing to 500 Dpa.” *Journal of Nuclear Materials* 453 (1–3): 323–33. https://doi.org/10.1016/j.jnucmat.2014.06.011.

Toloczko, M.B, D.S Gelles, F.A Garner, R.J Kurtz, and K Abe. 2004. “Irradiation Creep and Swelling from 400 to 600 °C of the Oxide Dispersion Strengthened Ferritic

Alloy MA957." *Journal of Nuclear Materials* 329–333 (August): 352–55. https://doi.org/10.1016/j.jnucmat.2004.04.296.

Trinkaus, H, and B.N Singh. 2003. "Helium Accumulation in Metals during Irradiation – Where Do We Stand?" *Journal of Nuclear Materials* 323 (2–3): 229–42. https://doi.org/10.1016/j.jnucmat.2003.09.001.

Tschopp, M. A., H. A. Murdoch, L. J. Kecskes, and K. A. Darling. 2014. "'Bulk' Nanocrystalline Metals: Review of the Current State of the Art and Future Opportunities for Copper and Copper Alloys." *JOM* 66 (6): 1000–1019. https://doi.org/10.1007/s11837-014-0978-z.

Tschopp, M. A., K. N. Solanki, F. Gao, X. Sun, M. A. Khaleel, and M. F. Horstemeyer. 2012. "Probing Grain Boundary Sink Strength at the Nanoscale: Energetics and Length Scales of Vacancy and Interstitial Absorption by Grain Boundaries in α-Fe." *Physical Review B* 85 (6): 064108. https://doi.org/10.1103/PhysRevB.85.064108.

Turnage, S. A., M. Rajagopalan, K. A. Darling, P. Garg, C. Kale, B. G. Bazehhour, I. Adlakha, et al. 2018. "Anomalous Mechanical Behavior of Nanocrystalline Binary Alloys under Extreme Conditions." *Nature Communications* 9 (1). https://doi.org/10.1038/s41467-018-05027-5.

Tyler, S. K., and P. J. Goodhew. 1980. "Direct Evidence for the Brownian Motion of Helium Bubbles." *Journal of Nuclear Materials* 92 (2): 201–6. https://doi.org/10.1016/0022-3115(80)90103-8.

UENISHI, K, K. F. KOBAYASHI, S. NASU, H. HATANO, K. N. ISHIHARA, and P. H. SHINGU. 1992. "Mechanical Alloying in the Fe-Cu System." *Mechanical Alloying in the Fe-Cu System* 83 (2): 132–35.

Villacampa, I., J. C. Chen, P. Spätig, H. P. Seifert, and F. Duval. 2018. "Helium Bubble Evolution and Hardening in 316L by Post-Implantation Annealing." *Journal of Nuclear Materials* 500 (March): 389–402. https://doi.org/10.1016/j.jnucmat.2018.01.017.

Wang, L., X.P. Wang, L.F. Zhang, Y.X. Gao, R. Liu, R. Gao, Y. Jiang, et al. 2019. "Helium Desorption Behavior and Growth Mechanism of Helium Bubbles in FeCrNi Film." *Nuclear Materials and Energy* 21 (December): 100710. https://doi.org/10.1016/j.nme.2019.100710.

Wang, M., N. Q. Vo, M. Campion, T. D. Nguyen, D. Setman, S. Dillon, P. Bellon, and R. S. Averback. 2014. "Forced Atomic Mixing during Severe Plastic Deformation:

Chemical Interactions and Kinetically Driven Segregation." *Acta Materialia* 66 (Supplement C): 1–11. https://doi.org/10.1016/j.actamat.2013.11.066.

Was, Gary S. 2017. *Fundamentals of Radiation Materials Science*. New York, NY: Springer New York. https://doi.org/10.1007/978-1-4939-3438-6.

Was, G.S., D. Petti, S. Ukai, and S. Zinkle. 2019. "Materials for Future Nuclear Energy Systems." *Journal of Nuclear Materials* 527 (December): 151837. https://doi.org/10.1016/j.jnucmat.2019.151837.

Wei, L. C., and R. S. Averback. 1997. "Phase Evolution during Ion-Beam Mixing of Ag–Cu." *Journal of Applied Physics* 81 (2): 613–23. https://doi.org/10.1063/1.364202.

Wharry, Janelle P., Matthew J. Swenson, and Kayla H. Yano. 2017. "A Review of the Irradiation Evolution of Dispersed Oxide Nanoparticles in the b.c.c. Fe-Cr System: Current Understanding and Future Directions." *Journal of Nuclear Materials* 486 (April): 11–20. https://doi.org/10.1016/j.jnucmat.2017.01.009.

Wichert, Th., M. Deicher, G. Grübel, E. Recknagel, and W. Reiner. 1985. "Migration of Helium Atoms in Copper at 25 K." *Physical Review Letters* 55 (7): 726–29. https://doi.org/10.1103/PhysRevLett.55.726.

Wilkes, P. 1979. "Phase Stability under Irradiation — a Review of Theory and Experiment." *Journal of Nuclear Materials* 83 (1): 166–75. https://doi.org/10.1016/0022-3115(79)90602-0.

Willertz, L. E., and P. G. Shewmon. 1970. "Diffusion of Helium Gas Bubbles in Gold and Copper Foils." *Metallurgical Transactions* 1 (8): 2217–23. https://doi.org/10.1007/BF02643438.

Wurster, Stefan, and Reinhard Pippan. 2009. "Nanostructured Metals under Irradiation." *Scripta Materialia* 60 (12): 1083–87. https://doi.org/10.1016/j.scriptamat.2009.01.011.

Yu, K.Y., Y. Liu, E.G. Fu, Y.Q. Wang, M.T. Myers, H. Wang, L. Shao, and X. Zhang. 2013. "Comparisons of Radiation Damage in He Ion and Proton Irradiated Immiscible Ag/Ni Nanolayers." *Journal of Nuclear Materials* 440 (1–3): 310–18. https://doi.org/10.1016/j.jnucmat.2013.04.069.

Zhang, T., C. Vieh, K. Wang, and Y. Dai. 2014. "Irradiation-Induced Evolution of Mechanical Properties and Microstructure of Eurofer 97." *Journal of Nuclear Materials* 450 (1–3): 48–53. https://doi.org/10.1016/j.jnucmat.2013.12.007.

Zhang, X., E. G. Fu, A. Misra, and M. J. Demkowicz. 2010. “Interface-Enabled Defect Reduction in He Ion Irradiated Metallic Multilayers.” *JOM* 62 (12): 75–78. https://doi.org/10.1007/s11837-010-0185-5.

Zhang, Xinghang, Khalid Hattar, Youxing Chen, Lin Shao, Jin Li, Cheng Sun, Kaiyuan Yu, et al. 2018. “Radiation Damage in Nanostructured Materials.” *Progress in Materials Science* 96 (July): 217–321. https://doi.org/10.1016/j.pmatsci.2018.03.002.

Ziegler, James F., and Jochen P. Biersack. 1985. “The Stopping and Range of Ions in Matter.” In *Treatise on Heavy-Ion Science: Volume 6: Astrophysics, Chemistry, and Condensed Matter*, edited by D. Allan Bromley, 93–129. Boston, MA: Springer US. https://doi.org/10.1007/978-1-4615-8103-1_3.

Ziegler, James F., M.D. Ziegler, and J.P. Biersack. 2010. “SRIM – The Stopping and Range of Ions in Matter (2010).” *Nuclear Instruments and Methods in Physics Research Section B: Beam Interactions with Materials and Atoms* 268 (11–12): 1818–23. https://doi.org/10.1016/j.nimb.2010.02.091.

Zinkle, S.J., and G.S. Was. 2013. “Materials Challenges in Nuclear Energy.” *Acta Materialia* 61 (3): 735–58. https://doi.org/10.1016/j.actamat.2012.11.004.

Zinkle, Steven J., and Jeremy T. Busby. 2009. “Structural Materials for Fission & Fusion Energy.” *Materials Today* 12 (11): 12–19. https://doi.org/10.1016/S1369-7021(09)70294-9.